JETP Letters, Vol. 77, No. 6, 2003, pp. 251–255. Translated from Pis'ma v Zhurnal Éksperimental'noĭ i Teoreticheskoĭ Fiziki, Vol. 77, No. 6, 2003, pp. 299–304.

Competition between Ferromagnetic and Antiferromagnetic Spin Ordering in Nuclear Matter

A. A. Isayev

National Science Center Kharkov Institute of Physics and Technology, ul. Akademicheskaya 1, Kharkov, 61108 Ukraine
e-mail: isayev@mail-x-change.com

Received January 30, 2003

The possibility of ferromagnetic and antiferromagnetic phase transitions in symmetric nuclear matter is analyzed in Fermi liquid theory with the Skyrme effective interaction. The density dependence of the ferromagnetic and antiferromagnetic parameters of spin polarization at zero temperature is obtained for SkM* and SGII effective potentials. In the density region where both solutions of self-consistency equations exist, the ferromagnetic spin state is preferable over the antiferromagnetic spin state. © *2003 MAIK "Nauka/Interperiodica".*

PACS numbers: 21.65.+f; 76.25.+z; 71.10.Ay

The appearance of states with spin polarization in nuclear matter is of great interest in view of astrophysical applications. Depending on whether the nuclear matter is spin polarized or not, different scenarios of a supernova explosion and cooling of neutron stars can be realized. The possibility of a phase transition of normal nuclear matter to the ferromagnetic state has been studied by many authors. In the gas model of hard spheres, neutron matter was shown to become ferromagnetic at $\rho \approx 0.41$ fm^{-3} [1]. It was found in [2, 3] that a long-range attractive interaction significantly increases the ferromagnetic transition density (e.g., to $\rho \approx 2.3$ fm^{-3} in Brueckner theory with a simple central potential and hard core only for singlet spin states [3]). By determining magnetic susceptibility with Skyrme effective forces, it was shown in [4] that the ferromagnetic transition occurs at $\rho \approx 0.18$–0.26 fm^{-3}. The Fermi liquid criterion for ferromagnetic instability in neutron matter with the Skyrme interaction is achieved at $\rho \approx 2$–$4\rho_0$ [5], where ρ_0 is the saturation density of nuclear matter. Akhiezer *et al.* [6] formulated the general conditions on the parameters of neutron–neutron interaction, which lead to the appearance of a magnetically ordered state in neutron matter. Spin correlations in dense neutron matter were studied in the Dirac–Hartree–Fock relativistic approach with the effective nucleon–meson Lagrangian in [7], where the ferromagnetic transition was predicted for a density equal to several saturation densities of nuclear matter. As was shown in [8], the Fock exchange term in relativistic mean-field theory is important for the rise of ferromagnetism in nuclear matter. The stability of strongly asymmetric nuclear matter against spin fluctuations was analyzed in [9], where it was shown that even a small admixture of protons encourages the ferromagnetic instability of the system. This conclusion was corroborated in [10] in the Dirac–Hartree–Fock relativistic approach for strongly asymmetric nuclear matter.

In models with relativistic nucleon–nucleon (*NN*) interaction, the ferromagnetic phase transition is likely suppressed up to the densities much higher than ρ_0 [11–13]. In particular, ferromagnetic instability was not found in recent investigations of neutron matter [14] and asymmetric nuclear matter [15] in the Brueckner–Hartree–Fock approach with Nijmegen II, Reid 93, and Nijmegen NSC97e realistic *NN* potentials. The same conclusion was obtained in [16], where the magnetic susceptibility of nuclear matter was calculated by using the Argonne two-body potential v_{18} and Urbana IX three-body potential.

In this paper, the study of the spin polarizability of nuclear matter is continued using the Fermi liquid description of nuclear matter [17, 18] with the effective Skyrme *NN* interaction used previously for calculations in nuclear matter [19–22]. Since the calculations of magnetic susceptibility with the effective Skyrme forces show that the ferromagnetic phase transition occurs in nuclear matter of a certain critical density, it is reasonable to determine the density dependence of the ferromagnetic spin polarization parameter of nuclear matter. In addition, the possibility of the antiferromagnetic phase transition in nuclear matter will be analyzed for the case where spins of protons and neutrons are oppositely directed. The antiferromagnetic spin-polarization parameter will be found as a function of density as well. The problem of the thermodynamic stability of the ferromagnetic and antiferromagnetic spin states will then be analyzed, and the phase preferable in the density region, where both types of solutions of self-consistency equations exist, will be determined.

We consider the thermodynamic properties of spin polarized states in nuclear matter up to high astrophysical densities. Nevertheless, we use a pure nucleon

0021-3640/03/7706-0251$24.00

description of nuclear matter, although other degrees of freedom such as pion, hyperon, kaon, or quark can be important for such high densities.

Basic equations. The normal states of nuclear matter is described by the normal nucleon distribution function $f_{\kappa_1\kappa_2} = \mathrm{Tr}\rho a^+_{\kappa_2} a_{\kappa_1}$. Here, $\kappa \equiv (\mathbf{p}, \sigma, \tau)$, where $\mathbf{p}$ is the momentum and $\sigma(\tau)$ is the projection of spin (isospin) onto the quantization axis, and ρ is the density matrix of the system. The energy of the system is a functional of the distribution function f, $E = E(f)$, and determines the single-particle energy

$$\varepsilon_{\kappa_1\kappa_2}(f) = \partial E(f)/\partial f_{\kappa_2\kappa_1}. \quad (1)$$

The matrix self-consistent equation for the distribution function f follows from the condition of a minimum of the thermodynamic potential [17]:

$$f = \{\exp(Y_0\varepsilon + Y_4) + 1\}^{-1} \equiv \{\exp(Y_0\xi) + 1\}^{-1}. \quad (2)$$

Here, ε and Y_4 are matrices in variables κ, $Y_{4\kappa_1\kappa_2} = Y_{4\tau_1}\delta_{\kappa_1\kappa_2}$ ($\tau_1 = p, n$); $Y_0 = 1/T$, $Y_{4p} = -\mu^0_p/T$, and $Y_{4n} = -\mu^0_n/T$ are the Lagrange multipliers; μ^0_p and μ^0_n are the chemical potentials of protons and neutrons, respectively; and T is temperature. We will analyze the possibility of forming various types of spin ordering (ferromagnetic and antiferromagnetic) in nuclear matter.

The normal distribution function can be decomposed in the Pauli matrices σ_i and τ_k in spin and isospin spaces as

$$\begin{aligned} f(\mathbf{p}) &= f_{00}(\mathbf{p})\sigma_0\tau_0 + f_{30}(\mathbf{p})\sigma_3\tau_0 \\ &+ f_{03}(\mathbf{p})\sigma_0\tau_3 + f_{33}(\mathbf{p})\sigma_3\tau_3. \end{aligned} \quad (3)$$

For the energy functional invariant about the rotations in spin and isospin spaces, the structure of the single-particle energy is similar to the structure of the distribution function f:

$$\begin{aligned} \varepsilon(\mathbf{p}) &= \varepsilon_{00}(\mathbf{p})\sigma_0\tau_0 + \varepsilon_{30}(\mathbf{p})\sigma_3\tau_0 \\ &+ \varepsilon_{03}(\mathbf{p})\sigma_0\tau_3 + \varepsilon_{33}(\mathbf{p})\sigma_3\tau_3. \end{aligned} \quad (4)$$

Using Eqs. (2) and (4), we can express the distribution functions f_{00}, f_{30}, f_{03}, and f_{33} in terms of ε in the explicit form

$$\begin{aligned} f_{00} &= \frac{1}{4}\{n(\omega_{+,+}) + n(\omega_{+,-}) + n(\omega_{-,+}) + n(\omega_{-,-})\}, \\ f_{30} &= \frac{1}{4}\{n(\omega_{+,+}) + n(\omega_{+,-}) - n(\omega_{-,+}) - n(\omega_{-,-})\}, \\ f_{03} &= \frac{1}{4}\{n(\omega_{+,+}) - n(\omega_{+,-}) + n(\omega_{-,+}) - n(\omega_{-,-})\}, \\ f_{33} &= \frac{1}{4}\{n(\omega_{+,+}) - n(\omega_{+,-}) - n(\omega_{-,+}) + n(\omega_{-,-})\}. \end{aligned} \quad (5)$$

Here, $n(\omega) = \{\exp(Y_0\omega) + 1\}^{-1}$ and

$$\begin{aligned} \omega_{+,+} &= \xi_{00} + \xi_{30} + \xi_{03} + \xi_{33}, \\ \omega_{+,-} &= \xi_{00} + \xi_{30} - \xi_{03} - \xi_{33}, \\ \omega_{-,+} &= \xi_{00} - \xi_{30} + \xi_{03} - \xi_{33}, \\ \omega_{-,-} &= \xi_{00} - \xi_{30} - \xi_{03} + \xi_{33}, \end{aligned}$$

where

$$\begin{aligned} \xi_{00} &= \varepsilon_{00} - \mu^0_{00}, \quad \xi_{30} = \varepsilon_{30}, \\ \xi_{03} &= \varepsilon_{03} - \mu^0_{03}, \quad \xi_{33} = \varepsilon_{33}, \\ \mu^0_{00} &= \frac{\mu^0_p + \mu^0_n}{2}, \quad \mu^0_{03} = \frac{\mu^0_p - \mu^0_n}{2}. \end{aligned}$$

As follows from the structure of distribution functions f, the exponent $\omega_{\pm,\pm}$ of the Fermi distribution function n plays the role of quasiparticle spectrum. In the case under consideration, the spectrum is fourfold split due to the spin and isospin dependences of the single-particle energy in Eq. (4). The distribution functions f must satisfy the normalization conditions

$$\frac{4}{\mathcal{V}}\sum_{\mathbf{p}} f_{00}(\mathbf{p}) = \rho, \quad (6)$$

$$\frac{4}{\mathcal{V}}\sum_{\mathbf{p}} f_{03}(\mathbf{p}) = \rho_p - \rho_n \equiv -\alpha\rho, \quad (7)$$

$$\frac{4}{\mathcal{V}}\sum_{\mathbf{p}} f_{30}(\mathbf{p}) = \rho_\uparrow - \rho_\downarrow \equiv \Delta\rho_{\uparrow\uparrow}, \quad (8)$$

$$\frac{4}{\mathcal{V}}\sum_{\mathbf{p}} f_{33}(\mathbf{p}) = (\rho_{p\uparrow} + \rho_{n\downarrow}) - (\rho_{p\downarrow} + \rho_{n\uparrow}) \equiv \Delta\rho_{\uparrow\downarrow}. \quad (9)$$

Here, α is the isospin asymmetry parameter; $\rho_{p\uparrow}$, $\rho_{p\downarrow}$ and $\rho_{n\uparrow}$, $\rho_{n\downarrow}$ are the densities of spin-up and spin-down protons and neutrons, respectively; and $\rho_\uparrow = \rho_{p\uparrow} + \rho_{n\uparrow}$ and $\rho_\downarrow = \rho_{p\downarrow} + \rho_{n\downarrow}$ are the densities of spin-up and spin-down nucleons, respectively. The densities $\Delta\rho_{\uparrow\uparrow}$ and $\Delta\rho_{\uparrow\downarrow}$ can be treated as ferromagnetic (FM) and antiferromagnetic (AFM) spin order parameters, respectively. Indeed, when all nucleon spins are identically directed (completely polarized FM spin state), $\Delta\rho_{\uparrow\uparrow} = \rho$ and $\Delta\rho_{\uparrow\downarrow} = 0$; when all proton spins are oriented in one direction and all neutron spins are oriented in the opposite direction (completely polarized AFM spin state), $\Delta\rho_{\uparrow\downarrow} = \rho$ and $\Delta\rho_{\uparrow\uparrow} = 0$.

To obtain the self-consistency equations, we specify the energy functional of the system in the form

$$\begin{aligned} E(f) &= E_0(f) + E_{\text{int}}(f), \\ E_0(f) &= 4\sum_{\mathbf{p}} \varepsilon_0(\mathbf{p}) f_{00}(\mathbf{p}), \quad \varepsilon_0(\mathbf{p}) = \frac{\mathbf{p}^2}{2m_0}, \\ E_{\text{int}}(f) &= 2\sum_{\mathbf{p}} \{\tilde{\varepsilon}_{00}(\mathbf{p}) f_{00}(\mathbf{p}) + \tilde{\varepsilon}_{30}(\mathbf{p}) f_{30}(\mathbf{p}) \\ &\quad + \tilde{\varepsilon}_{03}(\mathbf{p}) f_{03}(\mathbf{p}) + \tilde{\varepsilon}_{33}(\mathbf{p}) f_{33}(\mathbf{p})\}. \end{aligned} \tag{10}$$

Here, m_0 is the free-nucleon mass; and

$$\begin{aligned} \tilde{\varepsilon}_{00}(\mathbf{p}) &= \frac{1}{2\mathcal{V}}\sum_{\mathbf{q}} U_0(\mathbf{k}) f_{00}(\mathbf{q}), \quad \mathbf{k} = \frac{\mathbf{p}-\mathbf{q}}{2}, \\ \tilde{\varepsilon}_{30}(\mathbf{p}) &= \frac{1}{2\mathcal{V}}\sum_{\mathbf{q}} U_1(\mathbf{k}) f_{30}(\mathbf{q}), \\ \tilde{\varepsilon}_{03}(\mathbf{p}) &= \frac{1}{2\mathcal{V}}\sum_{\mathbf{q}} U_2(\mathbf{k}) f_{03}(\mathbf{q}), \\ \tilde{\varepsilon}_{33}(\mathbf{p}) &= \frac{1}{2\mathcal{V}}\sum_{\mathbf{q}} U_3(\mathbf{k}) f_{33}(\mathbf{q}) \end{aligned}$$

are Fermi liquid corrections to the free single-particle spectrum, where $U_0(\mathbf{k})$, …, $U_3(\mathbf{k})$ are the normal Fermi liquid amplitudes. Taking Eqs. (1) and (10) into account, we arrive at the self-consistency equations in the form

$$\begin{aligned} \xi_{00}(\mathbf{p}) &= \varepsilon_0(\mathbf{p}) + \tilde{\varepsilon}_{00}(\mathbf{p}) - \mu_{00}^0, \quad \xi_{30}(\mathbf{p}) = \tilde{\varepsilon}_{30}(\mathbf{p}), \\ \xi_{03}(\mathbf{p}) &= \tilde{\varepsilon}_{03}(\mathbf{p}) - \mu_{03}^0, \quad \xi_{33}(\mathbf{p}) = \tilde{\varepsilon}_{33}(\mathbf{p}). \end{aligned} \tag{11}$$

To obtain numerical results, we use the effective Skyrme interaction. In this case, the normal Fermi liquid amplitudes have the form [18]

$$\begin{aligned} U_0(\mathbf{k}) &= 6t_0 + t_3\rho^\beta + \frac{2}{\hbar^2}[3t_1 + t_2(5+4x_2)]\mathbf{k}^2, \\ U_1(\mathbf{k}) &= -2t_0(1-2x_0) - \frac{1}{3}t_3\rho^\beta(1-2x_3) \\ &\quad - \frac{2}{\hbar^2}[t_1(1-2x_1) - t_2(1+2x_2)]\mathbf{k}^2 \equiv a + b\mathbf{k}^2, \\ U_2(\mathbf{k}) &= -2t_0(1+2x_0) - \frac{1}{3}t_3\rho^\beta(1+2x_3) \\ &\quad - \frac{2}{\hbar^2}[t_1(1+2x_1) - t_2(1+2x_2)]\mathbf{k}^2, \\ U_3(\mathbf{k}) &= -2t_0 - \frac{1}{3}t_3\rho^\beta - \frac{2}{\hbar^2}(t_1 - t_2)\mathbf{k}^2 \equiv c + d\mathbf{k}^2, \end{aligned} \tag{12}$$

where t_i, x_i, and β are the phenomenological constants characterizing a given parameterization of the Skyrme forces. For the numerical calculations, we use the SkM* [23] and SGII [24] potentials designed for describing the properties of systems with small isospin asymmetry. Taking into account the explicit form of the Fermi liquid amplitudes and Eqs. (6)–(9), we obtain

$$\xi_{00} = \frac{p^2}{2m_{00}} - \mu_{00}, \tag{13}$$

$$\xi_{03} = \frac{p^2}{2m_{03}} - \mu_{03}, \tag{14}$$

$$\xi_{30} = \left(a + b\frac{\mathbf{p}^2}{4}\right)\frac{\Delta\rho_{\uparrow\uparrow}}{8} + \frac{b}{32}\langle\mathbf{q}^2\rangle_{30}, \tag{15}$$

$$\xi_{33} = \left(c + d\frac{\mathbf{p}^2}{4}\right)\frac{\Delta\rho_{\uparrow\downarrow}}{8} + \frac{d}{32}\langle\mathbf{q}^2\rangle_{33}. \tag{16}$$

Here, the effective nucleon mass m_{00} and effective isovector mass m_{03} are determined by the formulas

$$\begin{aligned} \frac{\hbar^2}{2m_{00}} &= \frac{\hbar^2}{2m_0} + \frac{\rho}{16}[3t_1 + t_2(5+4x_2)], \\ \frac{\hbar^2}{2m_{03}} &= \frac{\alpha\rho}{16}[t_1(1+2x_1) - t_2(1+2x_2)], \end{aligned} \tag{17}$$

the renormalized chemical potentials μ_{00} and μ_{03} should be found from Eqs. (6) and (7), and

$$\langle\mathbf{q}^2\rangle_{30} = \frac{4}{V}\sum_{\mathbf{q}} \mathbf{q}^2 f_{30}(\mathbf{q}), \tag{18}$$

$$\langle\mathbf{q}^2\rangle_{33} = \frac{4}{V}\sum_{\mathbf{q}} \mathbf{q}^2 f_{33}(\mathbf{q}) \tag{19}$$

are the second-order moments of the corresponding distribution functions.

Thus, taking into account expressions (5) for the distribution functions f, we obtain self-consistent equations (6)–(9), (18), and (19) for the effective chemical potentials μ_{00} and μ_{03}, FM and AFM spin order parameters $\Delta\rho_{\uparrow\uparrow}$ and $\Delta\rho_{\uparrow\downarrow}$, and second-order moments $\langle\mathbf{q}^2\rangle_{30}$ and $\langle\mathbf{q}^2\rangle_{33}$.

Ferromagnetic and antiferromagnetic spin-order parameters at zero temperature. Early investigations on the spin polarizability with the effective Skyrme forces were based on the calculation of magnetic susceptibility and determination of its pole structure [4, 5] that is responsible for the onset of instability with respect to spin fluctuations. In this paper, the FM spin polarization will be directly found as a function of the nuclear-matter density for zero temperature. Moreover, the possibility of AFM ordering in nuclear matter

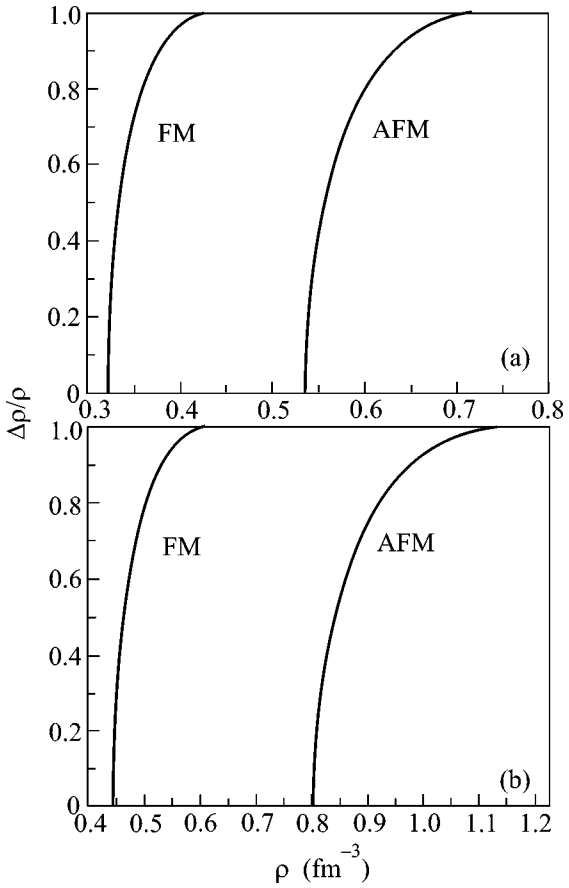

Fig. 1. Density dependence of the FM and AFM spin polarization parameters at zero temperature for (a) SkM* and (b) SGII potentials.

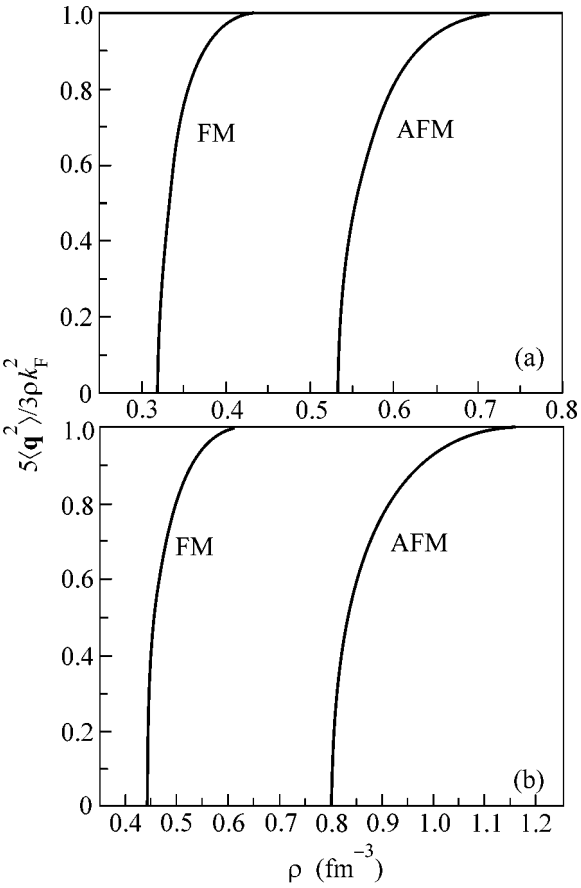

Fig. 2. Same as in Fig. 1, but for the second-order moments of the distribution functions.

and thermodynamic stability of two types of ordering will be analyzed.

We consider the behavior of the zero-temperature spin polarization in symmetric nuclear matter ($\rho_p = \rho_n$). Ferromagnetic spin ordering corresponds to $\Delta\rho_{\uparrow\uparrow} \neq 0$, $\langle \mathbf{q}^2\rangle_{30} \neq 0$, $\Delta\rho_{\uparrow\downarrow} = 0$, and $\langle \mathbf{q}^2\rangle_{33} = 0$. Antiferromagnetic spin ordering corresponds to $\Delta\rho_{\uparrow\downarrow} \neq 0$, $\langle \mathbf{q}^2\rangle_{33} \neq 0$, $\Delta\rho_{\uparrow\uparrow} = 0$, and $\langle \mathbf{q}^2\rangle_{30} = 0$. In the completely polarized FM state, nontrivial solutions of the self-consistency equations have the form

$$\Delta\rho_{\uparrow\uparrow} = \rho, \quad \langle \mathbf{q}^2\rangle_{30} = \frac{3}{5}\rho k_F^2. \tag{20}$$

Here, $k_F = (3\pi^2\rho)^{1/3}$ is the Fermi wavenumber of symmetric nuclear matter for the case, where the degrees of freedom corresponding to the spin-down nucleons are inaccessible. For completely AFM polarized nuclear matter,

$$\Delta\rho_{\uparrow\downarrow} = \rho, \quad \langle \mathbf{q}^2\rangle_{33} = \frac{3}{5}\rho k_F^2. \tag{21}$$

Here, k_F is the same as in Eq. (20), because the degrees of freedom corresponding to spin-down protons and spin-up neutrons are inaccessible. Figure 1 shows the FM $\Delta\rho_{\uparrow\uparrow}/\rho$ and AFM $\Delta\rho_{\uparrow\downarrow}/\rho$ spin polarization parameters calculated numerically with the effective SkM* and SGII potentials.

The FM spin-order parameter appears at the density $\rho \approx 2\rho_0$ and $\rho \approx 2.75\rho_0$ for SkM* and SGII potentials, respectively. The AFM spin-order parameter appears at the density $\rho \approx 3.3\rho_0$ and $\rho \approx 5\rho_0$ for SkM* and SGII potentials, respectively. For both potentials, FM ordering appears earlier than the AFM ordering. Nuclear matter becomes completely FM polarized ($\Delta\rho_{\uparrow\uparrow}/\rho = 1$) at the density $\rho \approx 2.7\rho_0$ and $\rho \approx 3.9\rho_0$ for the SkM* and SGII potentials, respectively. The completely AFM polarized state ($\Delta\rho_{\uparrow\downarrow}/\rho = 1$) arises at the density $\rho \approx 4.5\rho_0$ and $\rho \approx 7.2\rho_0$ for the SkM* and SGII potentials, respectively.

The second-order moments $\langle \mathbf{q}^2\rangle_{30}$ and $\langle \mathbf{q}^2\rangle_{33}$ of the distribution functions f_{30} and f_{33} also play the role of order parameters. Figure 2 shows the density dependence of these quantities normalized to their values in the completely polarized state. The ratios $5\langle \mathbf{q}^2\rangle_{30}/3\rho k_F^2$ and $5\langle \mathbf{q}^2\rangle_{30}/3\rho k_F^2$ are treated as the FM and AFM order

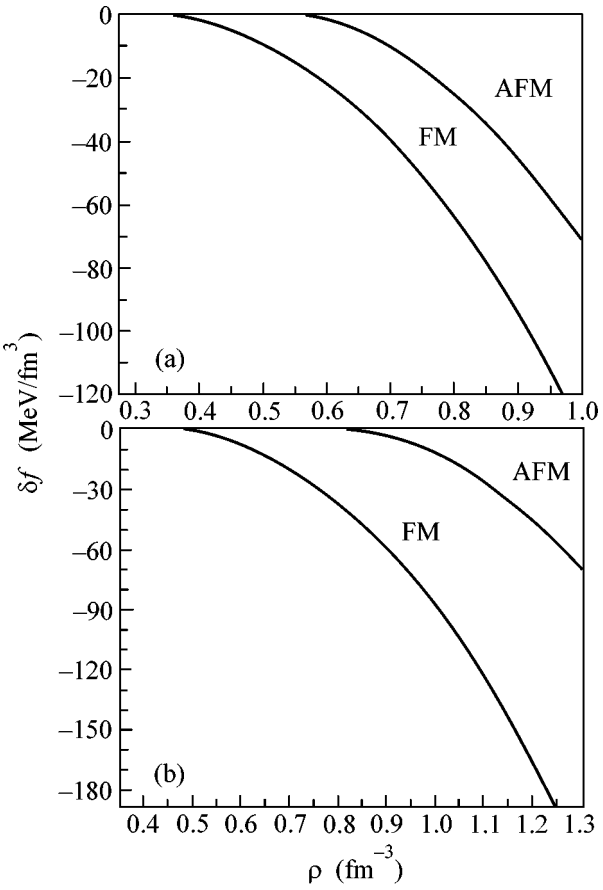

Fig. 3. Same as in Fig. 1, but for the free-energy density, which is measured from the normal-state density, for FM and AFM spin orderings.

parameter, respectively. These quantities behave similar to the spin polarization parameters in Fig. 1 with the same critical densities for the appearance and saturation of the order parameters.

To determine which of the solutions is thermodynamically preferable in the density region, where the FM and AFM solutions of the self-consistency equations coexist, it is necessary to compare the free energies of both states. Figure 3 shows the results of calculations of the free-energy density measured from the free-energy density of the normal state. It is seen that the FM spin ordering is preferable over the AFM ordering over the entire coexistence range. Moreover, the difference between the corresponding free energies increases with density. Therefore, there is no reason to expect that AFM spin ordering can be preferable for higher densities.

In summary, the possibility of spontaneous appearance of spin polarized states in symmetric nuclear matter corresponding to the FM and AFM spin orderings was considered in the Fermi liquid formalism, where *NN* interaction is described by the Skyrme effective forces (SkM* and SGII potentials). In contrast to the previous considerations, where the possibility of the arising of FM spin polarized states was analyzed by calculating magnetic susceptibility, the self-consistent equations for the FM and AFM spin polarization parameters were obtained and solved for zero temperature. The FM and AFM order parameters were shown to appear for densities 2–2.75ρ_0 and 3.3–5ρ_0, respectively. In the density range where both types of solutions exist, the FM spin ordering is thermodynamically preferable.

This work was supported by the Ukrainian Center for Science and Technology (grant no. 1480).

REFERENCES

1. M. J. Rice, Phys. Lett. A **29A**, 637 (1969).
2. S. D. Silverstein, Phys. Rev. Lett. **23**, 139 (1969).
3. E. Østgaard, Nucl. Phys. A **154**, 202 (1970).
4. A. Viduarre, J. Navarro, and J. Bernabeu, Astron. Astrophys. **135**, 361 (1984).
5. S. Reddy, M. Prakash, J. M. Lattimer, *et al.*, Phys. Rev. C **59**, 2888 (1999).
6. A. I. Akhiezer, N. V. Laskin, and S. V. Peletminskiĭ, Zh. Éksp. Teor. Fiz. **109**, 1981 (1996) [JETP **82**, 1066 (1996)].
7. S. Marcos, R. Niembro, M. L. Quelle, *et al.*, Phys. Lett. B **271**, 277 (1991).
8. T. Maruyama and T. Tatsumi, Nucl. Phys. A **693**, 710 (2001).
9. M. Kutschera and W. Wojcik, Phys. Lett. B **223**, 11 (1989).
10. P. Bernardos, S. Marcos, R. Niembro, *et al.*, Phys. Lett. B **356**, 175 (1995).
11. V. R. Pandharipande, V. K. Garde, and J. K. Srivatsava, Phys. Lett. B **38B**, 485 (1972).
12. S. O. Bäckmann and C. G. Källman, Phys. Lett. B **43B**, 263 (1973).
13. P. Haensel, Phys. Rev. C **11**, 1822 (1975).
14. I. Vidaña, A. Polls, and A. Ramos, Phys. Rev. C **65**, 035804 (2002).
15. I. Vidaña and I. Bombaci, Phys. Rev. C **66**, 045801 (2002).
16. S. Fantoni, A. Sarsa, and E. Schmidt, Phys. Rev. Lett. **87**, 181101 (2001).
17. A. I. Akhiezer, V. V. Krasil'nikov, S. V. Peletminsky, *et al.*, Phys. Rep. **245**, 1 (1994).
18. A. I. Akhiezer, A. A. Isaev, S. V. Peletminskiĭ, *et al.*, Zh. Éksp. Teor. Fiz. **112**, 3 (1997) [JETP **85**, 1 (1997)].
19. R. K. Su, S. D. Yang, and T. T. S. Kuo, Phys. Rev. C **35**, 1539 (1987).
20. M. F. Jiang and T. T. S. Kuo, Nucl. Phys. A **481**, 294 (1988).
21. A. I. Akhiezer, A. A. Isayev, S. V. Peletminsky, and A. A. Yatsenko, Phys. Rev. C **63**, 021304(R) (2001).
22. A. A. Isayev, Phys. Rev. C **65**, 031302(R) (2002).
23. M. Brack, C. Guet, and H.-B. Hakansson, Phys. Rep. **123**, 275 (1985).
24. V. G. Nguyen and H. Sagawa, Phys. Lett. B **106B**, 379 (1981).

Translated by R. Tyapaev

JETP Letters, Vol. 77, No. 6, 2003, pp. 256–259. Translated from Pis'ma v Zhurnal Éksperimental'noĭ i Teoreticheskoĭ Fiziki, Vol. 77, No. 6, 2003, pp. 305–308.

Two Comments on the Structure Function Approximation for Deep-Inelastic Scattering

É. Kuraev[1], M. Galynskiĭ[2], and A. Il'ichev[3]

[1] *Joint Institute for Nuclear Research, Dubna, Moscow region, 141980 Russia*

[2] *Stepanov Institute of Physics, National Academy of Sciences of Belarus, pr. Fr. Skariny 68, Minsk, 220072 Belarus*

[3] *National Scientific and Educational Center of Particle and High Energy Physics, Belarussian State University, ul. M. Bogdanovich 153, Minsk, 220040 Belarus*

Received September 17, 2002; in final form, February 6, 2003

The mechanism of radiative return to resonance can be effectively used to describe radiative corrections in terms of the Drell–Yan process. The iteration procedure is proposed. It is shown that the $y \longrightarrow 1$ kinematic region can be described in terms of modified structure functions and the Sudakov formfactor, which significantly changes the result obtained both in the lowest order and with allowance for all leading orders of perturbation theory. © *2003 MAIK "Nauka/Interperiodica".*

PACS numbers: 13.60.–r; 13.40.Ks; 14.60.Cd

Comment 1. At present, it is commonly accepted that the deep-inelastic scattering

$$e(p_1) + P(P) \longrightarrow e(p_2) + X(P_x) \tag{1}$$

is most adequately described as the Drell–Yan process (see [1, 2] and references therein) whose cross section with radiative corrections has the form

$$\frac{d^2\sigma^{\rm obs}(p_1, p_2)}{dQ^2 dy} = \int\limits_{z_{1m}}^{1} dz_1 \int\limits_{z_{2m}}^{1} dz_2 \frac{1}{z_2^2} \mathcal{D}(z_1, L)\mathcal{D}(z_2, L) \times \frac{d^2\sigma^{\rm hard}(\tilde{p}_1, \tilde{p}_2)}{d\tilde{Q}^2 d\tilde{y}}, \tag{2}$$

that includes the lowest order correction (see [3]) and leading corrections in all orders of perturbation theory, which enter into the lepton structure functions $\mathcal{D}(z, L)$. Here,

$$L = \ln(Q^2/m_e^2), \quad p_1^2 = p_2^2 = m_e^2, \quad P^2 = M^2, \quad Q^2 = -(p_1 - p_2)^2 \gg m_e^2, \quad y = \frac{2p_1 q}{2p_1 P}, \quad q = p_1 - p_2, \tag{3}$$

The parameters of hard-scattering cross section in the Born approximation are defined as

$$\tilde{p}_1 = z_1 p_1, \quad \tilde{p}_2 = \frac{p_2}{z_2}, \quad \tilde{Q}^2 = \frac{z_1}{z_2} Q^2, \quad \tilde{y} = 1 - \frac{1-y}{z_1 z_2},$$

and the lower integration limits have the form

$$z_{1m} = \frac{1 + z_{\rm th} - y}{1 - xy}, \quad z_{2m} = \frac{1 - y + xyz_1}{z_1 - z_{\rm th}}, \quad z_{\rm th} = \frac{2m_\pi M}{2p_1 P} \ll 1. \tag{4}$$

When calculating the integral in Eq. (2) with respect to energy fraction z_1, one has to take into account two properties of the behavior of the integrand. The basic property is a rapid decrease in cross section with increasing Q^2:

$$\frac{d\sigma^{\rm hard}}{dQ^2 dy} = \frac{1}{[1 - \Pi(Q^2)]^2} \frac{d\sigma_{\rm B}}{dQ^2 dy}\left(1 + \frac{\alpha}{\pi} K\right), \tag{5}$$

where

$$\frac{d\sigma_{\rm B}}{dQ^2 dy} = \frac{4\pi\alpha^2}{Q^4 y} \times \left[\left(1 - y - x^2 y^2 \frac{M^2}{Q^2}\right) F_2(x, Q^2) + xy^2 F_1(x, Q^2)\right] \tag{6}$$

is the Born cross section, $\Pi(Q^2)$ is the polarization operator of a virtual photon, and the explicit expressions for the K factor can be found in [2].

0021-3640/03/7706-0256$24.00

The other region of enhancing contributions is determined by the slow increase in the structure functions for near-unity energy fractions:

$$\mathcal{D}(z_1, L) \approx \beta(1-z_1)^{-1+\beta} \approx \delta(1-z_1),$$
$$\beta = \frac{2\alpha}{\pi}(L-1). \tag{7}$$

The first of the two competing tendencies dominates.

Let us represent the right-hand side of Eq. (2) in the form

$$\int_{z_{1m}}^{1} \frac{dz_1}{z_1^2}\Psi(z_1) = \left(\frac{1}{z_{1m}} - 1\right)\Psi(z_{1m}) + \int_{z_{1m}}^{1} \frac{dz_1}{z_1}(1-z_1)\frac{d}{dz_1}\Psi(z_1), \tag{8}$$

where integration by parts is carried out. The second term on the right-hand side of Eq. (8) is smaller than the first term by an order of magnitude if $z_{2m} \ll 1$. Enhancing tendencies in the integrand of the second term on the right-hand side of Eq. (8) are identical: $\beta z_1^{-1}(1-z_1)^{-1+\beta}$.

The integration with respect to z_2 is determined by the only tendency that is associated with the structure function $\mathcal{D}(z_2, L) \sim \delta(1-z_2)$, which is beyond the scope of this paper.

Based on the cross section written in form (8), an iteration procedure using the direct experimental data for Ψ can be constructed.

Comment 2. Experimental data on deep-inelastic scattering for $1 - y \ll 1$ are usually not analyzed, because the lowest order radiative corrections are large and can even exceed 100% in this region [3]. Additional inclusion of the leading radiative corrections in all-order perturbation theory (2) makes the situation worse rather than better [2]. For these reasons, experimental data in the region $y > 0.8$ are not analyzed.

A rather accurate expression for the cross section for large y, including radiative corrections, can be obtained by using the modified form of the structure functions and introducing the Sudakov suppressing formfactor that is characteristic for this region.

To this end, we consider radiative corrections of the two lowest orders of the perturbation theory. Along with contributions from the emission of virtual photons, it is necessary to take into account contributions from the emission of low-energy (soft) real photons and pairs of charged particles with energies $\Delta\varepsilon \ll \varepsilon$ on the order of the scattered-lepton energy ε_2:

$$\Delta\varepsilon \sim \varepsilon_2 = \varepsilon(1-y) \ll \varepsilon_1 = \varepsilon. \tag{9}$$

Cross section including the first and second-order radiative corrections is expressed in terms of the Born cross section as

$$\frac{d\sigma^{\text{obs}}}{dydQ^2} = \left[1 + \frac{\alpha}{\pi}\Delta^{(1)} + \left(\frac{\alpha}{\pi}\right)^2\Delta^{(2)} + \ldots\right]\frac{d\sigma_{\text{B}}}{dydQ^2}. \tag{10}$$

The lowest order contribution has the form

$$\Delta^{(1)} = (L-1)\left(\ln\frac{\Delta\varepsilon}{\varepsilon_1} + \ln\frac{\Delta\varepsilon}{\varepsilon_2}\right) + \frac{3}{2}L - \frac{1}{2}\ln^2(1-y) - \frac{\pi^2}{6} - 2 + \text{Li}_2\left(\frac{1+\cos\theta}{2}\right), \tag{11}$$

where θ and ε_2 are the scattering angle and energy of the scattered lepton in the laboratory system. According to the above argumentation concerning the energy of soft real photons and pairs, we can use the approximation

$$\ln\frac{\Delta\epsilon}{\epsilon_1} + \ln\frac{\Delta\epsilon}{\epsilon_2} = \ln(1-y). \tag{12}$$

The leading terms in $\Delta^{(1)}$ involving L are associated with the known Δ part of the kernel of evolution equation for the structure function:

$$P^{(1)}(x) = \lim_{\Delta\to 0}\left\{\delta(1-x)P_\Delta^{(1)} + \theta(1-x-\Delta)\frac{1+x^2}{1-x}\right\}. \tag{13}$$

For the case under consideration, the θ part $P_\theta^{(1)}(x)$ corresponding to the emission of hard collinear photons does not contribute (the dominant energy part of initial lepton is transferred to hadrons). Indeed, when the initial electron emits a hard photon, the magnitude of the squared 4-momentum transfer to the hadron is too low: $Q_1^2 \sim \varepsilon^2(1-y)^2 \ll Q^2 = 2\varepsilon^2(1-y)(1-\cos\theta)$. Moreover, we can take the parameter Δ as $1 - y$.

Assumption (9) concerning the energies of soft particles results in a certain modification of $P_\Delta^{(1)}$:

$$P_\Delta^{(1)} = 2\ln\Delta + \frac{3}{2} \longrightarrow \left(2\ln(1-y) + \frac{3}{2}\right) - \ln(1-y). \tag{14}$$

The second-order correction can be represented as the sum of contributions from the emission of photons (virtual and real) and formation of pairs of charged particles (virtual and real) $\Delta^{(2)} = \delta_{\gamma\gamma} + \delta_{sp}$. Replacing the fine-structure constant by the "running" constant, we can only consider contributions from photons.

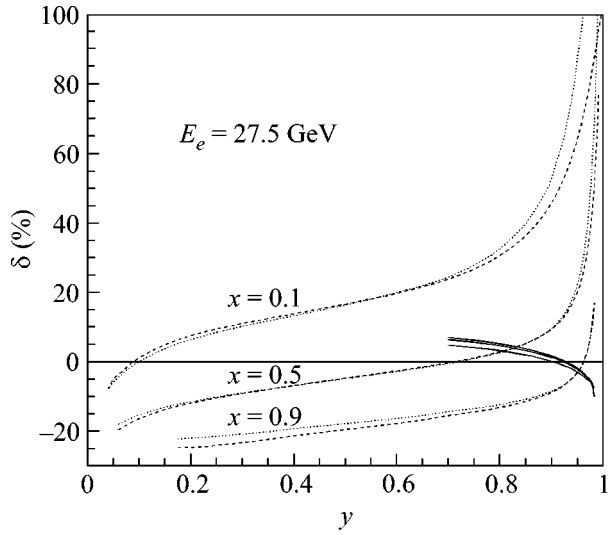

The quantity δ (22) vs. y in the HERMES experiment kinematics for (solid lines) radiative corrections determined by Eq. (21), (dashed lines) first-order radiative corrections from the inelastic spectrum, and (dotted lines) radiative corrections from the inelastic spectrum calculated by Eq. (2).

The contribution to the radiative corrections from the emission of virtual and real photons has the form

$$\delta_{\gamma\gamma} = \frac{1}{2}(\Delta^{(1)})^2 - \frac{\pi^2}{3}(L-1)^2 + \frac{3}{2}L\left(2 + \frac{\pi^2}{6} - \mathrm{Li}_2\left(\frac{1+\cos\theta}{2}\right)\right) + O(1), \quad (15)$$

where the first two terms for $y = 0$ agree with the prediction of the evolution equations for the structure functions [4]. The first term involves expressions such as $\ln^2(1-y)$ and $L\ln(1-y)$, which present the suppression of cross section due to the Sudakov formfactor mechanism. These terms are substantial in the $y \longrightarrow 1$ limit.

Introducing the additional integration

$$\int d\tilde{Q}^2 \delta((z_1 x Q^2/z_2) - \tilde{Q}^2), \quad x = 1 - (\Delta\epsilon/\epsilon) \quad (16)$$

to the right-hand side of Eq. (2), we consider the cross section for deep-inelastic scattering averaged over a small interval $\tilde{Q}^2 \sim Q^2$. Small variations in the momentum transfer occur due to the emission of photons (virtual and real). Since the hard-scattering cross section is smooth in this range, the cross sections with and without radiative corrections have the form

$$\frac{d\sigma^{\mathrm{obs}}}{dydQ^2} = \frac{F(x,L)}{[1-\Pi(Q^2)]^2}\frac{d\sigma_{\mathrm{B}}}{dydQ^2}\left(1 + \frac{\alpha}{\pi}K\right), \quad (17)$$

where

$$F(x,L) = \iint dz_1 dz_2 \mathcal{D}(z_1,L)\mathcal{D}(z_2,L)\theta(xz_1 - z_2). \quad (18)$$

Using the following differential evolution equations for the nonsinglet structure function $\mathcal{D}(x, L)$:

$$\frac{\partial\mathcal{D}}{\partial L} = \frac{\alpha(Q^2)}{2\pi}\int_x^1 \frac{dy}{y}P^{(1)}\left(\frac{x}{y}\right)\mathcal{D}(y,L),$$

$$\mathcal{D}(y,0) = \delta(1-y),$$

where $\alpha(Q^2) = \alpha/[1 - \Pi(Q^2)]$ is the running coupling constant, we arrive at the following differential equation for $F(x, L)$:

$$\frac{\partial F}{\partial L} = \frac{\alpha(Q^2)}{\pi}\int_x^1 dz P^{(1)}\left(\frac{\xi}{z}\right)F(z,L), \quad F(x,0) = 1. \quad (19)$$

The solution

$$F(x,L) = \left(\ln\frac{1}{x}\right)^{2\chi}\frac{1}{\Gamma(1+2\chi)}e^{\chi(3/2 - 2C_{\mathrm{E}})}, \quad \chi = -3\ln\left(1 - \frac{\alpha}{3\pi}L\right) \quad (20)$$

to this equation was found in [4] (we are grateful to L.N. Lipatov, who called our attention to works [5], where a similar method was developed).

Terms involving $\ln(1-y)$ were ignored in the above analysis of evolution.

According to the argumentation based on the factorization of infrared divergences in the form of the Yennie–Frauchi–Surra factor [6] and on the Bloch–Nordsick theorem about the change of the logarithm of the lepton-to-"photon" mass ratio to $\ln(\Delta\epsilon/\epsilon)$ (as a result of taking account of the emission of soft particles), the terms involving $\ln(1-y)$ can be taken into account in the form of a universal exponential factor.

Replacing $\ln(1/x) = 1 - y$, we obtain

$$\frac{d\sigma^{\mathrm{obs}}_{y\to 1}}{dQ^2dy} = \frac{1}{[1-\Pi(Q^2)]^2}\frac{d\sigma_{\mathrm{B}}}{dQ^2dy}R\left(1 + \frac{\alpha}{\pi}K\right),$$

$$R = \frac{(1-y)^{2\chi}}{\Gamma(1+2\chi)}\exp\left[\left(\frac{3}{2} - 2C_{\mathrm{E}}\right)\chi\right] \times \exp\left[-\frac{\alpha}{2\pi}\ln(1-y)(\ln(1-y) + 2L)\right], \quad (21)$$

where $C_{\mathrm{E}} = 0.577$ is the Euler constant. This result is consistent with the lower order perturbation calculations given by Eqs. (11) and (15) up to the nonleading terms included in the form of the K factor. Formula (21) takes radiative corrections into account with an accuracy of 1% for $|K| \sim 1$.

To numerically estimate radiative effect, the quantity

$$\delta = \left(\frac{d\sigma^{\text{obs}}}{dydQ^2} \Big/ \frac{d\sigma_{\text{B}}}{dydQ^2} - 1 \right) \qquad (22)$$

is calculated from Eq. (21). The result as a function of y for different values of the Bjorken parameter x is shown in the figure, where the results obtained with the corrections from the inelastic spectrum that are calculated both in the lowest order of perturbation theory and by Eq. (2) with the ESFRAD code [2] are also shown. As for the polelike behavior $1/(1-y)$ obtained in [2], it is due to the hard hadron emission in the initial state and corresponds to small energy transfer to hadron.

This work was supported by the Heisenberg–Landau Foundation. We are grateful to the Scientific Center of Applied Research, JINR and to V.N. Samoĭlov for interest in this work, to V. Fadin and L. Lipatov for stimulating discussions, and to I. Akushevich, who placed the ESFRAD code at our disposal.

REFERENCES

1. É. Kuraev, V. Fadin, and N. Merenkov, Yad. Fiz. **47**, 1593 (1988) [Sov. J. Nucl. Phys. **47**, 1009 (1988)].
2. A. Afanasev, I. Akushevich, and N. Merenkov, hep-ph/0111331 (2001).
3. A. Akhundov, D. Bardin, and N. Shumeĭko, Yad. Fiz. **44**, 1517 (1986) [Sov. J. Nucl. Phys. **44**, 988 (1986)].
4. É. Kuraev and V. Fadin, Yad. Fiz. **41**, 733 (1985) [Sov. J. Nucl. Phys. **41**, 466 (1985)].
5. V. Gribov and L. Lipatov, Yad. Fiz. **15**, 781 (1972) [Sov. J. Nucl. Phys. **15**, 438 (1972)]; Yad. Fiz. **15**, 1218 (1972) [Sov. J. Nucl. Phys. **15**, 675 (1972)].
6. D. Yennie, S. Frauchi, and H. Suura, Ann. Phys. (N.Y.) **13**, 379 (1961).

Translated by R. Tyapaev

JETP Letters, Vol. 77, No. 6, 2003, pp. 260–265. From Pis'ma v Zhurnal Éksperimental'noĭ i Teoreticheskoĭ Fiziki, Vol. 77, No. 6, 2003, pp. 309–313.

Feigenbaum Universality in String Theory¶

I. I. Kogan[1, 2] and D. Polyakov[3]

[1] *Theoretical Physics, Department of Physics, Oxford University, Oxford, OX1 3NP, UK*

[2] *Institute of Theoretical and Experimental Physics, Moscow, 117259 Russia*

[3] *Department of Physical Sciences, University of Helsinki and Helsinki Institute of Physics, FIN-00014 Helsinki, Finland*

e-mail: i.kogan@physics.ox.ac.uk, polyakov@pcu.helsinki.fl

Received December 23, 2002; in final form, February 10, 2003

Brane-like vertex operators, defining backgrounds with ghost-matter mixing in NSR superstring theory, play an important role in the world-sheet formulation of D-branes and M theory as creation operators for extended objects in the second quantized formalism. In this paper, we show that the dilaton beta function in ghost-matter mixing backgrounds becomes stochastic. The renormalization group (RG) equations in ghost-matter mixing backgrounds lead to non-Markovian Fokker–Planck equations whose solutions describe superstrings in curved space-times with brane-like metrics. We show that the Feigenbaum universality constant $\delta = 4.669\ldots$, describing transitions from order to chaos in a huge variety of dynamical systems, appears analytically in these RG equations. We find that the appearance of this constant is related to the scaling of relative space-time curvatures at fixed points of the RG flow. In this picture, the fixed points correspond to the period doubling of Feigenbaum iteration schemes. © *2003 MAIK "Nauka/Interperiodica".*

PACS numbers: 11.25.Uv; 11.25.Hf; 11.10.Hi; 05.45.-a

Superstring theory is our current hope to put gravity in a Prokrust bed of quantum mechanics. In spite of all the spectacular progress in the last quarter century [1], the full structure and underlying symmetries of the theory have yet to be unveiled. One of the most striking features of string theory is the deep relation between renormalization group (RG) flows on a world sheet and evolution in a target space. Critical points of these RG flows, described by 2D conformal field theories (CFT), determine equations of motion in a target space. The structure of these equations is determined by the world-sheet correlation functions of the appropriate vertex operators in respective CFT [2]. The conformal field theory description of strings in curved backgrounds, such as of strings in the presence of branes, as well as the underlying CFT of strongly coupled strings, is a much harder problem to tackle, in particular because adequate knowledge of quantum degrees of freedom of M-theory and nonperturbative strings is still lacking. Some time ago, we proposed a formalism [3–6] that describes the nonperturbative dynamics of solitons in string and M-theory in terms of a special class of vertex operators, called brane-like states. The crucial distinction of these vertex operators from usual ones (such as a photon or a graviton) is that they exist at nonzero ghost pictures only. A simplest example of these vertices in the closed string case is given by (before integration over the world-sheet)

$$\begin{aligned} V_5^{(-3)}(q) &= e^{-3\phi-\bar{\phi}}\psi_{t_1}\ldots\psi_{t_5}\bar{\psi}_{t_6}e^{iq_aX_a}(z,\bar{z}),\\ V_5^{(-2)}(q) &= c\partial\chi e^{\chi-3\phi-\bar{\phi}}\psi_{t_1}\ldots\psi_{t_5}\bar{\psi}_{t_6}e^{iq_aX_a}(z,\bar{z}),\\ V_5^{(+1)}(q) &= e^{\phi-\bar{\phi}}\psi_{t_1}\ldots\psi_{t_5}\bar{\psi}_{t_6}e^{iq_aX_a}(z,\bar{z}) + b - c \text{ ghosts},\\ a &= 0,\ldots,3; \quad t_i = 4,\ldots,9. \end{aligned} \tag{1}$$

It is important that the discrete picture-changing gauge symmetry is broken for such operators and that their superconformal ghost dependence cannot be removed by any picture-changing transformation. We shall refer to this property of the brane-like vertices as the ghost-matter mixing. The crucial property of these special vertex operators is that they do not correspond to any perturbative string excitation but describe the nonperturbative dynamics of extended solitonic objects, such as D-branes.

In [6], we showed that the low-energy effective action of the sigma-model with the brane-like states is given by the DBI action for D-branes. From the world sheet point of view, this means that the insertion of vertices with the ghost-matter mixing makes the deform CFT describing strings in flat space-time, and it flows to a new fixed point, corresponding to the CFT of strings in a curved background induced by D-branes. In this paper, we shall further investigate RG flows in the ghost-matter mixing backgrounds. It appears that the

¶ This article was submitted by the authors in English.

properties of these RG flows are stunningly different from the usual ones. We found that ghost-matter mixing adds to RG flow operator-valued stochastic terms. Even more intriguing is the emergence of a universal constant in the RG equations, which with an accuracy less than 0.5%, is just the logarithm of the famous Feigenbaum constant $\delta = 4.669$ [7]. This coincidence is not accidental but reflects remarkable and new relations between superstrings, chaos, gravity, and stochastic processes, which is the subject of this letter.

The crucial property of world-sheet conformal beta-functions (e.g., of a dilaton) in ghost-matter mixing backgrounds is the presence of stochastic terms in the RG equations. One specific property of the brane-like states is that their OPE algebra is picture-dependent. This picture dependence leads to nondeterministic stochastic terms in the dilaton beta-function. Namely, consider the NSR sigma model in $D = 10$ perturbed by the dilaton and the ghost-matter mixing vertex (1). The generating functional for this model is

$$\begin{aligned} Z(\varphi, \lambda) = \int DXD\psi D[\text{ghosts}] : f(\Gamma) :: f(\bar{\Gamma}) : \\ \times \exp\{-S_{NSR} + \int d^4q\lambda(q)\int d^2z V_5(q, z, \bar{z}) \\ + \int d^{10}p\varphi(p)\int d^2w V_\varphi^{(-2)}\varphi(p, w, \bar{w})\}. \end{aligned} \tag{2}$$

Here,

$$: f(\Gamma) :=: \frac{1}{1-\Gamma} := 1 + : \Gamma : + : \Gamma^2 : + \ldots$$

is the measure function of picture-changing operator, $: \Gamma :=: e^{\phi}G :$ with $G = G_m + G_{gh}$ being the full matter + ghost world-sheet supercurrent. The dilaton vertex operator can be taken at any negative picture. It is convenient to take V_φ at picture –2 (both left and right), as in this case the dilaton vertex operator is given by

$$V_\varphi(p) = \int d^2z e^{-2\phi - 2\bar{\phi}}\partial X^m \partial X_n(\eta_{mn} - k_m\bar{k}_n - k_n\bar{k}_m).$$

Let us expand the generating functional (2) up to the third order of λ and the second order of φ, which symbolically can be written as (keeping only relevant terms)

$$\begin{aligned} Z = \langle \ldots + \lambda\varphi V_5 V_\varphi + \lambda^2 V_5 V_5 \\ + \varphi^2 V_\varphi V_\varphi + \lambda^3 V_5 V_5 V_5 + \ldots\rangle. \end{aligned} \tag{3}$$

To determine the UV divergences in the partition function (2), relevant to the dilaton beta-function, one has to point out the relevant singular terms in the OPE algebra of the dilaton and V_5. In the on-shell limit, the relevant terms in the operator algebra are given by

$$\begin{aligned} V_5^{(a)}(w_1, \bar{w}_1; q_1)V_5^{(b)}(w_2, \bar{w}_2; q_2) \\ \sim \frac{C_{[-a|b]}(q_1, q_2)V_\varphi^{(a+b)}(q_1 + q_2)}{|z_1 - z_2|^2} + \ldots, \\ a, b = +1, -3, \end{aligned} \tag{4}$$

where

$$\begin{aligned} C_{[-3|-3]}(q_1, q_2) \sim (q_1q_2)(1 + (q_1 + q_2)^2), \\ C_{[-3|1]}(q_1, q_2) \sim (q_1q_2), \\ C_{[-3|1]}(q_1, q_2) \sim (q_1q_2)(1 - (q_1 + q_2)^2). \end{aligned} \tag{5}$$

Next, one has to point out the picture-changing rules for the left part of the V_5 operator, in order to specify how it is acted on by $: f(\Gamma) :$ The picture changing transformation rules for the V_5 operators (1) can be written in the form

$$\begin{aligned} : \Gamma :^n V_5^{(k)}(p) = \alpha_{[k|n+k]}V_5^{(N+k)}(p), \\ \alpha_{[i|j]} = \alpha_{[m|n]} = \alpha_{[n|m]} = 1, \\ \alpha_{[a|j]} = \alpha_{[a|b]} = \alpha_{[s|a]} = 0, \\ \alpha_{[i|m]} = \alpha_{[s|m]} = 1 + p^2, \\ s, t = -\infty, \ldots, -4; \quad i, j = -3, -2; \\ a, b = -1, 0; \quad m, n = 1, 2, \ldots. \end{aligned} \tag{6}$$

In the beta-function calculations, when the vertex operators are taken slightly off-shell, the following identities are useful:

$$\alpha_{[i|m]}C_{[m|n]} = C_{[i|n]}; \quad \alpha_{[i|m]}C_{[m|j]} = C_{[i|j]}. \tag{7}$$

Finally, using the fact that picture-changing operators form the polynomial ring,

$$: \Gamma :^{m+n} =: \Gamma^m\Gamma^n : + [Q_{BRST}, \ldots], \tag{8}$$

the action of the $: \Gamma^n :$ operator on the vertex operators inside the functional integral can be expressed as

$$\begin{aligned} \langle : \Gamma^n :(w)V_1(z_1)\ldots V(z_N)\rangle \\ = \sum_{k_1, \ldots k_N = 0}^{k_1 + \ldots + k_{N-1} = n} N^{-n}\frac{n!}{k_1!\ldots k_{N-1}!(n - k_1 - \ldots - k_{N-1})!} \\ \times \langle : \Gamma :^{k_1}V_1(z_1)\ldots : \Gamma :^{k_{N-1}}V_{N-1}(z_{N-1}) \\ : \Gamma :^{n-k_1-\ldots-k_{N-1}}V_N(z_N)\rangle; \end{aligned} \tag{9}$$

i.e., the correlator does not depend on w. The factor of N^{-n} in (9) ensures the correct normalization of amplitudes in the picture-independent case. Using relations (6)–(9), we are finally in a position to start evaluating the beta-function. The first contribution of interest to

the beta-function comes from the λ^2 term, bilinear in the V_5 operator. At a given picture level n, this term leads to the following divergence in the order of λ^2:

$$\frac{1}{2}\int d^2w_1 d^2w_2 \langle : \Gamma^{n+6} : V_5^{(-3)}(w_1) V_5^{(-3)}(w_2)\ldots\rangle$$
$$= 2^{-n-7}\sum_{k=0}^{n+6}\frac{(n+6)!}{k!(n+6-k)!}\alpha_{[-3|k-3]}C_{[k-3|n+3-k]} \quad (10)$$
$$\times \alpha_{[-3|n+3-k]}\int d^3\xi \langle V_\varphi^{(n)}(\xi,\bar\xi)\ldots\rangle \log\Lambda,$$

where $\xi = 1/2(w_1 + w_2)$, $\eta = 1/2(w_1 - w_2)$ and $\log\Lambda = \int_\Lambda \frac{d^2\eta}{|\eta|^2}$ is the log of the world sheet UV cutoff. For the sake of brevity, we suppress the momentum dependence of fields, vertices, and structure constants here and below. This divergence is removed by renormalizing the dilaton field as

$$\varphi \longrightarrow \varphi - \sum_{n=0}^{\infty} 2^{-n-7}\sum_{k=0}^{n+6}\frac{(n+6)!}{k!(n+6-k)!} \quad (11)$$
$$\times \alpha_{[-3|k-3]}C_{[k-3|n+3-k]}\alpha_{[-3|n+3-k]}\lambda^2\log\Lambda.$$

In the absence of picture-dependence, the sum over k would have been reduced to $\frac{1}{2}C\lambda^2\log\Lambda$ for each picture, as it should be in the standard case, when ghost-matter mixing is absent.

As a result of the dilaton RG flow, the $\lambda\varphi$ cross-term is renormalized by λ^3 logarithmic divergence:

$$\varphi \longrightarrow \varphi - \mathrm{const}\lambda^2\log\Lambda,$$
$$\lambda\varphi V_5 V_\varphi \longrightarrow \lambda\varphi V_5 V_\varphi - \mathrm{const}\lambda^3\log\Lambda V_5 V_\varphi. \quad (12)$$

Using identities (7) relating α and C and after some straightforward transformations, we can cast the renormalization of the $\lambda\varphi$ term under the flow (11) as

$$-\lambda^3\log\Lambda C_{[-3|-3]}\alpha_{[-3|1]}\int d^2w_2 V_\varphi^{(-6)}(w_1)V_5^{(n+6)}(w_2)$$
$$\times\sum_{n=0}^{\infty}\sum_{k,l=0}^{k=n+6;\ l=n+5}\frac{(n+5)!(n+6)!}{k!l!(n+5-l)!(n+6-k)!}, \quad (13)$$

where in the sum over k and l one must have $ak \neq 2, 3, n+3, n+6$; $l \neq n+2, n+3$. This gives the renormalization of the $\lambda\varphi$ cross-term under the RG flow (11) of the dilaton field in the ghost-matter mixing case. The other contribution on the same order of λ^3 to the dilaton beta-function comes from the OPE singularities inside the λ^3 term itself, appearing in the expansion (3) of the partition function. After simple calculations, we get

$$\frac{1}{2}\lambda^3\log\Lambda\sum_{n=0}^{\infty}3^{-n-9}\sum_{k,l=0}^{k+l=n+9}\frac{(n+9)!}{k!l!(n+9-k-l)!}$$
$$\times C\int d^2w_1\int d^2w_2\langle V_\varphi^{(-6)}(w_1)V_5^{(n+6)}(w_2)\ldots\rangle;$$

$$3C = C_{[k-3|l-3]}\alpha_{[-3|k-3]}\alpha_{[-3|n+6-k-l]}\alpha_{[-3|n+6]} \quad (14)$$
$$+ C_{[k-3|n+6-k-l]}\alpha_{[-3|k-3]}\alpha_{[-3|l-3]}\alpha_{[-3|n+6]}$$
$$+ C_{[k-3|n+6-k-l]}\alpha_{[-3|l-3]}\alpha_{[-3|n+6-k-l]}\alpha_{[-3|n+6]}.$$

Again, it is easy to see that, in the absence of the ghost-matter mixing ($\alpha = 1$, all C are picture-independent), this contribution sums to

$$\frac{1}{2}C\lambda^3\log\Lambda\int d^2w_1\int d^2w_2 V(w_1,\bar w_1)V(w_2,\bar w_2); \quad (15)$$

precisely canceling the divergence of the same λ^3 type, originating from the renormalization of the $\lambda\varphi$ cross term under the flow. In the picture-independent case, this ensures that the renormalization (11) of the dilaton field under the flow does not bring about any additional singularities from higher order terms, such as the cubic one and the $\lambda\phi$ cross-term. In particular, this guarantees that terms of the type

$$\sim C\lambda^3\log\Lambda\int_\Lambda d^2w V_5(w,\bar w) \quad (16)$$

never appear in the dilaton or other perturbative close string field beta-functions in the picture-independent case. On the contrary, should terms of this type appear in the beta-function, that would imply that the RG equations become stochastic, since from the point of view of the space-time fields, the world-sheet operator $\int_\Lambda d^2w V_5(w,\bar w)$ is a stochastic random variable, with the cutoff parameter Λ playing the role of the stochastic time. In this case, the RG equations have the form of non-Markovian Langevin equations, where the memory of the noise is determined by the world-sheet correlations of the V_5 operators. This is exactly what happens in the ghost-matter mixing backgrounds, due to the OPE picture dependence. To get the total flow on the λ^3 level, one has to subtract the sum (14) from (12) using identities (7). We obtain

$$\varphi \longrightarrow \varphi + \sigma C_{[-3|-3]}\alpha_{[-3|1]}\lambda^3\log\Lambda\int d^2w V_5^{(-3)}(w,\bar w), \quad (17)$$

where

$$\sigma = 1 - \sum_{n=0}^{\infty}\Big[(n+4)^2(n+5)^3(n+6)2^{-2n-12}$$
$$+\frac{(n+8)(n+9)(n+13)}{96}\left(\frac{2}{3}\right)^{n+9} - ((n+4)^2(n+5)$$
$$+ (1/2)(n+5)^2(n+6))2^{-n-6}\Big] = 1.534. \quad (18)$$

Therefore, the resulting beta-function equations for the dilaton in the ghost-matter mixing background gives (with the momentum dependence restored):

$$\frac{d\varphi(p)}{d\log\Lambda} = -\frac{\delta S_\varphi}{\delta\varphi(p)} + \sigma C(p)\int d^4q\lambda(q)\eta,$$
$$C(p) = \int d^4k C_{[-3|-3]}(p,k)\lambda\left(\frac{k+p}{2}\right)\lambda\left(\frac{k-p}{2}\right), \quad (19)$$
$$\eta = \int\limits_{\Lambda} d^2w V_5^{(-3)}(w,q),$$

with $\sigma = 1.534\ldots$. There are other examples of vertex operators with ghost-matter mixing, and they also lead to stochastic terms in the beta-function of the dilaton. In particular, we have also considered the dilaton field in the background of closed string operators of higher ghost cohomologies:

$$W_5 \sim \int d^2z e^{-4\phi-\bar\phi}\partial X_{(m_1}\ldots\partial X_{m_3)}\bar\Psi_{m_6}e^{ik^\perp X}G_{m_1\ldots m_5m_6}, \quad (20)$$

where the G tensor is symmetric and traceless in $m_1, \ldots, m_5$ (round brackets imply the symmetrization in space-time indices) and $k^\perp$ is transverse to directions $m_1, \ldots, m_6$ and

$$U_5 \sim \int d^2z e^{-4\phi-\bar\phi}\partial X_{(m_1}\ldots\partial X_{m_4)} \times \psi_{m_5}\psi_{m_6}\bar\psi_{m_7}e^{ik^\perp X}G_{m_1\ldots m_7}. \quad (21)$$

We have found that, even though the OPE details are quite different in each case, in the end one nevertheless always gets beta-function equations in the form (19). The crucial point is that the σ factor, reflecting the stochasticity of the beta-function, appears to be universal, and its value is independent of details of the ghost-matter mixing. Namely, we have found [8] $\sigma = 1.541\ldots$ for the W_5 insertion and $\sigma = 1.538\ldots$ for the U_5 case. Even more remarkably, can easily check that in fact

$$\sigma = \ln\delta, \quad (22)$$

where $\delta = 4.669\ldots$ is the famous Feigenbaum universality constant describing the universal scaling of the iteration parameter in a huge variety of dynamical systems under bifurcations and transitions from order to chaos [7].

To understand the physical meaning behind the appearance of the Feigenbaum constant in (19), it is necessary to analyze the non-Markovian Fokker–Planck (FP) equation describing the stochastic process, which can be straightforwardly derived from the Langevin equation (19). We shall present here the FP equation for scaling functions $\lambda(q) = \lambda_0/q^4$

$$\frac{\partial P_{FP}(\varphi,\tau)}{\partial\tau} = -\int d^4p\int d^4q\frac{\delta}{\delta\varphi(p,\tau)}\left(\frac{\delta S_\varphi}{\delta\varphi(q,\tau)}P_{FP}(\varphi,\tau)\right) + \sigma^2\lambda_0^6\int d^4k_1\int d^4k_2\int\frac{d^4p}{p^4}\int\frac{d^4q}{q^4}\int d\xi \quad (23)$$
$$\times\alpha_{-3|1}C_{[-3|-3]}\left(\frac{k_1+p}{2}\right)\alpha_{-3|1}C_{[-3|-3]}\left(\frac{k_2+q}{2}\right) \times\frac{\delta}{\delta\varphi(p,\tau)}G_5(\xi,\tau)\frac{\delta}{\delta\varphi(q,\xi)}P_{FP}(\varphi,\tau),$$

where $\tau = \log\Lambda$ now plays the role of the stochastic time variable. The Green's function $G_5(\xi, \tau, p, q)$ is defined by the cutoff dependence of the two-point correlator of the V_5-vertices:

$$G_5(\xi,\tau) = \int\limits_{\Lambda_1} d^2z\int\limits_{\Lambda_2} d^2w|z-w|^{-4}\delta(p+q) = \left(\frac{1+e^{\xi-\tau}}{1-e^{\xi-\tau}}\right)^2\delta(p+q), \quad (24)$$
$$\xi = \log\Lambda_1, \quad \tau = \log\Lambda_2.$$

We shall look for the anzats solving this equation in the form (for more details, see [3] and references therein)

$$P_{FP}(\varphi,\tau) = \exp[-H_{ADM}(\varphi,\tau)] = \exp\left[-\int d^4p\{g(\tau)(\partial_\tau\varphi)^2 + f(\tau)p^2\varphi^2\}\right]. \quad (25)$$

Substituting this into (23), we find that (25) solves the FP equation provided that the functions $f(\tau)$ and $g(\tau)$ satisfy the following differential equations:

$$g'(\tau) + 4g(\tau) + \frac{\sigma^2\lambda_0^6}{2} = 0,$$
$$\frac{1}{4}f'' + \left(1+\frac{1}{4\tau}\right)f' + \left(1+\frac{1}{4\tau}+\frac{1}{4\sigma^2\lambda_0^6}\left(1-\frac{1}{\tau^2}\right)\right)f \quad (26)$$
$$-\left(1-\frac{1}{\tau^2}\right)\left(e^{-2\tau}+\frac{1}{4\sigma^2\lambda_0^6}\right) = 1.$$

The first equation is elementary; its solution is given by

$$g(\tau) = \frac{\sigma^2\lambda_0^6}{2}(e^{-4\tau}-1), \quad \tau<0. \quad (27)$$

The second equation on $f(\tau)$ can be reduced to a Bessel-type equation by making the substitution

$$f(\tau) = \rho(\tau)e^{-2\tau} + 1/\sigma^2\lambda_0^6.$$

The solution is given by

$$f(\tau) = 1 + \sigma^2\lambda_0^6 e^{-2\tau}(1 + J_{1/\sigma\lambda_0^3}(\tau/\sigma\lambda_0^3)), \quad (28)$$

where $J_1/\sigma\lambda_0^3(\tau/\sigma\lambda_0^3)$ is the Bessel function. In terms of the τ coordinate, the stochastic process, describing the RG flow in ghost-matter mixing backgrounds, evolves in the direction of $\tau = -\infty$. Next, let us study the behavior of Hamiltonian (25), (27), (28) in the conformal limit of $\tau \longrightarrow -\infty$. In this limit, the exponents become very large and, moreover,

$$J_1/\sigma\lambda_0^3\left(\frac{\tau}{\sigma\lambda_0^3}\right) \sim O\left(\frac{1}{\sqrt{\tau}}\right) \ll 1, \quad (29)$$

and after rescaling the Hamiltonian reduces to

$$H(\varphi, \tau) = R^2\int d^4p\{e^{-4\tau}(\partial_\tau\varphi)^2 + p^2e^{-2\tau}\varphi^2\}, \quad (30)$$

which is just the ADM Hamijtonian for the AdS_5 gravity in the temporal gauge [9]; it is easy to see that the λ_0^6 parameter has the meaning of the square of the radius R^2 of the metric.

Let us now analyze in more detail the solution (25), (27), (28) of the non-Markovian FP equation, leading to a new space geometry. Let us note first of all that the limit $\lambda_0 \longrightarrow 0$ is not the same as $\lambda_0 = 0$ (ghost-matter mixing absent). The RG flow described by the effective metric (27), (28) must be single-valued; since Bessel functions at zero argument are single-valued for the integer orders only, this leads to the quantization condition

$$(\sigma\lambda_0^3)^{-1} = N. \quad (31)$$

Moreover, since $J_\nu(\tau) \sim \tau^\nu$ as $\tau \longrightarrow 0$, the absence of a physical singularities at $\tau = 0$ requires N to be positive. The quantization condition (31) implies that

$$((\lambda_0)_N)^{-3} = N\sigma, \quad e^{(\lambda_0)_N^{-3}} = \delta^N, \quad (32)$$

implying the iteration law

$$\frac{e^{(\lambda_0)_{N+1}^{-3}} - e^{(\lambda_0)_N^{-3}}}{e^{(\lambda_0)_N^{-3}} - e^{(\lambda_0)_{N-1}^{-3}}} = \delta, \quad (33)$$

where δ is the Feigenbaum number.

Therefore, the Feigenbaum iteration rule (33) determines the scaling of characteristic curvatures of geometries emerging at the fixed points of the stochastic renormalization group. The role of iteration parameter characterizing the bifurcations is played by $\sim e^{-1/R^2}$, vanishing at $R = 0$ and being finite at large R, as should be the case for the scaling parameter of the Feigenbaum iteration scheme.

From the quantization condition (31), it is clear that the stochastic renormalization group (19) has fixed points for $0 < \lambda_0 < 1$, i.e., that correspond to large curvatures. Moreover, the period doubling that lead to the transition to chaos corresponds to $N \longrightarrow \infty$, i.e., $\lambda_0 \longrightarrow 0$, which is a singularity. So we have reached the amazing conclusion that, precisely near the singularity, our RG flow becomes chaotic. It is tempting to assume that this may be the mechanism that can solve the problem of singularities in string theory.

In this letter, we discussed how matter-ghost mixing can radically modify the nature of the world sheet RG flows and lead to the emergence of chaos near curvature singularities. Here we analyzed only dilaton evolution, but a similar picture can be obtained for other mass-less fields, for example metric [8].

Amusingly, recently the chaotic behavior of metric was discussed in [10] (for earlier papers, see [11] and references therein), where the emergence of chaos in supergravity near a cosmological singularity was demonstrated in the presence of higher rank antisymmetric tensor fields, i.e., *R–R* fields. It will be extremely interesting to understand how chaos emerging during cosmological evolution in supergravity can be related to the chaotic nature of RG flows in underlying string theory in the presence of the sources of the background *R–R* fields.

It is tempting to assume that the resolution of the singularities problem is a transition to chaos and emergence of smooth distributions of fields not restricted on-shell. One can imagine that the curvature R is some new "Reynolds" number in string theory and for large R one has a transition to chaotic behavior in a fashion similar to hydrodynamics, where there is a transition from a laminar to a turbulent flow. These ideas definitely need further investigation.

I.K. is supported in part by PPARC rolling grant PPA/G/0/1998/00567 and EC TMR grant nos. HPRN-CT-2000-00152 and HRRN-CT-2000-00148. D.P. acknowledges the support of the Academy of Finland under project no. 54023, and both I.K. and D.P. acknowledge interesting discussions with T. Damour and the hospitality of Institute des Hautes Etudes Scientifiques (IHES) in Bures-sur-Yvette, where part of this work was done.

The paper is dedicated to the 80th birthday of Karen Avetovich Ter-Martirosyan.

REFERENCES

1. A. M. Polyakov, *Gauge Fields and Strings* (Harwood Academic, Chur, Switzerland, 1987); M. B. Green, J. H. Schwarz, and E. Witten, *Superstring Theory* (Cambridge Univ. Press, Cambridge, 1987), Vols. 1, 2; J. Polchinski, *String Theory* (Cambridge Univ. Press, Cambridge, 1998), Vol. 1, 2.
2. D. Fiedan, Phys. Rev. Lett. **45**, 1057 (1980); Ann. Phys. (N.Y.) **163**, 318 (1985); E. S. Fradkin and A. A. Tseytlin, Nucl. Phys. B **261**, 1 (1985); C. G. Callan, D. Friedan, E. J. Martinec, and M. J. Perry, Nucl. Phys. B **262**, 593 (1985); C. G. Callan and Z. Gan, Nucl. Phys. B **272**, 647

(1986); A. B. Zamolodchikov, Pis'ma Zh. Éksp. Teor. Fiz. **43**, 565 (1986) [JETP Lett. **43**, 730 (1986)]; Yad. Fiz. **46**, 1819 (1987) [Sov. J. Nucl. Phys. **46**, 1090 (1987)].

3. D. Polyakov, Class. Quantum Grav. **18**, 1979 (2001); arXiv:hep-th/0005094.
4. I. I. Kogan and D. Polyakov, Int. J. Mod. Phys. A **16**, 2559 (2001); arXiv:hep-th/0012128.
5. D. Polyakov, Phys. Rev. D **65**, 084041 (2002); arXiv:hep-th/0111227.
6. I. I. Kogan and D. Polyakov, arXiv:hep-th/0208036.
7. M. J. Feigenbaum, J. Stat. Phys. **19**, 25 (1978).
8. I. I. Kogan and D. Polyakov (in press).
9. J. de Boer, E. Verlinde, and H. Verlinde, J. High Energy Phys. **0008**, 003 (2000); arXiv:hep-th/9912012.
10. T. Damour and M. Henneaux, Phys. Rev. Lett. **85**, 920 (2000); hep-th/0003139; Phys. Rev. Lett. **86**, 4749 (2001); hep-th/0012172; Gen. Relativ. Gravit. **32**, 2339 (2000); T. Damour, M. Henneaux, B. Julia, and H. Nicolai, Phys. Lett. B **509**, 323 (2001); arXiv:hep-th/0103094; T. Damour, M. Henneaux, and H. Nicolai, Phys. Rev. Lett. **89**, 221601 (2002); arXiv:hep-th/0207267; T. Damour, Int. J. Mod. Phys. A **17**, 2655 (2002).
11. V. D. Ivashchuk and V. N. Melnikov, J. Math. Phys. **41**, 6341 (2000); arXiv:hep-th/9904077.

JETP Letters, Vol. 77, No. 6, 2003, pp. 266–269. Translated from Pis'ma v Zhurnal Éksperimental'noĭ i Teoreticheskoĭ Fiziki, Vol. 77, No. 6, 2003, pp. 314–318.

Cherenkov Superradiance with a Peak Power Higher than Electron Flow Power

A. A. El'chaninov[1], S. D. Korovin[1], V. V. Rostov[1,*], I. V. Pegel'[1], G. A. Mesyats[2], M. I. Yalandin[2], and N. S. Ginzburg[3]

[1] *High Current Electronics Institute, Siberian Division, Russian Academy of Sciences, Akademicheskiĭ pr. 4, Tomsk, 634050 Russia*

* *e-mail: rostov@lfe.hcei.tsc.ru*

[2] *Institute of Electrophysics, Ural Division, Russian Academy of Sciences, ul. Komsomol'skaya 34, Yekaterinburg, 620083 Russia*

[3] *Institute of Applied Physics, Russian Academy of Sciences, ul. Ul'yanova 46, Nizhni Novgorod, 603600 Russia*

Received February 4, 2003

The results of theoretical and experimental studies allowing the use of Cherenkov superradiance for the generation of electromagnetic pulses with a peak power higher than electron flow power are reported. For an injection current of 2.6 kA and a particle energy of 330 keV, the power of a microwave pulse with a carrier frequency of 9.3 GHz and a duration of 0.5 ns attained 1.2 GW. © *2003 MAIK "Nauka/Interperiodica".*

PACS numbers: 41.60.Bq; 84.40.Fe

Superradiance (SR) of finite-duration electron flows provides an example of a nonstationary collective process that is pertinent to various mechanisms of stimulated radiation of charged particles [1–7]. The highest peak power was obtained for the Cherenkov radiation [8, 9] of rectilinearly moving electrons in a periodic retarding system and their synchronous interaction with the spatial wave harmonic whose energy flux was directed toward the translatory particle motion. The peak power levels obtained for the millimeter and centimeter ranges exceeded (by almost an order of magnitude [9]) the power level of rather extended electron current pulses in the quasi-stationary generation regime. In essence, these works realize classical analogues of the effect that is known in quantum electronics as the Dicke SR [10]. The main difficulty in its application to two-level systems is caused, as is known, by the relaxation processes [11]. The conditions at which the relaxation time exceeds the pulse de-excitation time have been attained only for a narrow class of active media [12]. Estimates show that the collision effects can be ignored for electron flows in vacuum [13]. Therefore, the SR effect can be realized only with a rather high instability increment: $\mathrm{Im}(\omega)L/V_0 \gg 1$ (L is the interaction length and V_0 is the initial particle velocity). In the case of particle interaction with a counterpropagating wave, there is a certain time interval $t_a = L(1/V_0 + 1/|V_g|)$ corresponding to energy accumulation in the wave, where V_g is the wave group velocity. If the beam current duration is close to t_a, almost all beam electrons can be involved in the formation of a counterpropagating solitary electromagnetic pulse. The SR pulse duration can be estimated as a value inversely proportional to the absolute instability increment [14, 15] that appears in the system upon the injection of a stationary electron flow: $\mathrm{Im}(\omega) \approx C\omega_0/(1 + V_0/|V_g|)$, where C is the amplification coefficient (Pierce parameter) and ω_0 is the precise matching frequency between particles and synchronous spatial harmonic ($\omega_0 - h_s V_0 = 0$, where h_s is the harmonic longitudinal wavenumber):

$$\Delta t \approx \frac{1 + V_0/|V_g|}{\omega_0 C}. \qquad (1)$$

In the cases where the SR pulse duration Δt is small compared to the energy accumulation time, $\Delta t \ll t_a$, the SR pulse peak power can exceed (even appreciably) the electron flow power. This is not contradictory to the energy conservation law, because the SR pulse energy is still lower than the total kinetic energy of electron flow.

In this communication, the results of theoretical analysis corroborating this possibility and the results of the experiment on SR pulse generation in the range of 10 GHz with a power 1.4 times higher than the electron beam power are reported.

We assume that the amplification coefficient is small; i.e., $C \ll 1$, which, on the one hand, provides a rather narrow spectral width ($\Delta\omega \sim C\omega_0$), as compared to the finite passband of a real retarding system and, on the other hand, allows the description of the interaction process within the framework of the method of slowly varying amplitudes. Let us represent the longitudinal

field component of the synchronous harmonic with the tubular beam radius r_b as

$$E_z = \chi(z)\mathrm{Re}(\hat{E}(r_b)A(t,z)\exp[i\omega_0(t-z/V_0)]). \quad (2)$$

Here, A is the slowly varying fundamental-harmonic complex amplitude and $\hat{E}$ is a function describing the field transverse distribution. The function χ accounts for the ratio between the synchronous and fundamental amplitudes; it varies with changing corrugation amplitude along the length L and satisfies the normalization condition $\int_0^L \chi(z)dz = L$. In the case of a homogeneous coupling impedance, $\chi = 1$. Without regard for the wave dispersion, the equations describing the one- dimensional unidirectional (without stops and turns) particle motion and the evolution of wave amplitude can be written in the form

$$\frac{\partial^2\theta}{\partial\xi^2} = \gamma_0^3\left[\left(1+C\frac{\partial\theta}{\partial\xi}\right)^2-(1-\gamma_0^{-2})\right]^{\frac{3}{2}}\chi(\xi)\mathrm{Re}(ae^{i\theta}),$$

$$\frac{\partial a}{\partial\tau}-\frac{\partial a}{\partial\xi} = \chi(\xi)J, \quad (3)$$

$$\theta(0) = \theta_0 \in (0, 2\pi), \quad \partial\theta/\partial\xi|_{\xi=0} = 0,$$

$$a(\tau, \xi_k) = 0, \quad a(0, \xi) = a_0(\xi).$$

Here, $\theta = \omega_0(t - z/V_0)$ is the particle phase in the synchronous field, $\gamma_0 = (1 - V_0^2/c^2)^{-1/2}$ is the initial value of relativistic factor,

$$\tau = \omega_0 C(t - z/V_0)/(1 + V_0/|V_g|),$$

$\xi = \omega_0 Cz/V_0$, $a = eA/C\gamma_0^3 V_0 m\omega_0$, and $J = \frac{1}{\pi}\int_0^{2\pi} e^{-i\theta}d\theta_0$ is the dimensionless amplitude of rf current. For $\chi = 1$, Eqs. (3) contain two independent parameters: normalized interaction length $\xi_k = \omega_0 CL/V_0$ and the Pierce parameter $C = (eJ_bZ/2mc^2\gamma_0^3)^{1/3}$, where J_b is the beam current; e and m are electron charge and mass, respectively; c is the speed of light; and Z is the beam–wave coupling impedance [13] (in the case of an inhomogeneous system, it should be taken for the average corrugation amplitude). In addition to ξ_k and C, there are another two parameters whose choice is restricted by the conditions of a particular experiment; these are γ_0 and the initial noise level that, for high-current beams, is determined by the current front radiation [14]. The particular form of the function $a_0(\xi)$ in Eq. (3) is found by a nonselfconsistent method from the known current front profile, e.g., using the initial calculation step with a given rf current $J^f \ll 1$. For an arbitrary $\xi_k \gg 1$, the optimal level of initial perturbations should be that for which the region where the rf current amplitude is restricted by the nonlinearity (particle rearrangement) is near the edge of the interaction space. In this case, the SR-pulse formation time at the output of the system

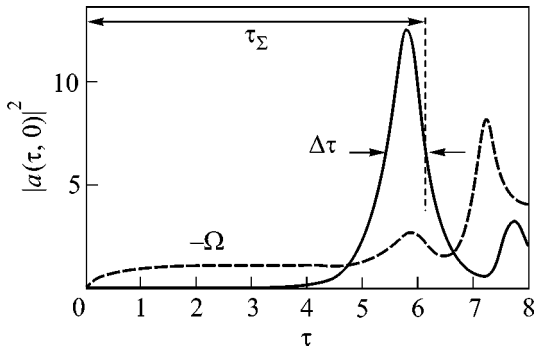

Fig. 1. The calculated pulse shape and the running frequency shift taken with minus sign (dashes) for $\xi_k = 6$, $\nu = 0.5$, $J^f = 0.003$, and $\gamma_0 \gg 1$.

($z = 0$) is found from the expression $\tau_\Sigma \approx \xi_k$ (Fig. 1), i.e., equal to the sum of the particle- and wave-transit times through the interaction space. If, for a given ξ_k, the initial perturbation is larger than its optimal value, the pulse forms within a shorter time and has a lower power, so that the rf current is saturated before a particle pass through the full interaction length. If the initial perturbation is small, the pulse appears later, and its amplitude is independent of J^f. Figure 1 shows the typical form of the SR-pulse envelope amplitude at the system output ($z = 0$) and the running frequency detuning $\Omega = d(\arg a)/d\tau$ from the exact matching frequency.

Let us define the conversion ratio as the ratio of peak radiation power to the electron flow power:

$$K = \frac{(\gamma_0+1)}{\gamma_0}\frac{\nu|A(\tau,0)|^2_{\max}}{8}, \quad \nu \equiv 2\gamma_0^2 C. \quad (4)$$

The introduction of the generalized nonlinearity parameter ν allows one to represent the results for various γ_0 in a simpler form, because the influence of initial particle energy can be taken into account using the similarity relations [16]. One can see in Fig. 2 that the conversion ratio is maximal for the nonrelativistic particles and is equal to about 1.4 for the parameters $\nu \approx \nu_{cr} \approx 0.35$ and $\xi_k \approx 10$. The critical values of nonlinearity parameter correspond to the appearance of stopping electrons, for which the model no longer applies. In the ultrarelativistic approximation, electrons do not stop ($K \longrightarrow 1$ for $\nu \approx 1$ and $\xi_k \longrightarrow \infty$). The asymptotic limit $\nu \longrightarrow 0$ corresponds to the regime of small relative changes in particle energies, for which the SR pulse duration is maximal and close to estimate (1). The fact that the duration decreases for high ν values is explained by a change in the pulse shape as a result of shortening the particle rearrangement step.

Note that the increase in the SR peak power can be achieved by choosing an appropriate profile for the coupling parameter along the interaction length. In particular, in the experiment described below, the coupling parameter increases linearly (by 1.6 times) at the first

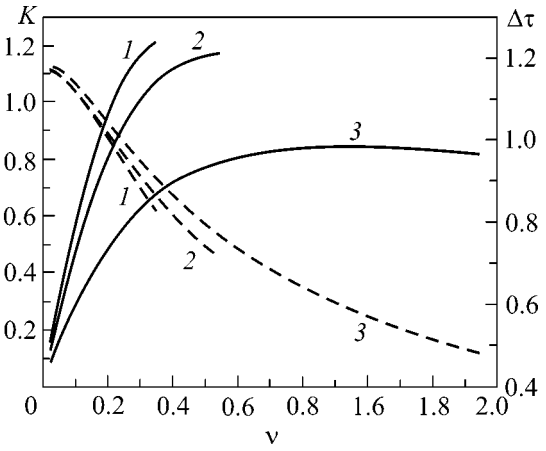

Fig. 2. Conversion ratio (solid lines) and normalized pulse duration (dashed lines) as functions of the nonlinearity parameter: (*1*) $\gamma_0 - 1 \ll 1$, (*2*) $\gamma_0 = 1.6$, and (*3*) $\gamma_0 \gg 1$ ($\xi_k = 6$ and $J^f = 0.003$).

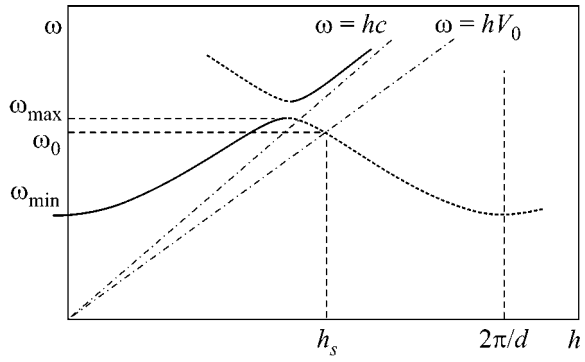

Fig. 3. Dispersion characteristic of a corrugated waveguide (with period *d*).

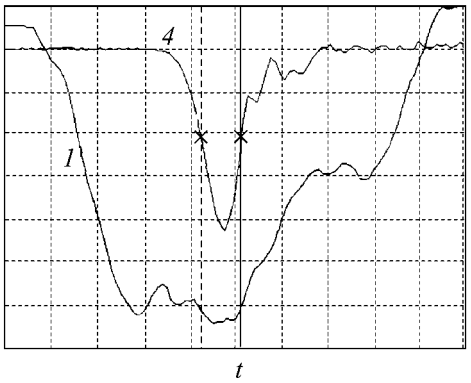

Fig. 4. Oscillograms of the accelerating voltage pulses (channel *1*) and a signal recorded by a microwave hot-carrier detector (channel *4*; signal duration is indicated by vertical cursors). Resolution: 1 ns per mesh.

half-length. The conversion ratio corresponding to this profile achieves 1.7 for $\xi_k = 6$ and $\gamma_0 = 1.6$.

The conversion ratio is maximal for a certain optimal form of the function $\chi(z)$. Assume that, when the pulse propagates from the collector to the cathode region, the signal shape and amplitude for the synchronous harmonic are constant, while the pulse peak power linearly increases at the greater portion of interaction length. One can readily show that, in the limiting case, these requirements are satisfied by the function $\chi(z) \propto (1 - z/L_a)^{-1/2}$, where L_a is slightly greater than L. This case is of interest to future studies and corresponds to solitonlike solutions for $K \gg 1$.

In the practical implementation of the Cherenkov SR, the effects associated with the dispersion of electromagnetic pulse (not taken into account in the model) may be important. In the active interaction phase, the generated pulse propagates counter to the electron motion, whereupon it is reflected from the cathode area and is led through the same corrugated waveguide to the collector. During each phase, the wave packet can spread because of the dispersion $V_g(\omega) = d\omega/dh$ of group velocity in the pulse spectral range. Figure 3 shows the dispersion characteristic of a lowest type (E_{01}) symmetric wave in a corrugated waveguide that was used in the experiment. Estimates show that this effect could be significant in some early works, where a portion of an evanescent waveguide (with a reduced radius) was used as a reflector, while the mean radius of the corrugated waveguide was only slightly different from the critical value. For this reason, the bandwidth $(1 - \omega_{min}/\omega_{max})$ of the retarding system, which was limited from above by blocking near the Bragg resonance, was equal to 25–35%. To reduce the dispersive spreading, a corrugated waveguide with an increased (almost twice) mean radius was used in this work. A low-finesse band reflector was used [17]. In parallel to the passband broadening, which, as seen from Fig. 3, achieves ~50%, the packet group velocity increases approximately twofold. As known, for the Gaussian pulse envelope, the scale, on which the pulse broadens by a factor of $\sqrt{2}$, is proportional to V_g^3. According to the estimates and simulation with the "KARAT" program, the dispersive spreading was small in our experiment.

Apart from the dispersion of group velocity, such factors as the particle interaction with nonsynchronous waves and the field of beam space charge may reduce the conversion coefficient in real conditions. All these factors were also taken into account in the large-particle numerical simulation (KARAT program). After detailed computations, which gave $K \approx 1.4$ for the conversion ratio, the geometry of the system was carried to the experiment. The maximal accelerating voltage in a coaxial vacuum diode tube of a compact electron accelerator SINUS-150 [15] was equal to 330 kV, with a pulse duration of 4 ns (Fig. 4). The beam current was as high as 2.6 kA. Thus, the maximal electron-beam

power was estimated at 0.9 GW with an accuracy of ±10%. The range of controlled voltage was 230–330 kV, which corresponded to currents from 1.6 to 2.6 kA. A tubular electron beam with an o.d. of 34.5 mm was transported in a uniform magnetic field of 24 kOe along a periodic decelerating system with a mean radius of 20 mm, a period of 13.1 mm, a length of 22*d*, and a maximal corrugation amplitude of 2.3 mm.

Signals were recorded by a TDS694C digital oscilloscope with an analog band of 3 GHz. With allowance for the nonlinear volt–watt characteristic of the detector, the microwave pulse duration reproduced by the program was equal to 0.5 ns at a 3 dB level for the maximal cathode voltage. The pulse energy measured by a calorimeter was as high as 0.6 J, which allowed the peak power to be estimated at 1.2 GW with an accuracy no worse than ±12%. The experimental data on the pulse shape, its duration, and a value of 1.4 ± 0.3 obtained for the maximal conversion ratio (for a cathode voltage of 300 kV) were in compliance with the simulation results. The SR-pulse spectrum, as measured by the heterodyne method followed by the Fourier analysis, had a width from 7 to 15% at a 3 dB level, in accordance with the natural width of the recorded microwave signals.

Thus, the possibility of realizing SR regimes with a pulse peak power exceeding the electron flow power has been proved theoretically and experimentally for the conditions of Cherenkov interaction between a rectilinear particle flow and a synchronous harmonic of a counterpropagating wave. Theoretical analysis shows that the SR-pulse peak power can be further increased in the inhomogeneous decelerating systems with special longitudinal profile of the coupling coefficient between electrons and synchronous spatial harmonic.

REFERENCES

1. V. V. Zheleznyakov, V. V. Kocharovskiĭ, and Vl. V. Kocharovskiĭ, Izv. Vyssh. Uchebn. Zaved., Radiofiz. **29**, 1095 (1986).
2. N. S. Ginzburg and A. S. Sergeev, Zh. Éksp. Teor. Fiz. **99**, 438 (1991) [Sov. Phys. JETP **72**, 243 (1991)].
3. N. S. Ginzburg, I. V. Zotova, and A. S. Sergeev, Pis'ma Zh. Éksp. Teor. Fiz. **60**, 501 (1994) [JETP Lett. **60**, 513 (1994)].
4. L. A. Vaĭnshteĭn and A. I. Kleev, Dokl. Akad. Nauk SSSR **301**, 862 (1990) [Sov. Phys. Dokl. **35**, 359 (1990)].
5. R. Bonifacio, N. Piovella, and B. W. J. McNeil, Phys. Rev. A **44**, 3441 (1991).
6. N. S. Ginzburg, I. V. Zotova, A. S. Sergeev, *et al.*, Pis'ma Zh. Éksp. Teor. Fiz. **63**, 322 (1996) [JETP Lett. **63**, 331 (1996)].
7. N. S. Ginzburg, I. V. Zotova, A. S. Sergeev, *et al.*, Phys. Rev. Lett. **78**, 2365 (1997).
8. V. G. Shpak, M. I. Yalandin, N. S. Ginzburg, *et al.*, Dokl. Akad. Nauk **365**, 50 (1999) [Dokl. Phys. **44**, 143 (1999)].
9. S. D. Korovin, G. A. Mesyats, V. V. Rostov, *et al.*, Pis'ma Zh. Tekh. Fiz. **28** (1), 81 (2002) [Tech. Phys. Lett. **28**, 76 (2002)].
10. R. H. Dicke, Phys. Rev. **93**, 99 (1954).
11. V. V. Zheleznyakov, V. V. Kocharovskiĭ, and Vl. V. Kocharovskiĭ, Usp. Fiz. Nauk **159**, 193 (1989) [Sov. Phys. Usp. **32**, 835 (1989)].
12. N. Skribanowitz, I. P. Herman, J. C. McGillivray, *et al.*, Phys. Rev. Lett. **30**, 309 (1973).
13. L. A. Vaĭnshteĭn and V. A. Solntsev, *Lectures on Microwave Electronics* (Sovetskoe Radio, Moscow, 1973).
14. N. S. Ginzburg, S. P. Kuznetsov, and T. N. Fedoseeva, Izv. Vyssh. Uchebn. Zaved., Radiofiz. **21**, 1037 (1978).
15. V. P. Gubanov, S. D. Korovin, I. V. Pegel, *et al.*, IEEE Trans. Plasma Sci. **25**, 258 (1997).
16. V. V. Rostov and E. M. Tot'meninov, Izv. Vyssh. Uchebn. Zaved., Radiofiz. **44**, 325 (2001).
17. S. D. Korovin, I. K. Kurkan, V. V. Rostov, and E. M. Tot'meninov, Izv. Vyssh. Uchebn. Zaved., Radiofiz. **42**, 1189 (1999).

Translated by V. Sakun

JETP Letters, Vol. 77, No. 6, 2003, pp. 270–275. Translated from Pis'ma v Zhurnal Éksperimental'noĭ i Teoreticheskoĭ Fiziki, Vol. 77, No. 6, 2003, pp. 319–325.

Beyond the Kuramoto–Zel'dovich Theory: Steadily Rotating Concave Spiral Waves and Their Relation to the Echo Phenomenon

O. A. Mornev[1, *], I. M. Tsyganov[2], O. V. Aslanidi[3, 4], and M. A. Tsyganov[1]

[1] *Institute of Theoretical and Experimental Biophysics, Russian Academy of Sciences, pr. Nauki, Pushchino, Moscow region, 142292 Russia*

* *e-mail: mornev@mail.ru*

[2] *Moscow State University, Vorob'evy gory, Moscow, 119899 Russia*

[3] *Institute of Cell Biophysics, Russian Academy of Sciences, Pushchino, Moscow region, 142292 Russia*

[4] *School of Biomedical Sciences, University of Leeds, Leeds LS2 9JT, United Kingdom*

Received November 27, 2002; in final form, February 12, 2003

In numerical experiments with the Fitzhugh–Nagumo set of reaction-diffusion equations describing two-dimensional excitable media, unusual solutions are found that correspond to a concave spiral wave steadily rotating round a circular obstacle in a finite-size medium. Such a wave arises in the region of parameters corresponding to the solitonlike regime (see text); it appears due to the interaction between the peripheral areas of a "seed" spiral wave with a convex front and the echo waves incoming from the outer boundaries of a medium. The solutions obtained are in contradiction with intuition and represent a numerical counterexample to the known theories that forbid steadily moving excitation waves with concave fronts. Nevertheless, a concave spiral wave is a stable object; being transformed to the usual spiral wave with a convex front by suppressing echo at the outer boundaries of the medium, it is again recovered upon restoring the echo conditions. In addition to the single-arm spiral concave wave, solutions are obtained that describe multiarm waves of this type; for this reason, the concave fronts of these waves are a coarse property. © *2003 MAIK "Nauka/Interperiodica"*.

PACS numbers: 82.40.Bj; 82.40.Ck

It is often believed that distributed autocatalytic reaction-diffusion systems (excitable media) are incapable of sustaining stable motion of excitation waves (autowaves) with a leading front concave toward the wave propagation direction. The argumentation of this opinion is based, in particular, on the theoretical works of Zel'dovich [1], where it was shown that the flat front of a flame propagating in a spatially homogeneous combustible medium with moderately large Reynolds numbers is stable to bending perturbations. The physical explanation of the stability is that medium is fired ahead of the concave (convex) front areas faster (slower) than ahead of the flat front because of the focusing (scattering) of heat flow propagating from the front along the orthogonal trajectories in the direction of decreasing temperature gradient. As a result, the motion of the front concave areas is accelerated, while the motion of convex areas is decelerated, and the front flattens.

Note that the kinetic mechanism for sustaining the propagation of combustion autowave, namely, the activator (heat) diffusion in the direction of wave motion and the triggering of autocatalytic processes ahead of the front, to provide its propagation, is quite universal. In particular, this mechanism underlies biologically important phenomena such as the transfer of nerve impulses in the nervous system and the propagation of electrochemical excitation autowaves to the heart [2–5]. The fact that not heat but the alkali metal ions are the diffusing activators in biologically excitable media (BEM) does not change anything; for this reason, when appealing to the qualitative argumentation such as that presented above with a slightly modified terminology, one usually arrives at the conclusion that a stable propagating concave wave cannot exist in the BEM.

This assumption is also supported by the theory of autowave bending stability [6], which was developed by Kuramoto for multicomponent excitable media containing the autocatalysis activators and inhibitors and described by the reaction-diffusion equations

$$\partial_t \mathbf{X} = D\Delta\mathbf{X} + \mathbf{F}(\mathbf{X}). \quad (1)$$

Here, $\partial_t \equiv \partial/\partial t$; t is time; Δ is the Laplacian acting on the spatial coordinates; $\mathbf{X} \equiv \{X_1, \ldots, X_n\}$ is the vector of component concentrations; $\mathbf{F}(\mathbf{X}) \equiv \{F_1(\mathbf{X}), \ldots, F_n(\mathbf{X})\}$ is the vector of kinetic functions that determine the component production rate in unit volume; n is the number of components; and $D \equiv \mathrm{diag}\{D_1, \ldots D_n\}$ ($D_1 > 0, \ldots, D_n > 0$) is the diagonal matrix of component diffusivities. In the Kuramoto theory, the local normal velocity v_n of a bent autowave wave front is related to

its local curvature K and velocity v_0 of the flat front by the expression

$$v_n = v_0 - \beta K, \quad (2)$$

where β is a constant that depends on the activator and inhibitor diffusivities (for flames, Eq. (2) was obtained independently by Zel'dovich in [1]). If a multicomponent medium contains only a single diffusing component (activator), while the inhibitors do not diffuse, then, as follows from the Kuramoto formalism, the constant β in Eq. (2) is positive. This situation corresponds to the BEM; the known Hodgkin–Huxley nerve-conduction equations and their analogues describing the excitable heart medium have the form of Eqs. (1) with the matrix $D = \mathrm{diag}\{D_1, 0, \ldots, 0\}$. However, for positive β, the velocity v_n in Eq. (2) satisfies the inequalities $v_n > v_0$ for $K < 0$ (concave front) and $v_n < v_0$ for $K > 0$ (convex front). Because of this, the bent autowaves should flatten with time.

The latter conclusion does not contradict the existence of the known spiral waves that usually have convex front upon the steady rotation in the spatially homogeneous excitable media [7–9]; when explaining the convex geometry of spiral waves [10–13], the modern theory uses Eq. (2) with $\beta > 0$ as one of the key postulates. As to the spiral waves with the stable concave leading front, their possible existence in the BEM is usually not disputed.

Recently, the first numerical examples against this opinion have been presented to demonstrate that concave spiral waves can be realized in the BEM [14, 15]. Later on, such waves were detected in the experiments on a multicomponent chemical excitable medium showing the Belousov–Zhabotinsky oscillation reaction [16] (contrary to BEM, inhibitors in this medium diffuse). These results raise the question of the physical mechanism that sustains the concave spiral waves. Below, numerical experiments aimed at revealing this mechanism are presented.

The experiments were carried out using the well-known Fitzhugh–Nagumo set of second-order reaction-diffusion equations that are used in biophysics for modeling the phenomena in BEM [2, 5]. A modification [17] of this system was used, which, when adapted to the description of a two-dimensional BEM and written in the dimensionless variables, takes the form

$$\partial_t V = (\partial_x^2 + \partial_x^2)V - kV(V - V_{\mathrm{th}})(V - 1) - I; \quad (3a)$$

$$\partial_t I = (\sigma V - I)/\tau(V, \Delta\varepsilon); \quad (3b)$$

$$\tau(V; \Delta\varepsilon) \quad (3c)$$

$$= \left[0.05 + \Delta = \varepsilon\left(2 - \tanh\frac{V + 0.04}{0.01} + \tanh\frac{V - 0.75}{0.1}\right)\right]^{-1}$$

(here, $\partial_x^2 \equiv \partial^2/\partial x^2$; $\partial_y^2 \equiv \partial^2/\partial y^2$; x and y are the spatial coordinates; and the physical meaning of the remaining variables and parameters is given in [17]).

The set of Eqs. (3) belongs to the reaction-diffusion Eqs. (1) and, being characterized by the diffusivity matrix $D = \mathrm{diag}\{1, 0\}$, describes a homogeneous two-component excitable medium with diffusing activator (variable V) and immobile inhibitor (variable I). From the above considerations, the traditional intuition refuses the possibility of the existence of steadily rotating concave spiral waves in this medium. However, such waves were observed by us in the numerical experiments described below. It turned out that concave spiral waves appear if the parameters correspond to the solitonlike regime. Contrary to the ordinary annihilation regime, the solitonlike regime in the BEM is characterized not by the quenching but by the reflection of autowaves colliding with each other and/or with impermeable medium boundaries (echo) [15, 17–19].[1] The data presented below allow one to conclude that the echo waves incoming from the outer boundaries of the medium sustain the existence of concave spiral waves.

Calculations were carried out for a medium of size $L_x \times L_y$, $L_x = L_y = 50$ using the Euler method; the integration steps hx, hy, and ht with respect to the variables x, y, and t were $hx = hy = 0.5$ and $ht = 0.005$ (the controlled $hx = hy = 0.125$ and $ht = 0.0003$). Two types of boundary conditions were used alternately for different boundary areas (the details will be clarified below): the Neumann conditions $\partial_n V = 0$ that describe the impermeability of the respective boundary area to the activator diffusion flux ($\partial_n \equiv \partial/\partial n$ symbolizes the derivative along the normal to the boundary) and the zero Dirichlet conditions $V = 0$. The parameters in Eq. (3) were established for $k = 8$, $V_{\mathrm{th}} = 0.12$, $\sigma = 4$, and $\Delta\varepsilon = 0.62$ corresponding to the solitonlike regime [17].

Recall the physical mechanism of echo phenomenon in the BEM with the solitonlike regime. Calculations show that the plane autowave in this regime is a doublet composed of a high-amplitude nonlinear leading pulse and a low-amplitude "near-linear" below-threshold satellite wave (Figs. 1a, 1b). Upon the collision of two counterpropagating doublets, the leaders annihilate, while the satellites are summed up and, by locally changing the variable V to the above-threshold value, initiate a pair of diverging doublet echo waves (Figs. 1c, 1d). However, the echo waves are not always generated upon the collision of the doublets with boundaries; the Neumann impermeability conditions correspond to the reflection from the boundaries (Fig. 1c), while the Dirichlet zero conditions suppress

[1] We refused the term "soliton regime" that was used in our early works in favor of the more careful synonym "solitonlike regime." In these terms, there is an allusion to the well-known soliton property of escaping from the interactions without destruction in conservative systems. However, the analogy with solitons is superficial, because the physical nature of the latter is basically different from the physics of autowaves.

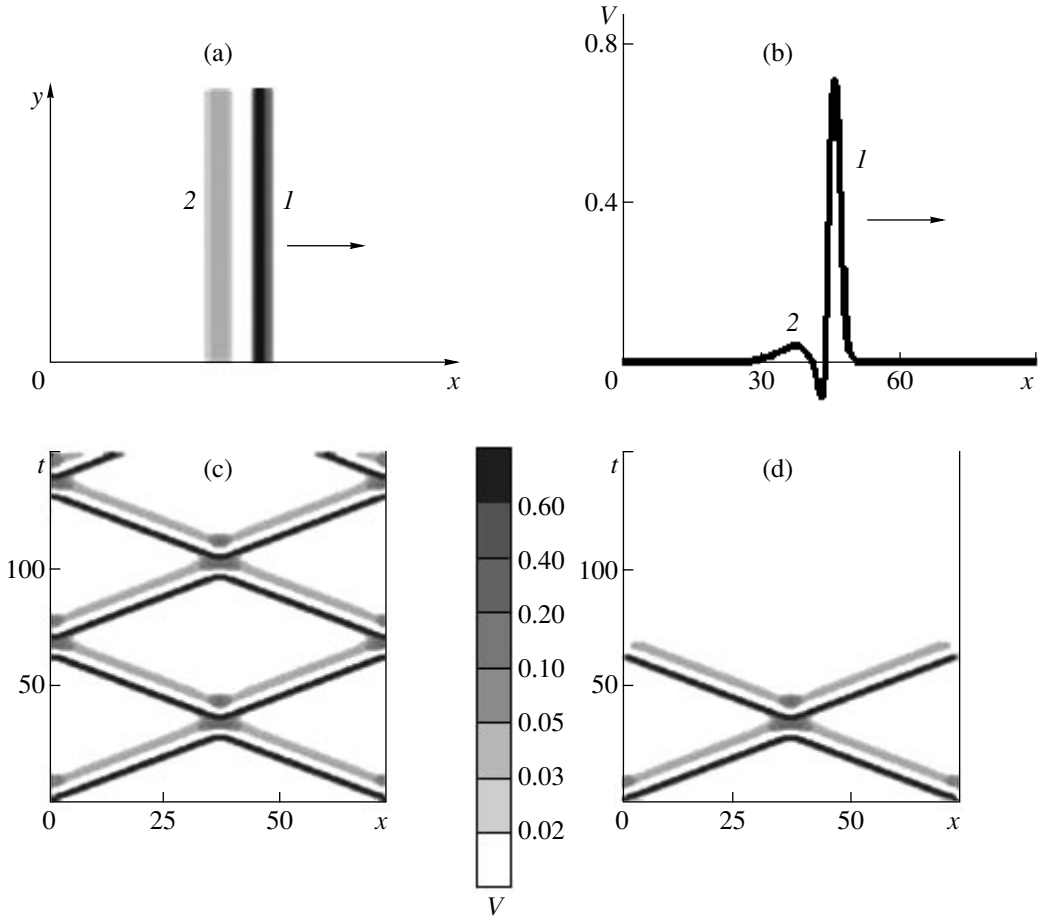

Fig. 1. Solitonlike regime in a two-dimensional excitable medium described by the set of Eqs. (3). (a) Doublet structure of a plane autowave (*1* leader and *2* satellite; the autowave moves from left to right); (b) spatial profile of the doublet along the *x* axis; (c) and (d) spatiotemporal interaction diagrams for plane autowaves moving along *x* and colliding with each other and with medium boundaries under the (c) impermeability conditions or (d) Dirichlet zero conditions. Charts in (a), (c), and (d) and in the subsequent figures reflect the distribution of the activation variable *V*. The correspondence between colors and *V* is shown in the palette.

reflection without affecting the doublet capability of being reflected in the mutual collisions in medium bulk (Fig. 1d).[2]

The latter fact was used in our numerical experiments with spiral waves rotated round a circular obstacle in the middle of computational mesh, set by the software tools. The experimental results are as follows.

1. In the solitonlike regime, if the boundary conditions at the outer boundary of the medium and the obstacle boundary are of the Neumann impermeability type, the set of Eqs. (3) has a solution in the form of steadily rotating concave spiral wave (Fig. 2). The formation of a spiral wave is initiated by a plane autowave, which initially moves along a finite medium region determined by the impermeable barrier (Fig. 2, $t = 10$).[3] After the plane autowave penetrates into the medium, the barrier is eliminated, and a seed doublet spiral wave with the convex leading front appears in the medium. This wave is captured by the circular obstacle with radius $\rho = 4$ in the middle of the medium (Fig. 2, $t = 30$) and starts to rotate clockwise. The collisions of peripheral areas of spiral satellite with the impermeable boundaries are accompanied by the appearance of echo waves. The latter, when penetrating into the medium and re-reflecting upon collisions, destroy the regular dynamic picture (Fig. 2, $t = 50$–400). With time, this irregular regime is surprisingly rearranged into a spiral (not doublet!) wave with a concave front, which rotates round the obstacle clockwise (Fig. 2, $t = 800$–806)

[2] From the symmetry considerations, the echo-wave generation in the doublet collision with the impermeable boundary can be regarded as the result of summing up the satellite and its virtual "mirror twin" moving counter the wave out from this boundary. For the Dirichlet zero boundary conditions, the doublet decays upon the collision with boundary without reflection because *V* becomes zero.

[3] The barrier shown in Fig. 2 for $t = 10$ by a thin vertical section is established by the program. The plane autowave is initiated by specifying the following initial ($t = 0$) conditions: $V = 0.5$ at the stripe $0 \le y \le 2$ between the left boundary of the medium and the barrier; $V = 0$ at other points; $I = 0$ everywhere. Hereafter, the origin of *x*, *y* coordinates is in the left bottom corner of the medium.

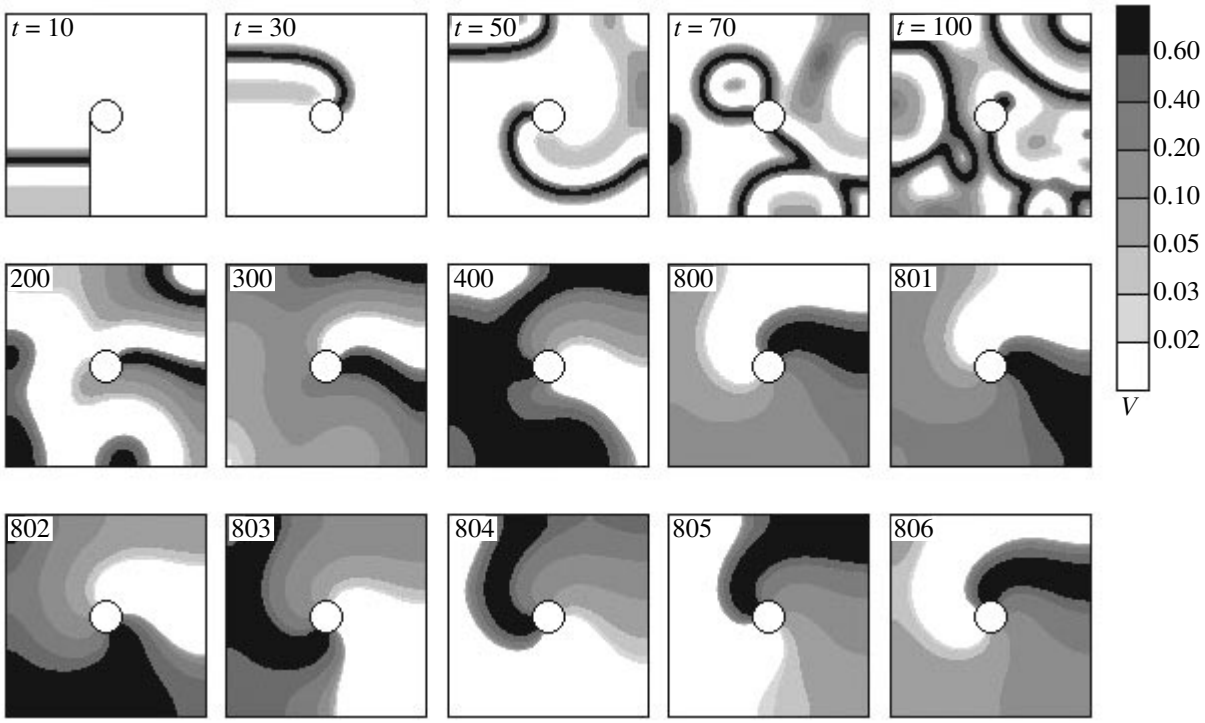

Fig. 2. Formation dynamics of a concave spiral wave rotating about circular obstacle in the solitonlike regime (see text).

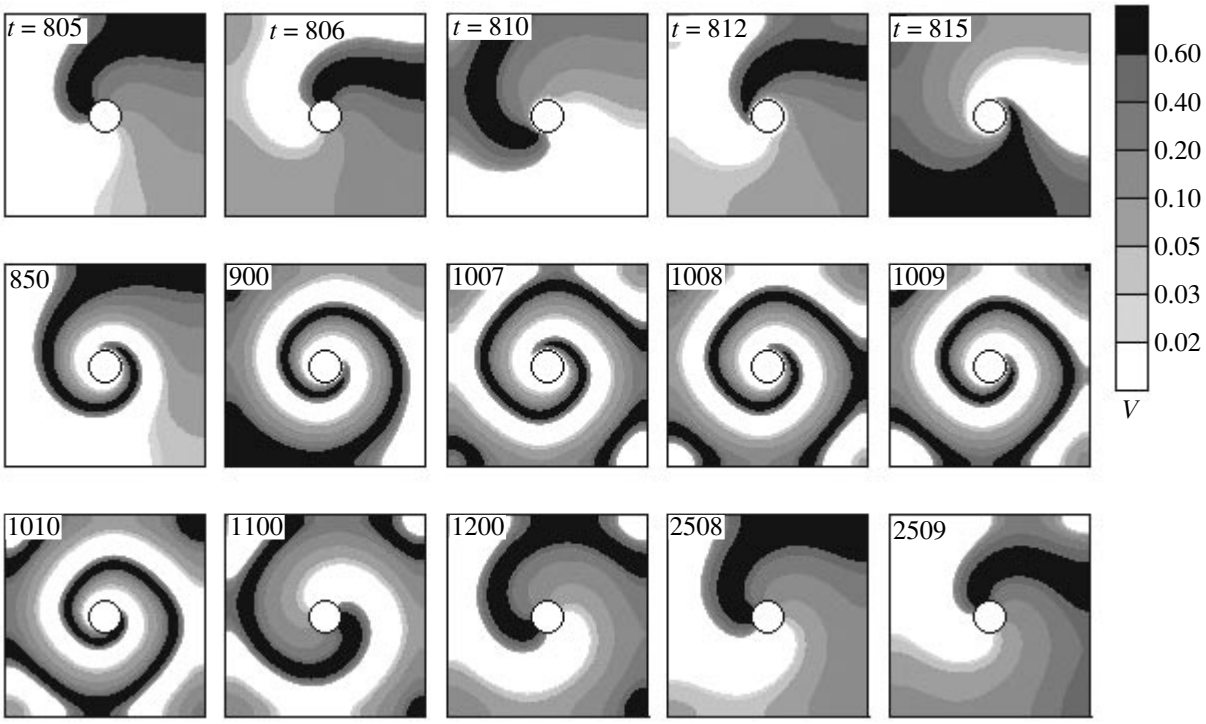

Fig. 3. The figure demonstrating that the mechanism sustaining the concavity of spiral wave is independent of the conditions at the boundary of circular obstacle.

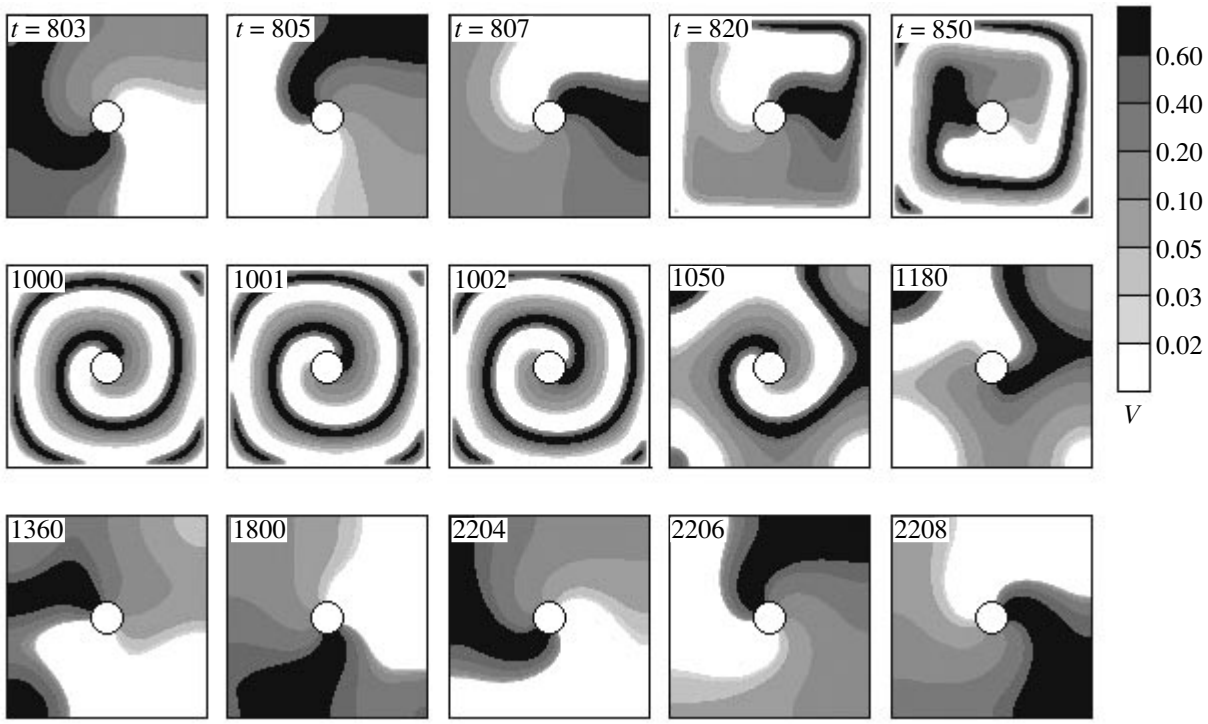

Fig. 4. The connection between the mechanism sustaining the concavity of spiral wave and the conditions at the outer boundary of the medium. The same as in Fig. 3, but the change from the impermeability conditions to the Dirichlet zero conditions occurs at the outer boundary of the medium rather than at the obstacle boundary.

retaining its characteristics during thousand revolutions (during all computational time).

2. The dynamic mechanism sustaining the stable front concavity of the spiral wave is not associated with the ability of a local obstacle, around which the wave circulates, to produce echo waves. This conclusion is confirmed by the following observation. If the impermeability conditions occur at the outer boundary, while they are replaced by the echo-suppressing Dirichlet zero conditions at the obstacle boundaries, the spiral wave remains concave (Fig. 3). In this case, the concave spiral clockwise-rotating wave (t = 805, 806) is formed as in Fig. 2. At t = 809 (not shown), the impermeability conditions at the obstacle boundary are changed to the Dirichlet zero conditions. As a result, the parameters of spiral wave change, but the front retains its concave shape (t = 810–1009). After the impermeability conditions are restored at the obstacle boundary, the spiral-wave parameters evolve to their initial values (t = 1010–2509). If the Dirichlet zero conditions are established for the outer boundary from the beginning of the experiment (t = 0), the seed spiral doublet shown in Fig. 2 rotates around the obstacle without producing echo waves and with retaining the convex shape.

3. The concave front shape of the spiral wave is due to the ability of the outer medium boundary to sustain the echo-wave generation (Fig. 4); if the impermeability condition at the outer boundary is changed at t = 809 to the Dirichlet zero conditions, the concave spiral wave transforms to the convex spiral wave (t = 820–1002). This transformation is reversible: after the impermeability conditions are returned to the outer boundary at t = 1010, the front again becomes concave (t = 1050–2208).

4. In the solitonlike regime, the front concavity of spiral wave is a coarse property in the sense that it is inherent not only in single-arm but also in multiarm spiral waves. This is illustrated in Fig. 5 by the formation dynamics of a concave three-arm spiral wave. The radius of circular obstacle is $\rho = 5$; the impermeability conditions are kept at the obstacle and outer boundaries. The spiral wave is initiated by three plane autowaves, as in Fig. 2. As in the case of a single-arm wave, a wave with three concave arms is formed through the stage of irregular regime resulting from the re-reflection of echo waves coming from the outer boundaries.

From the viewpoint of intuition based on the results of Zel'dovich and Kuramoto, the positions formulated in items 1–4 are paradoxical. They are seemingly unusual also for the kinematic theory of spiral waves, according to which the structure of a spiral wave is determined by the local situation in the vicinity of its core and not by the peripheral events ([11], chapter 1, section 8). This, however, signifies that the traditional intuition needs reorganization using a refined but as yet undeveloped theory.

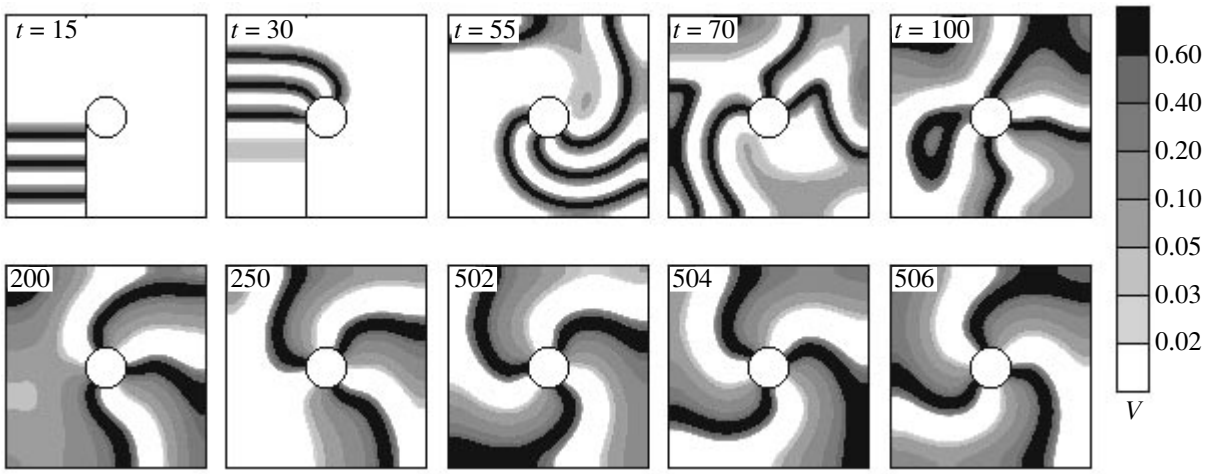

Fig. 5. Formation dynamics of a concave three-arm spiral wave.

P.S. When the manuscript had already been written, we received the reprints of article [20], where the analytic solutions were obtained for the main equation of kinematic theory of concave spiral waves. However, their relevance to the effects considered in this work is unclear, because the modern kinematic theory does not describe the solitonlike regime. We are grateful to Yu. E. El'kin and V.N. Biktashev for these reprints.

This work was supported by the Russian Foundation for Basic Research, project nos. 99-01-00956 and 02-01-00626.

REFERENCES

1. Ya. B. Zel'dovich, Preprint, IFKh AN SSSR (Inst. of Chemical Physics in Chernogolovka, USSR Academy of Sciences, 1979); Combust. Flame **40**, 225 (1981); in *Nonlinear Waves: Propagation and Interaction*, Ed. by A. V. Gaponov-Grekhov (Nauka, Moscow, 1981), pp. 30–41.
2. A. C. Scott, Rev. Mod. Phys. **47**, 487 (1975).
3. V. S. Markin, V. F. Pastushenko, and Yu. L. Chizmadzhev, Usp. Fiz. Nauk **123**, 289 (1977) [Sov. Phys. Usp. **20**, 836 (1977)].
4. V. A. Vasil'ev, Yu. M. Romanovskiĭ, and V. G. Yakhno, Usp. Fiz. Nauk **128**, 625 (1979) [Sov. Phys. Usp. **22**, 615 (1979)].
5. A. C. Scott, *Nonlinear Science: Emergence and Dynamics of Coherent Structures* (Oxford Univ. Press, Oxford, 1999); *Neuroscience: A Mathematical Primer* (Springer, New York, 2002).
6. Y. Kuramoto, Prog. Theor. Phys. **63**, 1885 (1980); *Dynamics of Synergetic Systems* (Springer, Berlin, 1980), p. 134.
7. N. Wiener and A. Rosenblueth, Arch. Inst. Cardiol. Mex. **16**, 205 (1946).
8. I. S. Balakhovskiĭ, Biofizika **10**, 1063 (1965).
9. A. M. Zhabotinskiĭ and A. N. Zaikin, *Oscillation Processes in Biological and Chemical Systems* (Pushchinsk. Nauchn. Tsentr, Pushchino, 1971), Vol. 2, p. 279.
10. V. A. Davydov, V. S. Zykov, A. S. Mikhaĭlov, and P. K. Brazhnik, Izv. Vyssh. Uchebn. Zaved., Radiofiz. **31**, 574 (1988).
11. A. Yu. Loskutov and A. S. Mikhaĭlov, *Introduction to Synergetics* (Nauka, Moscow, 1990).
12. V. A. Davydov, V. S. Zykov, and A. S. Mikhaĭlov, Usp. Fiz. Nauk **161** (8), 45 (1991) [Sov. Phys. Usp. **34**, 665 (1991)].
13. A. S. Mikhailov, V. A. Davydov, and V. S. Zykov, Physica D (Amsterdam) **70**, 1 (1994).
14. O. A. Mornev, O. V. Aslanidi, and L. M. Chaĭlakhyan, Dokl. Akad. Nauk **353**, 682 (1997).
15. O. A. Mornev, O. V. Aslanidi, and I. M. Tsyganov, Macromol. Symp. **160**, 115 (2000).
16. V. K. Vanag and I. R. Epstein, Science **294**, 835 (2001).
17. O. A. Mornev, O. V. Aslanidi, R. R. Aliev, and L. M. Chaĭlakhyan, Dokl. Akad. Nauk **347**, 123 (1996).
18. O. V. Aslanidi and O. A. Mornev, Pis'ma Zh. Éksp. Teor. Fiz. **65**, 553 (1997) [JETP Lett. **65**, 579 (1997)]; Mat. Model. **11**, 3 (1999).
19. O. V. Aslanidi and O. A. Mornev, J. Biol. Phys. **25**, 149 (1999).
20. Yu. E. Elkin, V. N. Biktashev, and A. V. Holden, Chaos, Solitons and Fractals **14**, 385 (2002).

Translated by V. Sakun

JETP Letters, Vol. 77, No. 6, 2003, pp. 276–279. From Pis'ma v Zhurnal Éksperimental'noĭ i Teoreticheskoĭ Fiziki, Vol. 77, No. 6, 2003, pp. 326–329.

Acoustic Impact on Superluminescence in Argon Plasma¶

A. R. Aramyan

Institute of Applied Problems of Physics NAS RA, 375014 Yerevan, Republic of Armenia

e-mail: aramyan@web.am

Received December 19, 2002; in final form, February 14, 2003

It is shown that in an argon discharge plasma it is possible to obtain the overpopulation of certain electronic levels of atomic argon under the influence of acoustic waves. When the specified threshold is passed, superluminescence (in the form of light flashes) from the overpopulated electronic levels of atomic argon is observed.
© *2003 MAIK "Nauka/Interperiodica".*

PACS numbers: 52.25.Os; 43.35.Lq; 32.50.+d

The investigation of the properties of low-temperature ionized plasma and of different influences on it is always urgent, since, besides the elucidation of new physical mechanisms, the results of these investigations find immediate practical applications. It is noteworthy, however, that work on the influence of acoustic waves on plasma parameters and on processes in the plasma environment is relatively scarce. In addition, the problem of acoustic wave interactions with a thermodynamically nonequilibrium gas, such as the partially ionized gas-discharge plasma, where the electron temperature usually far exceeds that of heavier particles [1–3], has lately been of high interest. Note that of numerous problems connected with interactions of acoustic waves with partially ionized plasma, the study of the influence of acoustic waves on radiation spectra of gas-discharge plasma appears to be especially promising. In recent years, an interesting effect of an abrupt change of the radiation spectrum under the action of sound waves in a dense ($p \sim 100$ Torr) argon discharge plasma was observed in our laboratory [4, 5]. Several seconds after cutting off the sound wave, light flashes were observed over several minutes at different points of the discharge tube in the bulk of the positive column, which apparently corresponded to some transitions between electronic levels of atomic argon. An assumption was made about the autogeneration (single-pass generation) of appropriate lines in the argon spectrum (the colored photo of this effect is given in [5]).

It was shown as a result of further research of this effect that, under certain conditions, the change in the plasma radiation at the interaction of acoustic waves with plasma shows up not only as flashes but also as a substantial amplification of some spectral lines. Contrary to [4, 5], in the present work the correspondence of the observed spectral lines to transitions between electronic levels of atomic argon was specified.

The studies of the change of a radiation spectrum under the influence of acoustic waves were conducted in low-temperature argon discharge plasma (pressure 100 Torr, discharge current 50mA, voltage on electrodes 2 kV). The experimental setup (Fig. 1) includes a quartz discharge tube with an internal diameter of 6 cm and a length of 100 cm. The distance between the electrodes was 85 cm. An electrodynamic transmitter is attached to one of the butt ends of the tube. Beforehand, the power from the electrodynamic transmitter was calibrated with a ROBOTRON 01012 sound level meter for conditions existing in the discharge tube. The light emitted from plasma passes through the second butt and is directed to a monochromator. The investigation of intensity variations of some lines of plasma radiation spectra is curried out under the action of acoustic waves.

The dependence of the radiation intensity of the $6s \longrightarrow 4p$ transition on the acoustic wave intensity at 190 Hz frequency is given in Fig. 2 and is seen to show hysteresis behavior. When the intensity of acoustic waves increases (from zero) to $A_{\max}$ (corresponding to 90 dB), no changes in the radiation spectrum are observed, and for these acoustic wave intensities a decontraction of plasma takes place and completely fills the tube volume. On the return path of acoustic wave intensity, a notable increase in line radiation

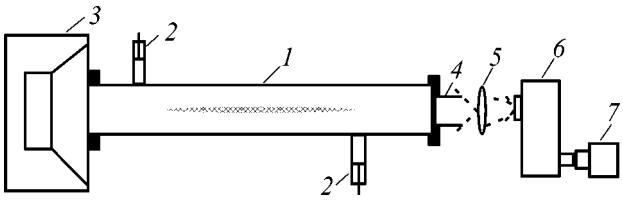

Fig. 1. The experimental setup: *1* is the discharge tube; *2* is the electrodes; *3* is the electrodynamic transmitter of sonic waves; *4* is the window; *5* is the lens; *6* is the monochromator; *7* is the photoelectric multiplier tube.

¶ This article was submitted by the author in English.

intensity is observed at the value A_c. The critical value A_c (82 dB) corresponds to the unpinching threshold of discharge. The line intensity is observed to increase after the pinching of discharge. The further reduction of acoustic wave intensity is accompanied by a smooth decrease of the line intensity.

To find the relation between the constant increase of spectral line intensity and flashes, we have plotted the dependences to be discussed below. The reduction in acoustic wave intensity on the return path A stays at the value A_o, which is less than A_c and corresponds to 80 dB (Fig. 2). In Fig. 3a, the time dependence of the radiation intensity of $6s \longrightarrow 4p$ transition under constant influence of resonant acoustic waves with 190 Hz frequency and intensity A_0 is shown. It is seen that, in the absence of flashes, the intensity of line radiation has the constant value I_o. At the bursting of flashes, the line intensity sharply increases (by nearly 100 times) up to I_{max}. After the bursting (with duration of 15–20 ms), the intensity drops to a minimum, I_{min}, which corresponds to the value of radiation intensity in the absence of acoustic waves. The rise of intensity from I_{min} to I_o is rather long, ~1s. Shown in the second plot (Fig. 3b) is the dependence of radiation intensity of an analogous transition after cutting out acoustic waves, the initial frequency of which was 190 Hz and intensity 90 dB. After cutting out of acoustic waves, the line intensity stays at the minimum initial value of I_{min} for several seconds (~2s). The value of I_o is reached in a time period, and then I_o smoothly decreases to I_{min} in 15–20 s. The pattern of light flashes in this regime is similar to the previous one (Fig. 3a).

Thus, summarizing the above experimental data one can draw a qualitative conclusion about the mechanism of this effect.

It is obvious that low frequency phonons cannot influence transitions between electronic levels and processes of radiation. It is possible to say that we are dealing with hydrodynamics, i.e., hydrodynamic flows, which can influence stability and configuration of a plasma cloud and, through them, processes of ionization and recombination. As is known [6–8], in the presence of inhomogeneity of the acoustic field, there arise vortex-type acoustic flows in the standing sound wave. The velocity of these flows has an order-of-magnitude value $U \sim u_a^2/C$ (u_a is the vibration velocity, C is the sound velocity). In the discharge tube the inhomogeneous acoustic field is formed, first of all, due to the existence of a strong temperature gradient along the tube radius, and secondly, of a boundary layer near the walls, where the velocity of motion is reduced from its value in the sound wave to zero. The calculations show [7] that the intensity of acoustic flow due to the temperature gradient essentially exceeds that due to the boundary layer. It was shown that a sufficiently intense standing acoustic wave may produce vortex-type acoustic flows, the contribution of which to the process

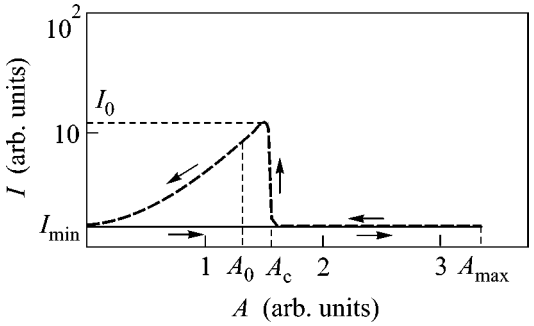

Fig. 2. Dependence of the radiation intensity of $6s \longrightarrow 4p$ transition on the acoustic wave intensity at 190 Hz.

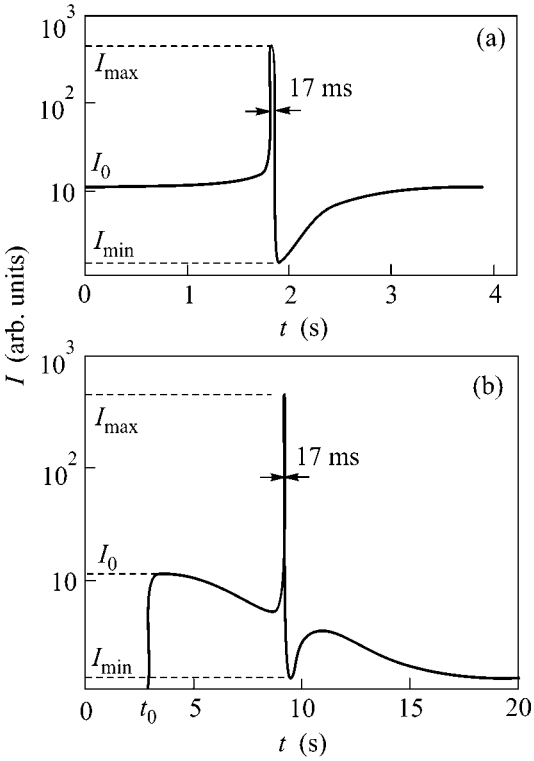

Fig. 3. The time dependence of radiation intensity of $6s \longrightarrow 4p$ transition: (a) under constant action of resonant acoustic waves of frequency 190 Hz and intensity 80 dB, (b) after cutting out of acoustic waves, the initial frequency and intensity of which were 190 Hz and 90 dB.

of particle transfer in the radial direction may be substantial. That was also confirmed experimentally in [9], where a pinched discharge decontracted under the influence of high-intensity acoustic waves and the radial temperature gradient considerably smoothed out.

It is also known that at sufficiently high pressures ($P > 10$ mm Hg), virtually the only process of bulk neutralization of charged particles in the gas-discharge plasma, which is competitive with the diffusion process, is the dissociative recombination [10] of electrons

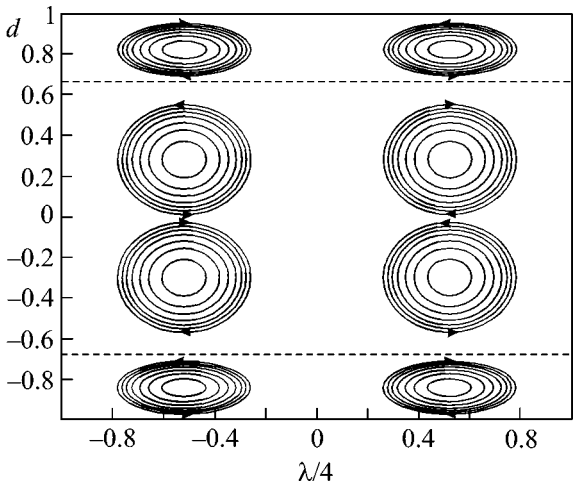

Fig. 4. The diagram of "acoustical flows" in the tube.

and molecular ions. In an inert gas discharge, the molecular ions are predominant at high pressures ($P >$ 10 mm Hg) and relatively low gas temperatures ($T <$ 1000 K). So, we may assume that our experiment proceeds via the following processes:

$$Ar^+ + 2Ar \longrightarrow Ar_2^+ + Ar, \quad Ar_2^+ + e \longrightarrow Ar^* + Ar.$$

These processes run at a very high rate and lead to efficient formation of excited atoms of inert gas. It is known that highly excited atoms are produced as a result of electron impact dissociation of molecules [11, 12]. This process was widely used in early investigations of Rydberg atoms.

High quantum levels of hydrogen atoms are known from the quantum theory to have large lifetimes. The average lifetime of t_n depends on the value of the first quantum number n as $t_n \sim n^4$.

So, taking into account the aforesaid, we may make the following assumptions: The flows formed (Fig. 4) are directed in some places to walls and in some places to the center of tube. These flows carry the particles in and out of the discharge range. In this process, the particles may be found in the regions of the discharge tube where the temperature of electrons and neutral particles are notably lower than in the discharge range. Hence, hot electrons are quickly cooled, mainly due to elastic electron–atom collisions. Then, recombination of electrons with ions takes place, basically with molecular ions. An analogous intense recombination occurs also in places, where the acoustic flows are directed to the center of tube. When and where the particles of cool gas get in the discharge, they cause an intense recombination. It turned out that, during these recombination events, i.e., during the dissociative recombinations, highly excited long-lived atoms were produced. So, in the indicated places, the accumulation of highly excited atoms occurs.

Now consider the destruction of such highly excited long-lived states of the atom as a result of collisions with atoms and molecules.

In conformity with the theory of atomic collisions [13], the probability of transition between two states strongly depends on the Messi parameter ξ (the probability is $\sim\exp(-\xi)$). Let us estimate the value of the Messi parameter for the transition $nl \longrightarrow n'l'$, where $n' = n - 1$. The difference in energy for this transition is $\Delta\varepsilon \sim (\delta_l - \delta_{l'})/n^3$, where δ_l is the quantum defect and n is the first quantum number. The Messi parameter is [14]

$$\xi = \Delta\varepsilon a/v_a \sim \delta_l/nv_a,$$

where a is the size of the strongly excited atom and v_a is the velocity of nucleus motion. For $n, l \gg 1$ the Messi parameter turns out to be small, due to the smallness of the quantum defect δ, and the probability of appropriate transitions is high. The situation is different when the highly excited states have orbital momentum $l \geq 0$. In these cases, the Messi parameter is $\xi \geq 1$ for moderate values of n. Then the probability of transition at the collision is much less than that in the former case.

Owing to the quenching of highly excited states at collisions with atoms and molecules, the levels with n, $l \geq 1$ are quickly emptied, whereas the levels with $n \gg 1$, $l \geq 0$ are occupied. In this experiment, the levels 7*s*, 6*s*, 7*d* are occupied. Due to this fact, an increase in radiation intensity from transitions $7s \longrightarrow 4p$, $6s \longrightarrow 4p$, $7d \longrightarrow 4p$ was observed. As for the flashes and locations of their formation, these are, presumably, due to the superluminescence that takes place when the overpopulation threshold for autogeneration is passed.

As was mentioned in the results, the blue flash of $7d \longrightarrow 4p$ arises only inside the discharge pinch and the orange one ($7s \longrightarrow 4p$, $6s \longrightarrow 4p$)—both inside and outside of the pinch boundaries. This is connected with the fact that, as a result of quenching at collisions, the 7*d* level may be depopulated. Since the concentration of charged particles inside the pinch is much greater than beyond the pinch boundary, one can assume that the recombination of charged particles inside the pinch (in consequence of acoustic flows) proceeds more intensely that beyond the radial boundary of pinch. For this reason, the concentration of highly excited atoms inside the pinch is much higher, with the result that the overpopulation threshold between levels $7d \longrightarrow 4p$ may be passed, to cause the superluminescence observed as blue flashes. As to the levels 7*s* and 6*s* (orange flashes), they are intensely populated inside and outside the pinch, but the probability of quenching of these levels on account of collisions with atoms and molecules is much lower than for the level 7*d*. For this reason, the orange flashes are observed both inside and outside the pinch.

As is seen in Fig. 2, after displaying superluminescence, the intensity of observed lines drops to a minimum for sufficiently long periods (~1*s*), which are

determined by the velocity of acoustic flow. Under our experimental conditions (tube radius $R \approx 3$ cm, sound wavelength $\lambda = 200$ cm, $T \approx 400$ K, $P \approx 100$ mm Hg, and 83 dB intensity of sound wave), the velocity of acoustic flow $U \sim 0.1$–0.2 cm/s. For these velocities, the charged particles cover the distance from the center of the discharge (diam. 2–3 cm) to the radial boundary in ~1*s*. So, after superluminescence (i.e., the stimulated depopulation of the levels 7*s*, 6*s*, 7*d*), approximately 1*s* is required to restore the population of these levels that existed prior to flashing.

The hysteresis-type dependence of the intensity of the above spectral lines on sound wave intensity is probably connected with the effect of generation of space harmonics of the major acoustic vortex [7].

Finally, we arrive at the following conclusion about the dynamics of this effect. The acoustic vortices that arise in the case of sufficiently intensive acoustic field transfer cool neutral atoms and charged particles in the radial plane in the discharge tube. At a definite value of the velocity of these motions, some regions emerge at specific locations of the tube (either in the discharge pinch or out of it), where an intense recombination of charged particles takes place (in this case, the dissociative recombination). As a consequence of this recombination, the concentration of highly excited atoms in the mentioned locations abruptly increases. Due to quenching of highly excited atoms at the collisions with atoms and molecules, the population of levels 6*s*, 7*s*, 7*d* is increased. The observed flashes occur when the overpopulation threshold for superluminescence between levels $6s \longrightarrow 4p$, $7d \longrightarrow 4p$, $7s \longrightarrow 4p$ is passed.

From the above-stated, it is possible to make the following conclusion. For realization of the observed effect, acoustic vibrations are not essential. The same effect can be caused by vortical flows generated in another way, if the speed of a flow does not result in a significant decrease in the temperature radial gradient. The strong flow will result in discharge decontraction [9], when, in the given experiment, the speed of flow comes to ~0.2 cm/s.

It is worth noting that such a recombinational superluminescence is also observed in astrophysical objects [15, 16]. One could say that the obtained effect in the gas discharge plasma may be used for modeling similar observed phenomena in astrophysics.

I am grateful to Academician A.R. Mkrtchyan for his continuous attention, discussions, and assistance in this work.

REFERENCES

1. A. I. Osipov and A. V. Uvarov, Usp. Fiz. Nauk **162** (11), 1 (1992) [Sov. Phys. Usp. **35**, 903 (1992)].
2. G. A. Galechyan, Usp. Fiz. Nauk **165**, 1357 (1995) [Phys. Usp. **38**, 1309 (1995)].
3. G. Martaza and M. Y. Yu, J. Plasma Phys. **57**, 835 (1997).
4. A. Aramyan, Pis'ma Zh. Éksp. Teor. Fiz. **69**, 355 (1999) [JETP Lett. **69**, 383 (1999)].
5. A. Aramyan, physics/0207014.
6. O. V. Rudenko and S. I. Soulyan, *Theoretical Foundations of Nonlinear Acoustics* (Nauka, Moscow, 1975; Consultants Bureau, New York, 1977).
7. K. Z. Hatsagortsyan and G. Galechyan, Laser Phys. **4**, 3 (1994).
8. Quan Qi, R. E. Johnson, and J. G. Harris, J. Acoust. Soc. Am. **97**, 1499 (1995).
9. A. Aramyan, A. Mkrtchyan, and G. Galechyan, Akust. Zh. **37**, 414 (1991) [Sov. Phys. Acoust. **37**, 213 (1991)].
10. A. V. Eletskiĭ, Usp. Fiz. Nauk **136**, 25 (1982) [Sov. Phys. Usp. **25**, 13 (1982)].
11. W. L. Borst and E. C. Zipf, Phys. Rev. A **4**, 153 (1971).
12. R. S. Frend, J. Chem. Phys. **54**, 3125 (1971).
13. N. F. Mott and H. S. W. Massey, *The Theory of Atomic Collisions*, 3rd ed. (Clarendon Press, Oxford, 1965; Mir, Moscow, 1969).
14. B. M. Smirnov, *The Excited Atoms* (Énergoizdat, Moscow, 1982).
15. C. Thum, V. S. Strelnitski, J. Martin-Pintado, *et al.*, Astron. Astrophys. **300**, 843 (1995).
16. K. Davidson, D. Ebbets, S. Johansson, *et al.*, Astron. J. **113**, 335 (1997).

JETP Letters, Vol. 77, No. 6, 2003, pp. 280–284. Translated from Pis'ma v Zhurnal Éksperimental'noĭ i Teoreticheskoĭ Fiziki, Vol. 77, No. 6, 2003, pp. 330–334.

Experimental Study on the Possibility of Formation of a Condensate of Excited States in a Substance (Rydberg Matter)

V. I. Yarygin*, V. N. Sidel'nikov, I. I. Kasikov, V. S. Mironov, and S. M. Tulin

State Scientific Center Leĭpunskiĭ Institute of Physics and Power Engineering, pl. Bondarenko 1, Obninsk, Kaluga region, 249033 Russia

** e-mail: ecs@ippe.obninsk.ru*

Received February 13, 2003

The results of experimental study of a condensate of cesium excited states (Rydberg matter) are presented. The possibility of condensate formation was predicted theoretically first by Prof. É.A. Manykin and coauthors from the Russian Research Center Kurchatov Institute and experimentally observed by L. Holmlid and coauthors from the Chalmers University, Sweden. In a thermionic energy converter with interelectrode medium, where, according to the data of Swedish researchers, Rydberg matter is formed, we observed similarities and distinctions between our and Swedish data on the formation of a condensate of cesium excited states. © *2003 MAIK "Nauka/Interperiodica".*

PACS numbers: 64.70.-p; 64.60.My; 32.80.Rm; 79.40.+z

1. Introduction. For an excitation energy close to the ionization energy, alkali metal atoms reach 10^{-6}–10^{-5} cm in size. At a density of ~10^{17}–10^{18} cm^{-3}, such highly excited atoms may form a metastable condensate with a free gas of valence electrons. The possibility of the condensate of excited states (CES) existing at zero temperature was predicted in the theoretical works of Prof. É.A. Manykin with coauthors from the Russian Research Center Kurchatov Institute [1–3]. The region of CES existence at nonzero temperatures was theoretically determined by Prof. G.É. Norman in [4].

According to the calculations, cesium CES possesses the following properties at a density of 10^{17}–10^{18} cm^{-3}: binding energy ~0.1 eV, melting point 450–550 K, lifetime up to ~100 h, resistivity ~10^{-3} Ω m, and electron work function ~0.2 eV. Note that the CES possesses high internal energy (~4 eV/atom for cesium). Macroscopic amounts of condensate cannot arise under the equilibrium isothermal conditions. At the same time, the energy release in such a large amount upon the CES decay can serve as a direct proof of the CES existence.

At present, the methods of obtaining CES are not described in the literature. However, a group of Swedish researchers at Chalmers University has performed experiments that confirm, in their opinion, the existence of CES [5, 6]. The Swedish researchers called this substance Rydberg matter (RM). Their main results were obtained in the experiments with a laboratory thermionic converter (TIC). The TIC was a cesium diode, whose electrodes (emitter and collector) were kept at different temperatures; cesium vapor was fed through a grid collector into the interelectrode gap (IEG) and then condensed at the walls of vacuum cap, where the TIC was placed. This provided continuous circulation of the cesium vapor through a collector containing many holes (~10^3 cm^{-2}; hole diameter ~0.1 mm) and through the IEG. The hole-free collector surface was covered with a thin carbon layer using a colloidal graphite solution (Aquadag).

The experimentally observed TIC characteristics with dynamic feed of cesium vapor into the IEG gave evidence for the unusual properties of the interelectrode medium and of the state of electrode surfaces. This can be explained by the assumption that CES exists in the interelectrode gap. The unusual shapes of TIC current–voltage characteristics (CVCs) in the Swedish experiments were considered as the main evidence of RM formation. It was established in those experiments that, in the working regimes, a high back current (the collector work function decreased to <0.7 eV) and the CVC transition to the electric-energy generation quadrant (the output voltage increased drastically [6]) were the main evidence of the CES (RM) formation. It was found experimentally that the Rydberg particles are formed in a large amount at the surface, covered with carbon or metal oxides, and do not form at a metallic surface. Mass-spectrometric analysis showed the presence of heavy clusters (up to 10^3 atoms) in the interelectrode gap.

The authors of [6, 7] pointed out that electrode activation in TIC before the experiment is a necessary condition for obtaining RM. The activation parameters are as follows: emitter temperature T_E = 1570 K, collector

temperature T_C = 670 K, cesium reservoir temperature T_{Cs} = 570 K, and the activation time should be no less than 1 h. They also pointed out that, under Rydberg conditions, the IEG was dark and emitted appreciably weaker visible radiation, as compared to the ordinary plasma regime [5].

The main purpose of our experiments was the independent repetition of the results and conclusions of Swedish researchers about the existence of RM. Our experiments were performed with a more perfect (regarding the apparatus and technique) laboratory TIC equipped with an original grid collector and colloidal graphite solution Aquadag, which were kindly provided us by R. Svensson. It was necessary to compare, in a single experiment with a constant systematic error, the TIC characteristics under the conditions of dynamic feed of cesium vapor into IEG (as in the Swedish experiments) and the traditional feed from the cesium reservoir.

2. Experimental. The cesium CES was formed in a laboratory TIC with flat electrodes and variable IEG (d = 0.2–3 mm) containing vacuum cesium injection track and allowing either the equilibrium of dynamic feed of cesium vapor to be performed under conditions of a single experiment. As in the Swedish experiments, the following materials were used as TIC electrodes: the emitter was a polycrystalline molybdenum vacuum-melt pellet with a diameter of 14 mm and a thickness of 11 mm and the collimator was a tantalum 0.2-mm-thick foil disk with a diameter of 8 mm.

In the central part of collector (4 × 3.1 mm), 400 holes with a diameter of 0.1 mm were punched by a laser beam. The hole-free collector surface was covered (using Aquadag) with a carbon layer 0.1–0.2 mm in thickness.

The emitter pellet had a single hole (1 mm in diameter) at its side surface to simulate a black body and independently measure temperature using a reference optical micropyrometer and also had five holes on the inside for placing tungsten–rhenium thermocouples in them. The emitter was heated by electron bombardment.

The TIC frame contained two viewing leucosapphire windows, through which the IEG was measured using an optical instrument (cathetometer KM-6) and the visual observations were carried out (photographing, video photography, etc.). The TIC and emitter heater cavity were pumped out by high-vacuum electric-discharge pumps NORD-100.

The preparation of TIC for measurements included conventional degassing procedures [8].

With the dynamic feed of cesium vapor, it was led along high-pressure cesium tracks to the grid collector, passed through it to IEG and then into the TIC working cavity, condensed at the cold walls of the low-pressure vacuum tracks and drained down into a liquid cesium receiver. The stored liquid cesium was sufficient for several working hours. Next, cesium was carried from the cesium receiver to the working Cs thermostat. After this, the measurement and CVC optimization run was repeated.

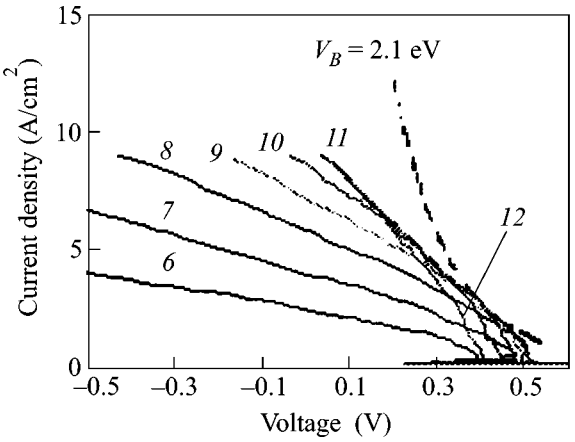

Fig. 1. Equilibrium cesium feed regime. The CVC family for different temperatures of cesium reservoir and T_E = 1573 K, T_C = 900 K, and d = 0.3 mm; (*5*) T_{Cs} = 528.7 K and P_{Cs} = 0.585 mm Hg; (*6*) T_{Cs} = 539.5 K and P_{Cs} = 0.817 mm Hg; (*7*) T_{Cs} = 551.3 K and P_{Cs} = 1.16 mm Hg; (*8*) T_{Cs} = 562.7 K and P_{Cs} = 1.6 mm Hg; (*9*) T_{Cs} = 571.3 K and P_{Cs} = 2.03 mm Hg; (*10*) T_{Cs} = 580.2 K and P_{Cs} = 2.57 mm Hg; (*11*) T_{Cs} = 587.5 K and P_{Cs} = 3.1 mm Hg; and (*12*) T_{Cs} = 594.7 K and P_{Cs} = 3.72 mm Hg.

In the case of equilibrium feed, the cesium vapor pressure in the IEG and the TIC working cavity was determined by the cesium reservoir temperature (Cs thermostat). The CVCs were measured by the pulsed method by sweeping electric current from the static working point, which, as a rule, corresponded to the diffusional TIC regime [9].

After completing the first stage of measurements (measurement and optimization of CVC for the equilibrium feed), the TIC electrodes were activated following the regime proposed by the Swedish researchers in [6, 7].

In the course of experimental studies, the transition from equilibrium feed to the dynamic feed and back to the equilibrium feed was performed several ten times.

2.1. Results. In the case of the equilibrium feed of cesium vapor, the TIC CVCs were measured to determine reference points (starting database) for the purpose of comparison with the TIC characteristics that were obtained in the simulation of the CES formation conditions. One of the resulting CVC families obtained upon measuring the temperature of cesium reservoir at T_E = 1573 K is shown in Fig. 1. The emitting working area in TIC was taken to be equal to the total collector area (S_C = 0.5 cm^2). The optimization (with respect to T_{Cs}, d, and T_C) of the TIC output electric characteristics showed that they corresponded to the minimal barrier index V_B = 2.1 eV. In the working region of parameter T_E/T_{Cs} = 2.3–3.0, the emitter vacuum work function

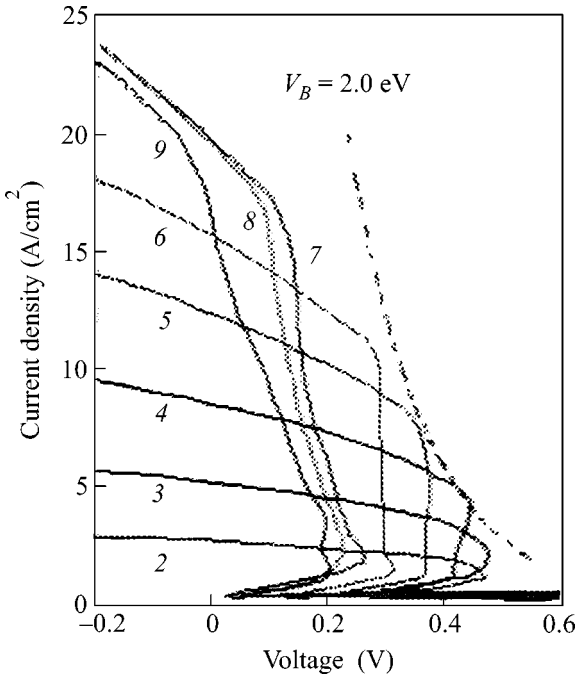

Fig. 2. Dynamic cesium feed regime. The CVC family for different temperatures of cesium reservoir and T_E = 1572 K, T_C = 903 K, and d = 0.3 mm; (2) T_{Cs} = 602.2 K and P_{Cs} = 4.47 mm Hg; (*3*) T_{Cs} = 616.6 K and P_{Cs} = 6.28 mm Hg; (*4*) T_{Cs} = 628.1 K and P_{Cs} = 8.14 mm Hg; (*5*)T_{Cs} = 638.1 K and P_{Cs} = 10.1 mm Hg; (*6*) T_{Cs} = 646.4 K and P_{Cs} = 12.1 mm Hg; (*7*) T_{Cs} = 655.2 K and P_{Cs} = 14.5 mm Hg; (*8*) T_{Cs} = 656.4 K and P_{Cs} = 14.8 mm Hg; and (*9*) T_{Cs} = 660.4 K and P_{Cs} = 16.1 mm Hg.

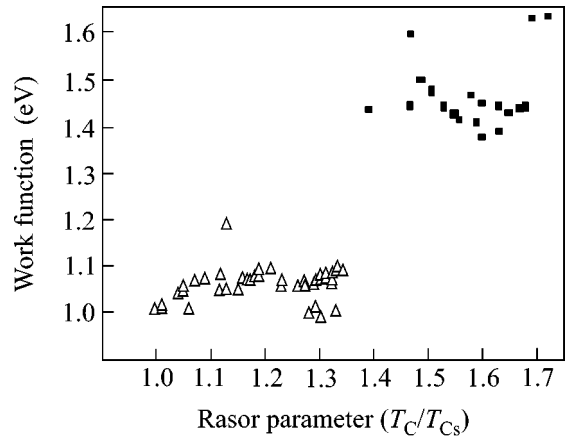

Fig. 3. Comparison of the collector work functions $\Phi_C^{E_m}$ obtained from the emission measurements with different methods of feeding cesium vapor. Feed regime: ■ equilibrium and △ dynamic.

was Φ_{E0} = 4.6–4.7 eV. It is typical of polycrystalline molybdenum. The work function Φ_{E0} was virtually independent of the collector temperature in the range of working temperatures T_C = 740–950 K, indicating the absence of oxygen-containing impurities in the interelectrode medium. These data are typical for the usual characteristics of TICs operating in the standard low-voltage arc discharge regime with an electrode pair that is analogous to Mo–Ta and is not optimal for achieving high TIC efficiency against the V_B criterion [10].

In the case of dynamic feed of cesium vapor into the IEG, the CVC measurements and optimization were performed over a wide range of parameters T_E, T_{Cs}, d, and T_C. Figure 2 presents an example of such a CVC family for the same T_E, T_C, and d values as in Fig. 1. The emitting (working) area was taken to be equal to the collector area S_C = 0.125 cm^2 (the area of the grid part of collector). The visual observation and video photography of the IEG and its environment with a magnification of ×25, without and with illumination by a diode laser, and the monitoring of the character and shape of a low-voltage arc discharge glow at the TV display suggested that the discharge electric current was "locked" to this emitting (working) electrode area. Note that, according to the similar IEG monitoring data in the case of equilibrium feed, the discharge occurred from the entire collector area (S_C = 0.5 cm^2).

In the experiments with the dynamic feed of cesium vapor, we determined the collector emission characteristics and the energetic effects in the interelectrode medium. Although we call them "anomalous," they can be, in principle, related to the CES (RM) that was observed by the Swedish researchers. These are, primarily, a decrease in the collector work function from 1.4–1.5 eV for the equilibrium feed to 1.0–1.1 eV for the dynamic feed and the appearance of a green-colored plasma drop fraction.

The results of emission measurements for the collector work function $\Phi_C^{E_m}$ as a function of the Rasor parameter are given in Fig. 3.

2.2. Appearance of a plasma drop fraction. In the dynamic feed regimes, the collector surface was in one of the three states; (1) the surface was covered with a stable and visible cesium film, and there was no excess pressure in the cesium feed chamber; (2) the surface was "dry," and the excess pressure in the cesium feed chamber was 25–50 mm Hg; and (3) a visible cesium film appeared periodically at the surface, and there was an excess pressure in the cesium-vapor feed chamber. The first state lasted 10–15 min, and the second state lasted several hours. In the first and second states, the low-voltage arc discharge had the ordinary shape, and the CVC showed no sizable qualitative and quantitative anomalies.

The third state appeared periodically during ~1 h. As in case (2), the operation time was limited by the store of cesium in the working reservoir (Cs thermostat). In the full cycle of this state, one can also distinguish between three phases: (a) the collector is dry; (b) the collector is covered with a visible liquid cesium film; and (c) spraying of cesium drops with "drying"

the collector surface. The maintenance of this state, the cycle duration, and the duration of cycle phases depended on the ratio between the collector and reservoir temperatures.

When the TIC was at the short-circuit point of the diffusional CVC portion during the entire measurement time, no anomalous phenomena were observed. If, in the course of voltage sweep for measuring CVC, the discharges occurred in the (a) or (b) phase, the CVC and the character of low-voltage arc discharge were of the usual type. However, when the discharge coincided with phase (c), an unusual glow appeared with a certain time delay from the main discharge in the space between the electrodes (IEG) and the outer (with respect to IEG) walls of the laboratory TIC frame. The frame was under the emitter voltage and separated from the electrodes by a distance of 2–3 cm. The observed glow color (light green) differed strongly from the traditional color of the main discharge (red tones). The glow had a short duration and, unfortunately, we have failed, at the present stage of investigation, to record CVC at the instant the green-colored cesium plasma drop fraction appeared.

From the results of our experiments, one can state that the light-green glow of the plasma drop fraction arises only under the combined action of two factors: cesium vapor circulation and the TIC IEG breakdown. Note that, in the previous experiments with dynamic feed of cesium vapor through a hole in a collector [11], the current flowing in the center and periphery of the collector was highly inhomogeneous and the emitter erosion was observed, which can occur only under the combined action of the discharge and circulation on the IEG.

Due to a high internal energy, the CES can arise only in the presence of energy sources. In our experiments, two such energy sources are present. The first consists of the isothermal expansion of cesium vapor in the holes of the grid collector. We have established that, when cesium vapor passes through the collector, its pressure decreases almost tenfold. In this case, the work per molecule is ~0.1–0.2 eV. However, only 2–5% of flowing vapor can transform into CES even for the best use of this energy. A low-voltage electric discharge is another energy source. Estimates show that the energy liberated in this discharge is an order of magnitude higher than the cesium vapor expansion work.

Since, according to our data, the electric discharge is necessary for the CES formation, some distinctions between our characteristics and the Swedish data, for which the discharge pulse repetition rate was several times (~3) higher than in our experiments, can be explained. It is conceivable that this fact did not allow us to completely reproduce the CES (RM) characteristics at the present stage of investigations.

3. Calculated estimates of cluster size in the plasma drop fraction. When the cesium drops sprayed from the collector fall on the emitter or hot walls of the TIC frame surrounding the electrodes, they are rapidly evaporated. In the case of dynamic cesium-vapor feed into the IEG, a combined plasma is formed, which is composed of electrons, ions, neutral atoms, and liquid cesium drops of different size.

Let us estimate the decay time of such plasma after switching off the electric fields. The decay of low-temperature plasma in the IEG with $d = 0.1$–1.0 cm is mainly due to the ions that go out to the electrodes and loose their charge. The characteristic plasma-decay time, i.e., the time plasma density to decrease by e times, is $t_0 = d^2/lv$, where $l \approx 10^{-3}$ cm is the mean free path of the cesium ions ($P_{Cs} \approx 1$ mm Hg), and $v \approx 10^4$ cm/s is their thermal velocity [12].

The concentration of excited cesium atoms decreases with approximately the same characteristic time.

For the IEG with $d = 0.1$ cm, the characteristic decay time is found to be $t_0 \approx 10^{-3}$ s and, for $d = 1$ cm, $t_0 \approx 0.1$ s.

In our experiment, the green glow of the plasma drop fraction was observed for several seconds in the IEG and in the near-electrode zone with characteristic $d = 1$ cm. This is 10–100 times longer than the decay time of cluster-free plasma.

Consequently, the experimentally observed plasma fraction contained clusters with mass corresponding to ≈100 atoms. Note that, according to the Swedish data, the clusters formed in RM may contain several hundred of cesium atoms (up to 1000).

Therefore, the estimate of plasma decay rate from the data of our measurements under the conditions of CES formation in the form of green-colored interelectrode medium in the cesium TIC with dynamic feed of cesium vapor give evidence for the presence of a plasma drop fraction in the form of clusters with a mass of ~10^2 excited or ionized cesium atoms.

We are grateful to R. Svensson from Sweden for providing us with the samples of collector materials to study Rydberg matter and to the participants of the Scientific and Coordinating Session “Investigations of Nonideal Plasma” (December 3 and 4, 2002; under the leadership of Academician V.E. Fortov) of the Scientific Council on Physics of Low-Temperature Plasma, the Russian Academy of Sciences, for discussion.

This work was supported by the Russian Foundation for Basic Research, project no. 02-02-96021.

REFERENCES

1. É. A. Manykin, M. I. Ozhovan, and P. P. Poluéktov, Dokl. Akad. Nauk SSSR **260**, 1096 (1981) [Sov. Phys. Dokl. **26**, 974 (1981)].
2. E. A. Manykin, in *Proceedings of Thermionic Energy Conversion Specialist Conference* (Göteborg, 1993), p. 35.
3. É. A. Manykin, M. I. Ozhovan, and P. P. Poluéktov, Khim. Fiz. **18**, 87 (1999).

4. G. É. Norman, Pis'ma Zh. Éksp. Teor. Fiz. **73**, 13 (2001) [JETP Lett. **73**, 10 (2001)].
5. L. Holmlid, in *Proceedings of Thermionic Energy Conversion Specialist Conference* (Göteborg, 1993), p. 47.
6. R. Svensson, L. Holmlid, and E. Kennel, in *Proceedings of Thermionic Energy Conversion Specialist Conference* (Göteborg, 1993), p. 93.
7. R. Svensson and L. Holmlid, in *Proceedings of the 32nd Intersociety Energy Conversion Engineering Conference, Honolulu, Hawaii* (1997), p. 1071.
8. S. Dushman, *Scientific Foundations of Vacuum Technique*, 2nd ed. (Wiley, New York, 1962; Mir, Moscow, 1964).
9. A. V. Andriashin, E. A. Meleta, V. S. Mironov, *et al.*, in *Selected Works of GNTs RF-FÉI, 1996* (Inst. of Physics and Power Engineering, Obninsk, 1997), p. 97.
10. V. I. Yarygin, Doctoral Dissertation in Engineering (Inst. of Physics and Power Engineering, Obninsk, 1999).
11. V. K. Tskhakaya and V. I. Yarygin, Pis'ma Zh. Tekh. Fiz. **1**, 25 (1975) [Sov. Tech. Phys. Lett. **1**, 10 (1975)].
12. *Physical Foundations of Thermal Emission Energy Transformation*, Ed. by I. P. Stakhanov (Atomizdat, Moscow, 1973).

Translated by V. Sakun

JETP Letters, Vol. 77, No. 6, 2003, pp. 285–290. From Pis'ma v Zhurnal Éksperimental'noĭ i Teoreticheskoĭ Fiziki, Vol. 77, No. 6, 2003, pp. 335–340.

Effects of the Mixture of One- and Three-Dimensional Inhomogeneities on the Wave Spectrum of Superlattices¶

V. A. Ignatchenko*, Yu. I. Mankov*, and A. A. Maradudin**

** Kirensky Institute of Physics, Krasnoyarsk, 660036 Russia*

*** Department of Physics and Astronomy, University of California, Irvine CA 92697, USA*

e-mail: ignatchenko@theorphys.krasn.ru

Received February 10, 2003

Dependences of the dispersion laws and damping of waves in an initially sinusoidal superlattice on the dimensionality of inhomogeneities modulating the period of the superlattice are studied. The cases of one- and three-dimensional modulations, as well as modulation by a mixture of inhomogeneities of both of these dimensionalities, are considered. The correlation function of the superlattice $K(\mathbf{r})$ has the form of a product of the same periodic function and a decreasing function that is significantly different for these different cases. The decreasing part of the correlation function for the mixture of inhomogeneities of different dimensionalities has the form of a product of the decreasing parts of the correlation functions of the components of the mixture. This leads to the nonadditivity of the contributions of the components of different dimensionalities to the resulting modification of the parameters of the wave spectrum that are due to the inhomogeneities (the damping of waves for the mixture of these components is smaller than the sum of the dampings of the components, the maximum gap in the spectrum corresponds to the simultaneous presence of both components of the mixture, not only of the three-dimensional inhomogeneities). © *2003 MAIK "Nauka/Interperiodica".*

PACS numbers: 68.65.Cd

1. Investigations of the spectrum of waves in partially randomized superlattices (SLs) have been carried out very intensively in recent years. This is due to the wide use of these materials in various high-technology devices, as well as to the fact that they are convenient models for developing new methods of theoretical physics for studying media without translation symmetry. Several methods now exist for developing a theory of such SLs: the modeling of the randomization by altering the order of successive layers of two different materials [1–7]; the numerical modeling of the random derivations of the interfaces between layers from their initial periodic arrangement [8–10]; the postulation of the form of the correlation function of a SL with inhomogeneities [11, 12]; the application of the geometrical optics approximation [13]; and the development of the dynamic composite elastic medium theory [14].

One more method for the investigation of the influence of inhomogeneities on the wave spectrum of a SL was suggested in [15]: the method of the random spatial modulation (RSM) of the period of the SL. This method is an extension of the well-known theory of the random frequency (phase) modulation of a radio signal [16, 17] to the case of spatial inhomogeneities in the SL. The advantage of this method is that the form of the correlation function (CF) of the SL is not postulated but is developed from the most general assumptions about the nature of a random spatial modulation of the SL period. It appeared that in the general case this function had quite a complicated form that depended on the dimensionality of the inhomogeneities. Knowledge of the CF corresponding to a particular type and dimensionality of the inhomogeneities permitted us to apply methods of investigation of averaged Green's functions to find the energy spectrum and other characteristics of the waves [15, 18–23]. The RSM method permitted us to consider inhomogeneities of different dimensionalities in the framework of the same model. Effects of one-dimensional (1D) and three-dimensional (3D) inhomogeneities on the wave spectrum were studied for sinusoidal SLs, SLs with sharp interfaces, and SLs with arbitrary thicknesses of interfaces. The influence of inhomogeneities of each dimensionality was studied separately. So, a significant aspect of the problem that was not considered up to now is the situation when inhomogeneities of different dimensionalities are present simultaneously in a superlattice. The study of this aspect is the objective of the present work.

2. Model and correlation function. A SL is characterized by the dependence of some material parameter A on the coordinates $\mathbf{x} = \{x, y, z\}$. The physical nature of the parameter $A(\mathbf{x})$ can be different. This parameter can be a density of matter or a force constant for the elastic system of a medium, the magnetization, anisotropy, or exchange for a magnetic system, and so on. We represent $A(\mathbf{x})$ in the form

$$A(\mathbf{x}) = A[1 + \gamma\rho(\mathbf{x})], \quad (1)$$

¶ This article was submitted by the authors in English.

where A is the average value of the parameter, γ is its relative rms variation, and $\rho(\mathbf{x})$ is a centered ($\langle\rho(\mathbf{x})\rangle = 0$) and normalized ($\langle\rho^2(\mathbf{x})\rangle = 1$) function. The function $\rho(\mathbf{x})$ describes the periodic dependence of the parameter along the SL axis z, as well as the random spatial modulation of this parameter, which, in the general case, can be a function of all three coordinates $\mathbf{x} = \{x, y, z\}$.

We will consider in this paper a SL that has a sinusoidal dependence of the material parameter on the coordinate z in the initial state when inhomogeneities are absent. According to the RSM method, we represent the function $\rho(\mathbf{x})$ in the form

$$\rho(\mathbf{x}) = \sqrt{2}\cos[q(z - u_1(z) - u_3(\mathbf{x})) + \psi], \quad (2)$$

where $q = 2\pi/l$ is the SL wave number.

The function $u_1(z)$ describes 1D inhomogeneities of the phase of the function $\rho(\mathbf{x})$. The sensitivity of the profile of the function $\rho(\mathbf{x})$ to the action of the modulation $u_1(z)$ is different for different points of the function $\rho(\mathbf{x})$. The smallest changes of the profile occur in the vicinities of the minima and maxima of the function $\cos(qz)$. In contrast to this, the displacements of the zero points of $\cos(qz)$ by the values of $u_1(z)$ lead to the strongest changes in the profile. The zero points of the function $\rho(\mathbf{x})$ correspond to the interfaces of the SL. Because of this, we assume in the RSM method that the function $u_1(z)$ models 1D displacements of the interfaces from their initial periodic arrangement.

The function $u_3(\mathbf{x})$ is introduced in Eq. (2) to model a random deformation of the surfaces of the interfaces. At first glance, it would seem that this function must depend only on the two coordinates, x and y. But the function $u(x, y)$ describes in the RSM method a 2D deformation that is uniform for all interfaces of the SL, i.e., that has an infinite value of the correlation radius along the z coordinate. The directly opposed cases are of interest in reality, namely, the cases where the deformations of the two nearest interfaces are uncorrelated (the correlation radius along z is much smaller than $l/2$) or only several interfaces are correlated. That is why $u_3(\mathbf{x})$ must be a random function of all three coordinates x, y, and z.

In the general case, this function has an anisotropy of correlation properties, because the values of the correlation radii in the xy plane and along the z axis are determined by different physical reasons. But we restrict ourselves here to the simplest case and assume that $u_3(\mathbf{x})$ is a 3D random function with isotropic correlation properties. A coordinate-independent random phase ψ is introduced into Eq. (2) to ensure the fulfillment of the condition of ergodicity for the function $\rho(\mathbf{x})$ (see [15]); it is characterized by a uniform distribution in the interval $(-\pi, \pi)$. After averaging the product of the functions $\rho(\mathbf{x})$ and $\rho(\mathbf{x} + \mathbf{r})$ over the phase ψ, we obtain

$$\langle\rho(\mathbf{x})\rho(\mathbf{x} + \mathbf{r})\rangle_\psi = \cos(qr_z - \chi_1 - \chi_3), \quad (3)$$

where

$$\begin{aligned}\chi_1 &= q[u_1(z + r_z) - u_1(z)],\\ \chi_3 &= q[u_3(\mathbf{x} + \mathbf{r}) - u_3(\mathbf{x})].\end{aligned} \quad (4)$$

We assume that the random functions χ_1 and χ_3 are mutually uncorrelated and that each of them is a Gaussian random process. After averaging Eq. (3) over χ_1 and χ_3, we obtain a general expression for the CF of the SL in the form

$$K(\mathbf{r}) = \cos(qr_z)K_1(r_z)K_3(r), \quad (5)$$

where

$$K_1(r_z) = \exp\left[-\frac{1}{2}Q_1(r_z)\right], \quad (6)$$

$$K_3(r) = \exp\left[-\frac{1}{2}Q_3(r)\right], \quad (7)$$

and the structure functions $Q_i(\mathbf{r})$ are defined by the equations

$$Q_1(r_z) = \langle\chi_1^2\rangle, \quad Q_3(r) = \langle\chi_3^2\rangle. \quad (8)$$

One can see from Eqs. (6)–(8) that $K_1(r_z)$ and $K_3(\mathbf{r})$ are the decreasing parts of the CFs of the SLs with 1D or 3D inhomogeneities (recall that the complete CFs for these cases have the form of the product of $\cos(qr_z)$ and $K_1(r_z)$ or $K_3(\mathbf{r})$, respectively [15]. So, the decreasing part of the CF of a SL with a mixture of the mutually uncorrelated phase inhomogeneities of different dimensionalities has the form of the product of the decreasing parts of the CFs of the components of this mixture.

To find the structure functions $Q_1(r_z)$ and $Q_3(r)$, we must model the correlation properties of the modulating functions $u_1(z)$ and $u_3(\mathbf{x})$ or, more precisely, the correlation properties of their gradients. Both $Q_1(r_z)$ and $Q_3(r)$ were found in [15] (see also some refinements of the coefficients in these expressions in [21]) by the use of different forms of the model CFs for the random modulation. It was shown that the forms of the functions Q_i do not depend asymptotically (for both small and large values of r) on the form of the model CF but strictly depend on the dimensionalities of the inhomogeneities. For the exponential model CFs for $u_1(z)$ and $u_3(\mathbf{x})$, the structure functions were obtained in the forms

$$Q_1(r_z) = 2\gamma_1^2[\exp(-k_\parallel r_z) + k_\parallel r_z - 1], \quad (9)$$

$$Q_3(r) = 6\gamma_3^2\left[1 - \frac{2}{k_0 r} + \left(1 + \frac{2}{k_0 r}\right)\exp(-k_0 r)\right], \quad (10)$$

where γ_1 and $k_\parallel$ are the relative rms fluctuation and correlation wave number of the random modulation $u_1(z)$,

γ_3 and k_0 are the corresponding characteristics of the random modulation $u_3(\mathbf{x})$.

After the substitution of Eqs. (9) and (10) into them, Eqs. (6) and (7) become quite complicated. That is why approximate expressions for $K_1(r_z)$ and $K_3(r)$ were suggested for the 1D and 3D inhomogeneities (see [15, 23], respectively):

$$K_1(r_z) = \exp(-\gamma_1^2 k_\parallel r_z), \quad (11)$$

$$K_3(r) = (1-L)\exp(-\gamma_3^2 k_0 r) + L, \quad (12)$$

where $L = \exp(-3\gamma_3^2)$ is the asymptotic form of $K_3(r)$ when $r \longrightarrow \infty$.

According to these equations, effective correlation radii of the SL can be introduced for the 1D and 3D cases, respectively:

$$r_1 = (\gamma_1^2 k_\parallel)^{-1}, \quad r_3 = (\gamma_3^2 k_0)^{-1}. \quad (13)$$

One can see that the effective correlation radii of the SL depend not only on the correlation radii $k_\parallel^{-1}$ or k_0^{-1} of the corresponding modulating functions u_1 or u_3 but also on the rms fluctuations of these functions, γ_1 or γ_3.

3. Dispersion law and damping of waves. We consider the equation for waves in the superlattice in the form

$$\nabla^2\mu + (\nu - \varepsilon\rho(\mathbf{x}))\nu = 0, \quad (14)$$

where the expressions for the parameters ε and ν and the variable μ are different for waves of different natures. For spin waves, when the parameter of the superlattice $A(\mathbf{x})$ in Eq. (1) is the value of the magnetic anisotropy $\beta(\mathbf{x})$, we have [15] $\nu = (\omega - \omega_0)/\alpha g M$, $\varepsilon = \gamma\beta/\alpha$, where ω is the frequency, $\omega_0 = g(H + \beta M)$, g is the gyro-magnetic ratio, α is the exchange parameter, H is the magnetic field strength, M is the value of the magnetization, β is the average value of the anisotropy, and γ is its relative rms variation. For elastic waves in the scalar approximation, we have $\nu = (\omega/v)^2$, $\varepsilon = \gamma\nu$, where γ is the rms fluctuation of the density of the material and v is the wave velocity. For an electromagnetic wave in the same approximation, we have $\nu = \epsilon_e(\omega/c)^2$, $\varepsilon = \gamma\nu$, where ϵ_e is the average value of the dielectric permeability, γ is its rms deviation, and c is the speed of light.

Laws of the dispersion and damping of the averaged waves are determined by the equation for the complex frequency $\nu = \nu' + i\xi$, which follows from the vanishing of the denominator of the Green's function of Eq. (14). In the Bourret approximation [24], this equation has the form [15]

$$\nu - k^2 = \varepsilon^2 \int \frac{S(\mathbf{k} - \mathbf{k}_1)d\mathbf{k}_1}{\nu - k_1^2}, \quad (15)$$

where $S(\mathbf{k})$ is the spectral density of the function $\rho(\mathbf{x})$:

$$S(\mathbf{k}) = \frac{1}{(2\pi)^3}\int K(\mathbf{r})e^{-i\mathbf{kr}}d\mathbf{r}. \quad (16)$$

Substituting Eq. (5) into Eq. (16), then Eq. (16) into Eq. (15), and approximating $K_1(r_z)$ and $K_3(r)$ by Eqs. (11) and (12), we obtain an exactly integrable expression. Upon integrating this expression with respect to $\mathbf{k}_1$ and $\mathbf{r}$, we obtain an explicit form of the equation for ν:

$$\nu - k^2 = \frac{\varepsilon^2}{2}\left\{(1-L)\frac{P_{13}}{P_3}\left[\frac{1}{P_{13}^2 - (k-q)^2} + \frac{1}{P_{13}^2 - (k+q)^2}\right] + L\frac{P_1}{\sqrt{\nu}}\left[\frac{1}{P_1^2 - (k-q)^2} + \frac{1}{P_1^2 - (k+q)^2}\right]\right\}, \quad (17)$$

where

$$P_1 = \sqrt{\nu} - ik_\parallel\gamma_1^2, \quad P_3 = \sqrt{\nu} - ik_0\gamma_3^2, \quad P_{13} = \sqrt{\nu} - i(k_\parallel\gamma_1^2 + k_0\gamma_3^2). \quad (18)$$

We consider this equation at the Brillouin zone boundary $k = k_r \equiv q/2$. Under the conditions that ε, $(k_\parallel\gamma_1^2)^2$, and $(k_0\gamma_3^2)^2$ are much smaller than $\nu_r = k_r^2$, we obtain Eq. (17) in the form of a cubic equation in ν:

$$\nu - k_r^2 = \frac{\varepsilon^2}{2}\left[\frac{1-L}{\nu - 2ik_r(k_\parallel\gamma_1^2 + k_0\gamma_3^2) - k_r^2} + \frac{L}{\nu - 2ik_r k_\parallel\gamma_1^2 - k_r^2}\right]. \quad (19)$$

Both limiting cases of this equation, corresponding to 1D ($\gamma_1 \neq 0$, $\gamma_3 = 0$) and 3D ($\gamma_1 = 0$, $\gamma_3 \neq 0$) inhomogeneities, were considered in our previous works.

The equation (19) for the mixture of 1D and 3D inhomogeneities has been investigated by numerical methods. The results of this investigation are shown in Figs. 1 and 2 by solid curves. Dotted and dashed curves in these figures correspond to the limiting cases of the presence of only 1D or 3D inhomogeneities, respectively. All figures correspond to the same correlation wave numbers for 1D ($\eta_1 \equiv k_\parallel q/\Lambda = 4$, where $\Lambda = \sqrt{2}\,\varepsilon$) and 3D ($\eta_3 \equiv k_0 q/\Lambda = 4$) inhomogeneities. Different situations are shown in these figures.

Figure 1a shows the decrease of the gap $\Delta\nu = \nu'_+ - \nu'_-$ with the increase of γ_1^2 or γ_3^2. If $\gamma_3 = 0$, the increase in γ_1^2 leads to the closing of the gap at $\gamma_1^2 = 0.25$ (dotted curve). Simultaneously the damping of both eigenfrequencies increases linearly till the point $\gamma_1^2 = 0.25$ (dot-

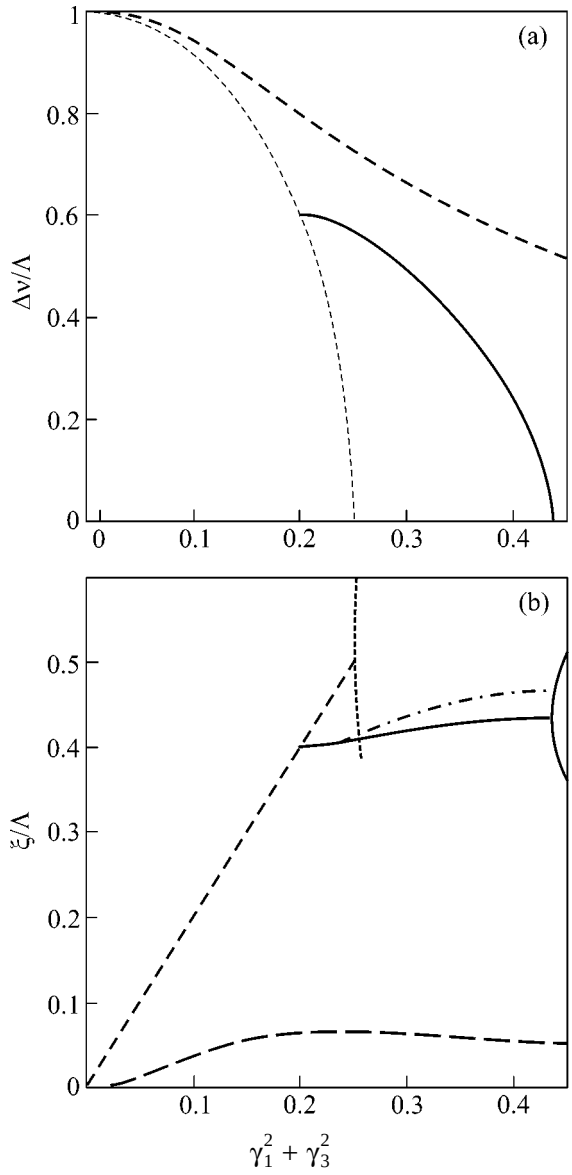

Fig. 1. The width of the (a) gap and (b) damping as functions of the sum $\gamma_1^2 + \gamma_3^2$ for different situations: $\gamma_1^2 \neq 0$, $\gamma_3^2 = 0$ (dotted curves); $\gamma_1^2 = 0$, $\gamma_3^2 \neq 0$ (dashed curves); $\gamma_1^2 = 0.2$, $\gamma_3^2 \neq 0$ (solid curves). The explanation of the dotted-dashed curve in Fig. 1b is given in the text.

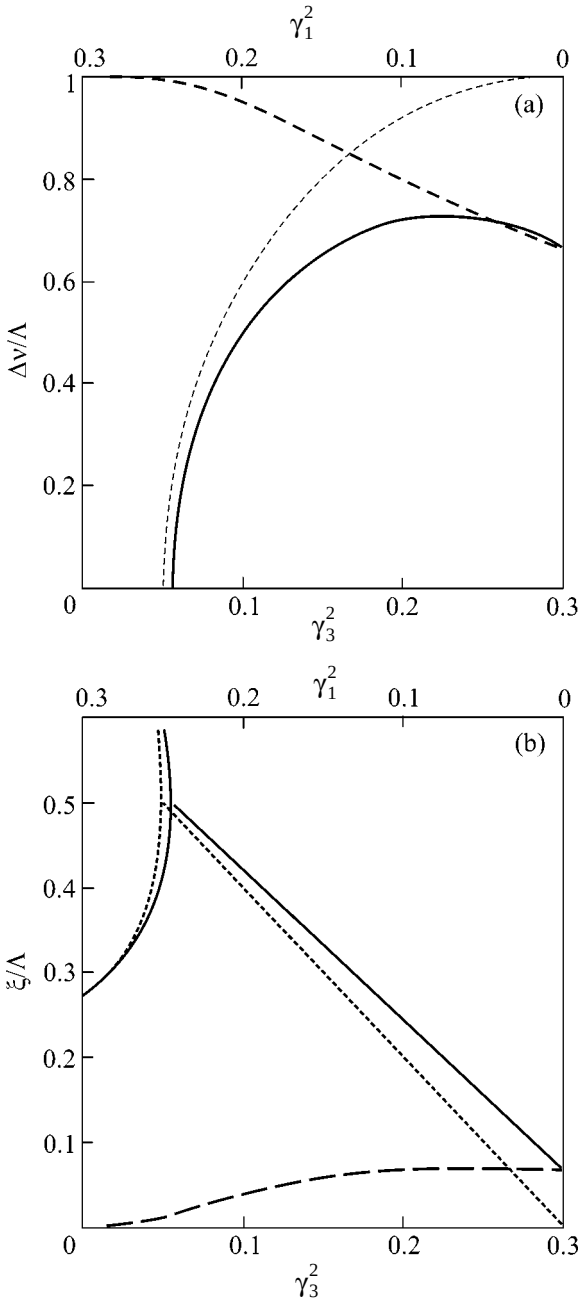

Fig. 2. The width of the (a) gap and (b) damping under the condition $\gamma_1^2 + \gamma_3^2 = 0.3$ (solid curves) and for the situations when γ_3^2 increases for $\gamma_1^2 = 0$ (dashed curves, the scale is under the picture), and when γ_1^2 decreases for $\gamma_3^2 = 0$ (dotted curves, the scale is above the picture).

ted curve in Fig. 1b). For $\gamma_1^2 > 0.25$, two degenerate eigenfrequencies $\nu'_+ = \nu'_-$ exist with different dampings, $\xi_+ \neq \xi_-$. If $\gamma_1^2 = 0$ the increase of γ_3^2 also leads to the decrease of the gap (dashed curve in Fig. 1a) but significantly more slowly than under the action of the 1D inhomogeneities. For example, a large gap exists for $\gamma_3^2 = 0.25$, while the gap closes when γ_1^2 has the same value. In line with this, the damping increases very slightly with the increase in γ_3^2 (dashed curve in Fig. 1b).

To show the effects of the mixture of inhomogeneities of different dimensionalities, the following situation is depicted in Figs. 1. Let us have only 1D inhomo-

geneities with $\gamma_1^2 = 0.2$ and, correspondingly, let the spectrum gap be $\Delta\nu/\Lambda = 0.6$. Then we add 3D inhomogeneities increasing γ_3^2 and keeping $\gamma_1^2 = 0.2$. One can see that the gap decreases slowly and closes at $\gamma_1^2 + \gamma_3^2 = 0.45$ (solid curve in Fig. 1a). Simultaneously, the increase in the damping slows down (solid curve in Fig. 1b). The dashed-dotted curve in Fig. 1b corresponds to the unreal situation that would have been realized if the damping of the mixture of 1D inhomogeneities with $\gamma_1^2 = 0.2$ and 3D inhomogeneities with γ_3^2 were equal to the simple sum of the damping of the components of the mixture. One can see that in reality the additional contribution to the damping due to 3D inhomogeneities in the presence of the 1D inhomogeneities is approximately two times smaller than in the absence of the latter.

Quite another situation is shown in Figs. 2 by the solid curves. We assume here that the sum $\gamma_1^2 + \gamma_3^2$ remains constant (and equal to 0.3 in these graphs) when γ_1^2 and γ_3^2 are varied. In other words, we consider a gradual replacement of the 1D inhomogeneities by 3D inhomogeneities with the same values of rms fluctuations. For comparison, the functions $\Delta\nu$ and ξ are shown in Figs. 2 separately for the 1D and 3D inhomogeneities. The origin of the coordinates corresponds to $\gamma_3^2 = 0$ (the scale is under the picture) and $\gamma_1^2 = 0.3$ (the scale is above the picture). The width $\Delta\nu$ of the gap is equal to zero for the 1D inhomogeneities and to Λ for the 3D inhomogeneities. The dashed curve in Fig. 2a shows the decrease in $\Delta\nu$ when γ_3^2 increases for $\gamma_1^2 = 0$. The dotted curve in this figure shows the opening and increase of $\Delta\nu$ when γ_1^2 decreases for $\gamma_3^2 = 0$. The solid curve shows the dependence of $\Delta\nu$ on γ_3^2 under the condition $\gamma_1^2 + \gamma_3^2 = 0.3$. One can see that the maximum of $\Delta\nu$ corresponds to some point corresponding to the presence of both components of the mixture ($\gamma_1^2 \neq 0$, $\gamma_3^2 \neq 0$) but not to the absence of the 1D inhomogeneities ($\gamma_1^2 = 0$, $\gamma_3^2 = 0.3$), as might be expected from the general point of view.

4. The method of the random spatial modulation of the superlattice period [15] permits developing the CF of a SL with 1D random modulation (which models random displacements of the interfaces from their initial periodic arrangement), 3D modulation (which models random deformations of the interfaces), and the simultaneous presence of both kinds of modulation (which models the mixture of the 1D and 3D inhomogeneities of the SL structure).

The decreasing part of the CF of the SL in the presence of the mixture of the 1D and 3D inhomogeneities has the form of the product of the decreasing parts of the CFs of the components of the mixture $K_1(r_z)$ and $K_3(\mathbf{r})$.

The widths of the gap in the spectrum and damping of waves at the boundary of the first Brillouin zone have the following behavior depending on the relationship between rms fluctuations γ_1 and γ_3 of the 1D and 3D inhomogeneities. On addition of the 3D inhomogeneities to the SL containing only 1D inhomogeneities, the damping of waves increases. But this additional damping is approximately half as large as the damping that is due to the inhomogeneities with the same value of γ_3^2 in the absence of the 1D inhomogeneities. The situation has also been considered when a gradual replacement of inhomogeneities of one dimensionality by inhomogeneities of the other dimensionality subject to the condition $\gamma_1^2 + \gamma_3^2 = \text{const}$ occurs. It has been shown that the maximum value of the gap corresponds to some relationship between γ_1^2 and γ_3^2 but not to $\gamma_1^2 = 0$, as one could expect from general considerations. This phenomenon, as well as the phenomenon of the reduction of the damping induced by the 3D inhomogeneities in the presence of 1D inhomogeneities, is due to the fact that the decreasing parts of the CFs of the components of the mixture $K_1(r_z)$and $K_3(\mathbf{r})$, as for the mixture of any phase inhomogeneities, enter into the CF of the SL in the form of a product, not a sum.

This work was supported by the NATO Science Program and Collaborative Linkage (Grant no. 978090) and the Russian Foundation for Basic Research (project no. 00-02-16105).

REFERENCES

1. J. M. Luck, Phys. Rev. B **39**, 5834 (1989).
2. S. Tamura and F. Nori, Phys. Rev. B **41**, 7941 (1990).
3. N. Nishiguchi, S. Tamura, and F. Nori, Phys. Rev. B **48**, 2515 (1993).
4. G. Pang and F. Pu, Phys. Rev. B **38**, 12649 (1988).
5. J. Yang and G. Pang, J. Magn. Magn. Mater. **87**, 157 (1994).
6. D. H. A. L. Anselmo, M. G. Cottam, and E. L. Albuquerque, J. Appl. Phys. **85**, 5774 (1999).
7. L. I. Deych, D. Zaslavsky, and A. A. Lisyansky, Phys. Rev. E **56**, 4780 (1997).
8. B. A. Van Tiggelen and A. Tip, J. Phys. I **1**, 1145 (1991).
9. A. R. McGurn, K. T. Christensen, F. M. Mueller, and A. A. Maradudin, Phys. Rev. B **47**, 13120 (1993).
10. M. M. Sigalas, C. M. Soukoulis, C.-T. Chan, and D. Turner, Phys. Rev. B **53**, 8340 (1996).
11. V. A. Ignatchenko, R. S. Iskhakov, and Yu. I. Mankov, J. Magn. Magn. Mater. **140–144**, 1947 (1995).
12. A. G. Fokin and T. D. Shermergor, Zh. Éksp. Teor. Fiz. **107**, 111 (1995) [JETP **80**, 58 (1995)].

13. A. V. Belinskiĭ, Usp. Fiz. Nauk **165**, 691 (1995) [Phys. Usp. **38**, 653 (1995)].
14. B. Kaelin and L. R. Johnson, J. Appl. Phys. **84**, 5451 (1998); J. Appl. Phys. **84**, 5458 (1998).
15. V. A. Ignatchenko and Yu. I. Mankov, Phys. Rev. B **56**, 194 (1997).
16. A. N. Malakhov, Zh. Éksp. Teor. Fiz. **30**, 884 (1956) [Sov. Phys. JETP **3**, 701 (1956)].
17. S. M. Rytov, *Introduction to Statistical Radiophysics*, 2nd ed. (Nauka, Moscow, 1976), Part 1.
18. V. A. Ignatchenko, Yu. I. Mankov, and A. V. Pozdnaykov, Zh. Éksp. Teor. Fiz. **116**, 1335 (1999) [JETP **89**, 717 (1999)].
19. V. A. Ignatchenko, Yu. I. Mankov, and A. A. Maradudin, Phys. Rev. B **59**, 42 (1999).
20. V. A. Ignatchenko, Yu. I. Mankov, and A. A. Maradudin, J. Phys.: Condens. Matter **11**, 2773 (1999).
21. V. A. Ignatchenko, A. A. Maradudin, and A. V. Pozdnaykov, Phys. Met. Metallogr. **91** (S1), 69 (2001).
22. V. A. Ignatchenko, Yu. I. Mankov, and A. A. Maradudin, Phys. Rev. B **62**, 2181 (2000).
23. V. A. Ignatchenko, Yu. I. Mankov, and A. A. Maradudin, Phys. Rev. B **65**, 024207 (2002).
24. R. C. Bourret, Nuovo Cimento **26**, 1 (1962); Can. J. Phys. **40**, 783 (1962).

JETP Letters, Vol. 77, No. 6, 2003, pp. 291–294. Translated from Pis'ma v Zhurnal Éksperimental'noĭ i Teoreticheskoĭ Fiziki, Vol. 77, No. 6, 2003, pp. 341–344.

Luminescence of Eu^{3+} Ions in Ultradisperse Diamond Powders

G. E. Malashkevich, V. A. Lapina, G. I. Semkova, P. P. Pershukevich, and G. P. Shevchenko

Institute of Molecular and Atomic Physics, National Academy of Sciences of Belarus, Minsk, 220072 Belarus
e-mail: malash@imaph.bas-net.by

Received February 10, 2003

The luminescence of Eu^{3+} ions implanted in ultradisperse diamond powders, activated by impregnating with a solution of $Eu(NO_3)_3 \cdot 6H_2O$ and heat-treated at various temperatures, is studied. A multiple increase in the efficiency of excitation in the charge-transfer band is observed for the $^5D_0$ state of Eu^{3+} ions as compared to europium nitrate heat-treated similarly. This effect is explained by an increase in the degree of Eu–O bond covalency and a change in the activator coordination polyhedron due to the formation of chemical bonds Eu–O–C. © *2003 MAIK "Nauka/Interperiodica".*

PACS numbers: 78.67.Bf; 78.55.-m

Ultradisperse diamond (UDD) powders obtained by detonation synthesis consist of nanoparticles that represent diamond nuclei with an average size of ~ 4 nm covered by a cluster shell of nondiamond carbon in the so-called "onionlike" form [1]. Inclusions of the graphite phase, which additionally contains various types of hydrocarbons and impurities [1, 2], are located on this shell. Such nanoparticles exhibit luminescence properties in the visible and near-UV spectral regions, whereas the band gap width of nondiamond carbon can decrease down to 2 eV as in the fraction of "graphite-like" sp^2 bonds increases with respect to "diamond-like" sp^3 bonds (the band gap width in single crystal diamond comprises 5.5 eV) [3, 4]. These features make UDD an interesting object for studying its effect on the spectral luminescence properties of rare-earth ions implanted in an onionlike shell. This work reports results of such an investigation with the use of Eu^{3+} ions as a spectroscopic probe.

Samples were prepared by mixing a dry UDD powder with a water–alcohol solution of $Eu(NO_3)_3 \cdot 6H_2O$ under conditions of ultrasonic dispersion, dried, and then successively annealed in air at different temperatures (T_{an}) for 30 min (the heating rate was 300 K/h). Luminescence spectra (LS) and luminescence excitation spectra (LES) were measured by the reflectance method on an SDL-2 spectrofluorimeter, corrected with regard to the spectral sensitivity of the detection system and the spectral density distribution of the exciting radiation according to [5], and plotted the number of quanta per unit wavelength interval $[dn(\lambda)/d\lambda]$ against the wavelength. All the spectral measurements were performed at T = 298 K. The decomposition of spectral bands into individual components and the determination of their barycenters were carried out by the procedures outlined in [6, 7].

Figure 1 shows the LS of a Eu-containing UDD powder (sample 1) annealed at different temperatures; the excitation wavelength λ_{exc} = 280 nm (curves *1*). LS of a $Eu(NO_3)_3 \cdot 6H_2O$ crystalline hydrate powder (sample 2) annealed and measured under identical conditions (curves *2*) are displayed in the same figure. Fragments of these spectra measured with a high resolution are given in insets. These spectra were normalized by reducing the maximum of the Eu^{3+} $^5D_0 \longrightarrow {}^7F_2$ band ($\lambda \sim 615$ nm) to unity; spectra in the insets were normalized to the maximum of the $^5D_0 \longrightarrow {}^7F_1$ band lying in the range 585–600 nm. It is evident that a long-wavelength shift of the barycenter of the nonsplit $^5D_0 \longrightarrow {}^7F_0$ band ($\lambda \sim 580$ nm) and a drastic change in the splitting pattern of $^5D_0 \longrightarrow {}^7F_2$ and $^5D_0 \longrightarrow {}^7F_4$ bands take place at T_{an} = 450°C for sample 1 as compared to sample 2 (Fig. 1a). An increase in T_{an} up to 700°C (Fig. 1b) leads to a significant narrowing of spectral bands, a change in their shapes, and the appearance of excessive components in the bands corresponding to the $^5D_0 \longrightarrow {}^7F_0$, $^7F_1$ transitions. At T_{an} = 1000°C (Fig. 1c), the difference between the spectra of the samples under comparison is essentially leveled.

Figure 2 shows the LES of the samples studied normalized to the maximum of the magnetic dipole $^7F_0 \longrightarrow {}^5D_1$ band ($\lambda \sim 530$ nm); the detection wavelength λ_{det} = 611 nm. It is evident that an approximately ninefold increase in the intensity of the broad band at λ = 250 nm, a decrease by a factor of 1.5 in the relative intensity of the $^7F_0 \longrightarrow {}^5L_6$ band ($\lambda \sim 395$ nm), and a

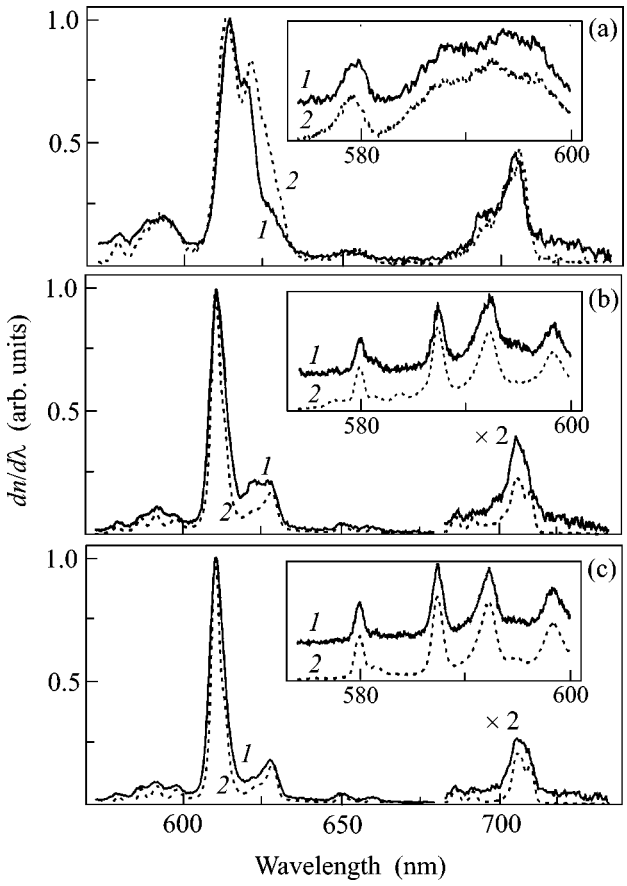

Fig. 1. Luminescence spectra of (*1*) Eu-containing UDD powder and (*2*) $Eu(NO_3)_3 \cdot 6H_2O$ crystalline hydrate annealed in air; λ_{exc} = 280 nm. The width of the detection line $\Delta\lambda_{det}$ = 2.6 nm and 0.2 nm (inset). $\Delta\lambda_{exc}$ = 2.6 nm and 0.3 nm (inset). T_{an}, °C: (a) 450, (b) 700, and (c) 1000.

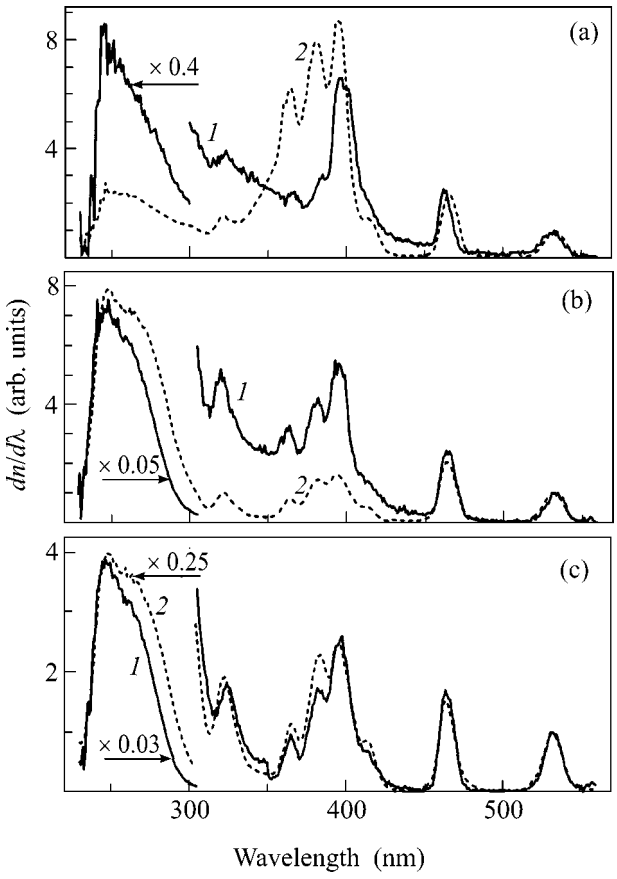

Fig. 2. Luminescence excitation spectra of (*1*) Eu-containing UDD powder and (*2*) $Eu(NO_3)_3 \cdot 6H_2O$ crystalline hydrate annealed in air; λ_{det} = 611 nm, $\Delta\lambda_{det}$ = 2 nm; T_{an}, °C: (a) 450, (b) 700, and (c) 1000.

multiple decrease in the relative intensity of the $^7F_0 \longrightarrow {}^5G_2$, $^5D_4$ bands ($\lambda \sim 382$ and 364 nm, respectively) take place at T_{an} = 450°C (Fig. 2a) for sample 1 (curve *1*) as compared to sample 2 (curve *2*). At T_{an} = 700°C (Fig. 2b), a significant and nonsimilar redistribution of the intensities of electric dipole *f–f* bands of the activator is observed in the spectra of both samples, and the excess of the intensity of the band at $\lambda \sim 250$ nm in curve *1* as compared to curve *2* approaches a twenty-fold one. At T = 1000°C (Fig. 2c), the intensity and shape of the *f–f* bands for the samples under comparison significantly approach each other, and the ratio of band intensities at $\lambda \sim 250$ nm decreases down to 8. The scanning of the monochromator slit with $\Delta\lambda_{det}$ = 2 nm over the $^5D_0 \longrightarrow {}^7F_2$ band at T_{an} = 450 and 1000°C weakly affects LES. The redistribution of the relative intensities and shape of the *f–f* bands for samples with T_{an} = 700°C with the same scanning is more significant; however, the efficiency of Eu^{3+} luminescence excitation in sample 1 at $\lambda \sim 250$ nm remains many times higher than in sample 2 in all the cases. Here it should be noted that, when the samples under comparison annealed at T_{an} = 450°C were held for many days in a wet atmosphere, the relative intensity of the broad short-wavelength band and the shape and intensity of the *f–f* bands become virtually identical in both LES and LS. At $T_{an} \geq$ 700°C, this effect was not observed.

In addition to the results described above, it is necessary to report that the color of the obtained powders of activated UDD changed in the following sequence: gray (T_{an} = 450°C), pink (T_{an} = 700°C), and light beige (T_{an} = 1000°C). It is also essential to note that the LS of the nonactivated UDD at λ_{exc} = 240 nm and T_{an} = 450°C is characterized by a broad ($\Delta\lambda \sim 250$ nm), weakly structured band with a maximum in the region of 500 nm. The corresponding LES weakly depends on λ_{det} and represents a band that reaches a significant intensity at $\lambda < 250$ nm, whereas its maximum lies beyond the limits of the short-wavelength boundary of the working region of the detection system ($\lambda \approx$ 215 nm).

According to [8], the complete dehydration of $Eu(NO_3)_3 \cdot 6H_2O$ crystalline hydrate and, possibly, the appearance of the phase of the $EuONO_3$ oxy salt take place at T_{an} = 450°C for the annealing regime used in this work. Judging from curves *1* and *2* in Fig. 1a, the optical Eu^{3+} centers forming in this case are characterized by low symmetry and large inhomogeneous broadening. A notable 0.5-nm (15-cm^{-1}) long-wavelength shift of the barycenter of the $^5D_0 \longrightarrow {}^7F_0$ band of Eu^{3+} ions in Fig. 1a and a significant weakening of the electric dipole Eu^{3+} *f–f* bands in Fig. 2a in going from sample 2 to sample 1 point to an increase on the average in the degree of Eu–O chemical bond covalency [9]. It is evident that the reason for this increase is associated with the interaction of Eu^{3+} and EuO^+ ions with the onion-like shell of UDD and with the residual acid groups located on its surface (carbonyl, carboxyl, etc. [2]) with the formation of Eu–O–C bonds. Actually, calculating the strength of a single chemical bond by the procedure [10] based on the use of the electronegativities of interacting elements, one can easily show that it comprises 1.94 and 1.80 relative units for the N–O and C–O bonds, respectively. This, according to the known rule of "polarization" and "counter polarization," leads to a weaker displacement of oxygen from europium in the Eu–O–C chain and to an increase in the degree of Eu–O bond covalency. Here, a significant increase in the splitting of the $^5D_0 \longrightarrow {}^7F_4$ band indicates, according to [11], a change in the shape of the activator coordination polyhedron. Apparently, it is these two facts that lead to a multiple increase in the intensity of the luminescence excitation band of Eu^{3+} ions in UDD with the shortest wavelength. Based on the similarity of this band for both samples and also on the absence of the analogous band in the LES of nonactivated UDD, it should be assigned to absorption in the $Eu^{3+} \longleftarrow O^{2-}$ charge-transfer band. It is not inconceivable that the efficiency of excitation in the $Eu^{3+} \longleftarrow O^{2-}$ band is even higher, because, judging from the gray color of sample 1, it is possible that this band is screened by the absorption of the UDD shell. As to the similarity between the LS and LES of the samples under comparison with T_{an} = 450°C after their hold in a wet atmosphere, it is appropriate to associate this similarity with the formation of basic europium salts due to the hydrolysis reaction.

At T_{an} = 700°C, anhydrous europium salts are transformed to oxy salts and, partially, to oxides [8]. This fact is reflected in the sharp decrease in the inhomogeneous broadening and, judging from the appearance of additional components in the region of $^5D_0 \longrightarrow {}^7F_0$, $^7F_1$ bands (see the inset in Fig. 1b), in the appearance of two types of Eu^{3+} optical centers in sample 1 and three or four types in sample 2. In addition, the degree of Eu–O bond covalency in the main type of centers in both sample 1 and sample 2 increases, whereas the distance between the barycenters of the corresponding nonsplit bands decreases down to 0.05 nm (1.5 cm^{-1}); however, according to the retaining of the $^5D_0 \longrightarrow {}^7F_4$ band splitting character, the activator coordination polyhedron retains its shape. It is evident that the significant increase for UDD in the efficiency of the excitation of the $^5D_0$ state in the $Eu^{3+} \longleftarrow O^{2-}$ charge-transfer band in this case can be explained by both an increase in the quantum yield of the intracomplex transfer of excitations and the weakening of luminescence quenching as a result of an increase in the band gap width of the onionlike shell due to the partial burning of amorphous carbon. According to the data from [12], the quantum yield indicated above increases as the charge-transfer absorption band shifts toward the short-wavelength side, which also occurs in our case: the barycenters of the $Eu^{3+} \longleftarrow O^{2-}$ bands in Figs. 2b and 2c for sample 1 shift with respect to the corresponding bands of sample 2 by 4.7 nm (690 cm^{-1}) and 3.9 nm (570 cm^{-1}), respectively. Simultaneously, this shift gives additional evidence of the increase in the degree of Eu–O bond covalency, because the energy of electron detachment from the ligand and electron transfer to the activator must increase in this case.

Significant leveling of the differences in spectra at T_{an} = 1000°C due to Eu^{3+} *f–f* transitions in the samples under comparison can be explained by the burning of the most part of amorphous carbon. It is notable that the differences in the LS of the samples under comparison are virtually absent already at T_{an} = 1100°C; however, the efficiency of luminescence excitation in the $Eu^{3+} \longleftarrow O^{2-}$ bands for UDD remains approximately seven times higher. Apparently, this is due to the retention of the Eu–O–C bonds, but at the expense of dangling surface bonds of the diamond cluster.

It may be believed that the multiple increase in the luminescence intensity of Eu^{3+} ions upon excitation in the charge-transfer band found in this work is of a universal character. This increase is associated with the chemical interaction of Eu^{3+} ions with the UDD surface and must be manifested in all cases when chemical bonds form between variable valence metals and carbon-containing nanoparticles.

We are grateful to ZAO "Sinta" (Minsk, Belarus) for presenting UDD samples.

REFERENCES

1. A. E. Aleksenskiĭ, M. V. Baĭdakova, A. Ya. Vul', and V. I. Siklitskiĭ, Fiz. Tverd. Tela (St. Petersburg) **41**, 740 (1999) [Phys. Solid State **41**, 668 (1999)].
2. A. V. Gubarevich, G. S. Akhremkova, and V. A. Lapina, Zh. Fiz. Khim. (in press).
3. M. E. Kompan, E. I. Terukov, S. K. Gordeev, *et al.*, Fiz. Tverd. Tela (St. Petersburg) **39**, 2156 (1997) [Phys. Solid State **39**, 1928 (1997)].
4. A. E. Aleksenskiĭ, V. Yu. Osipov, N. A. Kryukov, *et al.*, Pis'ma Zh. Tekh. Fiz. **23** (22), 39 (1997) [Tech. Phys. Lett. **23**, 874 (1997)].

5. C. A. Parker, *Photoluminescence of Solutions* (Elsevier, Amsterdam, 1968; Mir, Moscow, 1972).
6. L. G. Brazhnik and R. G. Zhbankov, Zh. Anal. Khim. **49**, 257 (1994).
7. B. I. Stepanov and V. P. Gribkovskiĭ, *Introduction to the Theory of Luminescence* (Akad. Nauk BSSR, Minsk, 1963).
8. *Chemistry of Rare-Earth Elements. Carbonates, Oxalates, Nitrates, Titanates*, Ed. by V. P. Orlovskiĭ and N. N. Chudinov (Nauka, Moscow, 1984).
9. M. I. Gaĭduk, V. F. Zolin, and L. S. Gaĭgerova, *Luminescence Spectra of Europium* (Nauka, Moscow, 1974).
10. N. N. Ermolenko, Steklo Sitally Silik. Mater., No. 5, 3 (1976).
11. V. S. Korol'kov and A. G. Makhanek, Zh. Prikl. Spektrosk. **48**, 975 (1988).
12. N. S. Poluéktov, N. P. Efryushina, and S. A. Gava, *Determination of Microquantities of Lanthanides from Luminescence of Crystallophosphors* (Naukova Dumka, Kiev, 1976).

Translated by A. Bagatur'yants

JETP Letters, Vol. 77, No. 6, 2003, pp. 295–299. Translated from Pis'ma v Zhurnal Éksperimental'noĭ i Teoreticheskoĭ Fiziki, Vol. 77, No. 6, 2003, pp. 345–349.

Spatial Correlations of Recombination Radiation Intensities of Two-Dimensional Electrons under the Conditions of the Quantum Hall Effect

M. V. Lebedev*, I. V. Kukushkin*, O. V. Volkov*, A. L. Parakhonskiĭ*, J. H. Smet, and K. von Klitzing****

** Institute of Solid-State Physics, Russian Academy of Sciences, Chernogolovka, Moscow region, 142432 Russia*

*** Max-Planck-Institut für Festkörperforschung, 70569 Stuttgart, Germany*

Received February 11, 2003

Correlations have been studied between the recombination radiation intensities of a two-dimensional electron gas measured at different points of the sample with giant luminescence fluctuations in the quantum Hall effect regime. It has been found that the correlation of the radiation intensities measured under these conditions at different points of the sample separated by a distance of 1–3 mm is close to unity and disappeared in a threshold way with increasing temperature. It is shown that macroscopic spatial correlations also disappear if the electron system is artificially divided into two subsystems not connected with each other. © *2003 MAIK "Nauka/Interperiodica".*

PACS numbers: 73.20.-r; 73.43.-f; 78.66.-w

1. Giant fluctuations that we observed previously in the luminescence intensity of a two-dimensional electron gas under the conditions of the quantum Hall effect [1] exhibit a number of completely unusual properties pointing to the fundamentality of the new phenomenon. Among these are the following properties: (a) the dispersion of radiation intensity fluctuations is anomalously high, (b) fluctuations are observed exclusively in the quantum Hall effect regime, (c) the range of magnetic fields at integer filling factors in which fluctuations can be observed is extremely narrow (less than 0.01 T), (d) fluctuations rapidly disappear as the temperature is raised above a critical one, and (e) the critical temperatures for even and odd filling factors are essentially different. The very possibility of observing giant intensity fluctuations in the radiation collected by a light guide from the surface of the sample about 1 mm in size already points to the existence of mechanisms in the system determining that recombination processes proceed consistently at macroscopic distances. The nature of these mechanisms is not clear at present; however, the necessity of studying spatial correlations in radiation fluctuations is evident. It is not inconceivable that luminescence intensity fluctuations are due to the effect of additional background illumination on the two-dimensional electron system. This background illumination serves to excite the luminescence signal, and although it creates a negligibly small concentration of electrons as compared to their dark concentration in the two-dimensional channel, it can nevertheless become significant because of an extremely fast variation of system parameters in the immediate vicinity of an integer filling factor. Another explanation is of a more fundamental character. It may be believed that the electron system undergoes a phase transition; that is, a new coherent macroscopic state of two-dimensional electrons described by a common wave function arises. In this case, the unity of wave function provides an exceptionally high degree of the uniformity of the concentration of electrons at macroscopic distances, which is manifested in the abnormally narrow peak of noise localized at an integer filling factor (the peak width at the filling factor scale is less than 0.001). In the case of this scenario, an analogue of the Josephson effect in the two-dimensional electron system in the quantum Hall effect regime and a manifestation of the phase of the common wave function of the coherent state should be sought. From the viewpoint of the theory of dynamic systems (see, for example, [2, 3]), it is appropriate to raise the question of whether the observed fluctuations are a random process or a manifestation of the deterministic chaos of the dynamic system with the phase space of a finite dimension. In the latter case, an effort can be made to determine the phase space dimension and to find the form of the strange attractor of the system. It is of course hardly probable that studies of this sort can unambiguously elucidate the microscopic reasons for the fluctuations; however, these can strongly help in constructing the theory of this phenomenon, because the phase space dimension is directly related to

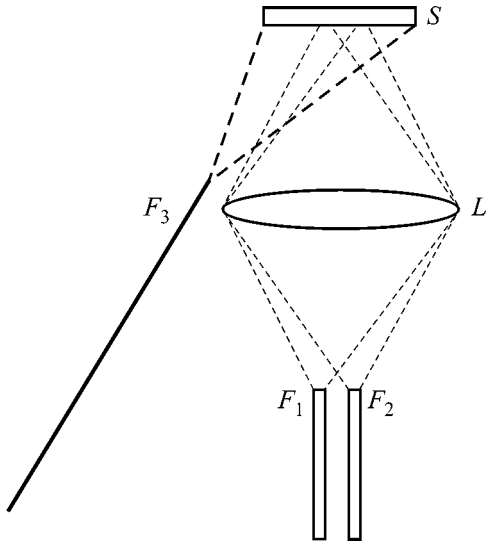

Fig. 1. Schematic diagram of the experiment.

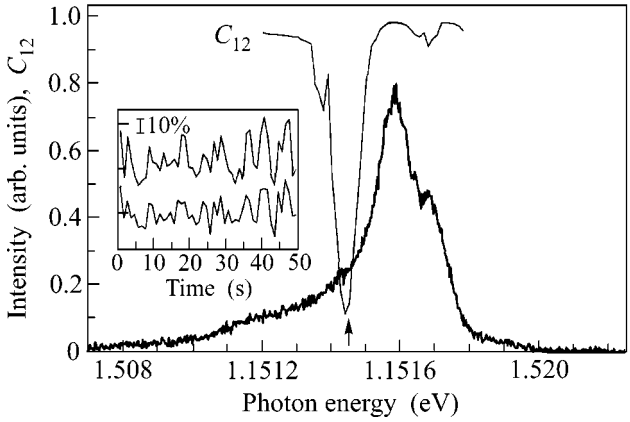

Fig. 2. Luminescence spectrum of two-dimensional electrons measured in a single quantum well with a width of 25 nm under conditions of the quantum Hall effect ($\nu = 2$, $n_s = 3.85 \times 10^{11}$ cm^{-2}, $B = 7.95$ T) at $T = 1.5$ K. Curve C_{12} corresponds to the spectral dependence of the correlation coefficient of luminescence intensities measured simultaneously in two different sections of the sample spaced at 1 mm (the inset shows time dependences of these luminescence signals). The arrow indicates the spectral position of the luminescence line from the GaAs buffer layer.

the number of independent differential equations describing the dynamic system. This work is devoted to a study of correlations between luminescent signals measured from two spatially separated regions of the sample surface under conditions of giant fluctuations of the radiation of two-dimensional electrons in the vicinity of the filling factor equal to 2. It is found that virtually complete correlation is observed for the radiation intensities measured at different points of the sample separated by a distance of 1–3 mm. It is shown that macroscopic spatial correlations disappear if the electron system is divided into two subsystems unconnected with each other.

2. Measurements were performed with high-quality samples containing a single GaAs quantum well, in which the radiative recombination of 2D electrons with photoexcited holes was studied. The samples were grown by molecular-beam epitaxy on a GaAs substrate by the following scheme: GaAs buffer layer 3000 Å thick, undoped GaAs/AlGaAs (30/100 Å) superlattice 13000 Å in total thickness, GaAs quantum well 250 Å thick, AlGaAs spacer 400 Å thick, and doped AlGaAs : Si layer (doping level, 10^{18} cm^{-3}) 650 Å thick. The characteristic mobility of 2D electrons in these structures at 3.8×10^{11} cm^{-2} was 1.3×10^6 cm^2 V^{-1} s^{-1}. The optical excitation of the sample was carried out by a laser light-emitting diode with a photon energy of 1.653 eV and the time instability of the radiation power less than 10^{-4}. A Monospec monochromator with a spectral resolution of 0.03 meV served as the spectral instrument. A semiconductor charge-coupled device (CCD) matrix was used for detecting the radiative recombination signal and for analyzing its intensity fluctuations. This allowed the entire luminescence spectrum to be measured simultaneously in the wavelength region of our interest. At the same time, the CCD matrix response speed (1 spectrum per minute) was quite sufficient for studying signal fluctuations, because the fluctuations at hand are predominantly of a low-frequency character with characteristic times on the order of tens of seconds. Sufficiently long sequences of spectra were recorded at a step of 1 s for studying the fluctuations. The characteristic duration of a series of spectra was 3000 s. The sample was placed in a helium cryostat inside a superconducting solenoid. The exciting radiation was delivered and the luminescence signals were collected using light guides as shown in Fig. 1. The radiation of the pumping laser was supplied to the sample through light guide F_3 0.4 mm in diameter, which gave a spot about 2–3 mm in diameter on the sample surface. Short-focus lens L constructed an image of the sample with a magnification close to unity in the plane where the ends of receiving light guides F_1 and F_2 were arranged. This symmetric optical scheme is the least critical with respect to the accuracy of the arrangement of the light guides and, therefore, minimizes the effect of misalignment, which inevitably arises on cooling to helium temperatures. The receiving light guides were 1 mm in diameter and were arranged right up to each other. As a result, we had the possibility of recording signals from two sections of the sample surface 1 mm in diameter each with distances between their centers of about 1.2 mm, which did not overlap with each other. The accurate alignment of the whole system was carried out in the following way. The sample was illumi-

nated through the receiving light guides and the lens using a filament lamp. A screen of thin white paper was placed on the surface of the sample, and the sample and the screen were transferred along the optical axis until a sharp image of light guide ends F_1 and F_2 appeared on the screen. As a result, we could be assured that the sections of the sample surface from which signals were recorded did not actually overlap.

3. Figure 2 demonstrates the luminescence spectrum measured in a single quantum well with a concentration of 2D electrons of 3.85×10^{11} cm^{-2} in a magnetic field of 7.95 T, which corresponds to a filling factor $\nu = 2.00$. It is important that under these conditions the radiative recombination spectra measured from two different points of the sample with the use of two light guides spaced at about 1 mm coincided. This fact indicates that a 2D-electron system under conditions of the integer quantum Hall effect becomes uniform and the local electron concentrations at different points of the sample coincide with a high accuracy. This result is in good agreement with the fact that anomalous radiation intensity fluctuations are observed within an extremely narrow range of magnetic fields in the vicinity of integer filling factors that corresponds to the change in the filling factor by less than 0.005. Measuring with the use of two light guides allowed us to record the time evolution of radiation spectra from different points of the sample simultaneously, because the signals from the light guides were detected simultaneously by two different sections of one CCD matrix. This allowed us to perform a quantitative comparison of the parameters of giant radiation intensity oscillations at different points of the sample and to study spatial correlation effects. With this purpose, we calculated the correlation coefficient (see, for example, [3]) between the radiation intensities (I_1 and I_2) measured simultaneously from two different light guides

$$C_{12} = \langle \Delta I_1 \Delta I_2 \rangle / (D_1 D_2)^{1/2},$$

where $\langle I_i \rangle$ is the average intensity over the whole measurement time and $\Delta I_i = I_i - \langle I_i \rangle$, $D_i = \langle \Delta I_i^2 \rangle$ is the variance of I_i. A comparison of the results measured from different light guides showed that giant intensity fluctuations are observed simultaneously in the same narrow range of magnetic fields in the vicinity of an integer value of the filling factor equal to 2 (and also in the vicinity of $\nu = 4, 6, 8$). Therefore, it was possible to measure the correlation coefficient of fluctuating signals and its dependence on the wavelength in the emission spectrum. A typical example of measurements of anomalous radiation intensity fluctuations carried out with the use of two light guides under conditions of the quantum Hall effect at a maximum of the luminescence line is shown in the inset in Fig. 2. It is evident that strong correlation (phase coherence) is observed under these conditions for fluctuations of the two intensities. The spectral dependence of the coefficient C_{12} under conditions when the filling factor equals 2 ($B = 7.95$ T) is shown in Fig. 2 (curve C_{12}). It is evident that the coefficient C_{12} is rather close to unity for all the wavelengths corresponding to the luminescence of the 2D electron gas and drops virtually to zero in the vicinity of 1514.66 meV, where the contribution of bulk luminescence from the GaAs buffer layer (shoulder in the luminescence spectrum marked by an arrow in Fig. 2) dominates. Note that we identified luminescence lines from bulk GaAs by an analysis of the behavior of these lines upon varying the magnetic field and the concentration of 2D electrons [4]. It is directly followed from Fig. 2 that sections of the two-dimensional electron system spaced at about 1 mm can emit light in a strongly correlated way.

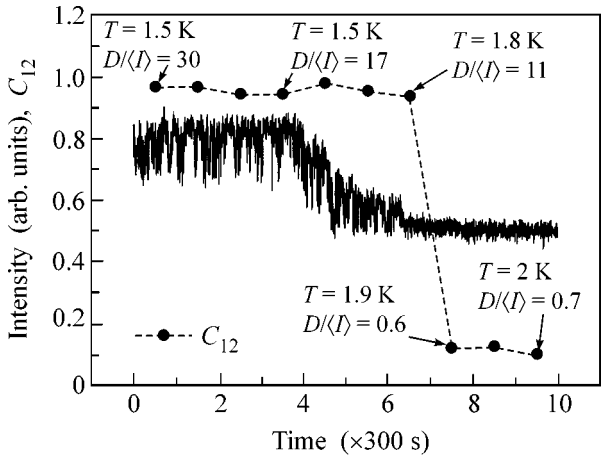

Fig. 3. Temperature dependence of the luminescence intensity measured at a maximum of the recombination line of two-dimensional electrons (1.516 eV) under conditions of the quantum Hall effect ($\nu = 2$, $n_s = 3.85 \times 10^{11}$ cm^{-2}, $B = 7.95$ T) at $T = 1.5$ K. Points in the figure indicate how the correlation coefficient C_{12} of two radiative recombination intensities of two-dimensional electrons measured simultaneously at two spatially distant points of the sample. The value of the ratio $D/\langle I \rangle$ is indicated for each point.

Tracing the temperature dependence of the correlation coefficient is of interest. We measured giant fluctuations under conditions when all the macroscopic parameters were fixed with the greatest possible accuracy and the temperature varied slowly with time. The results of the corresponding measurements are shown in Fig. 3. As the temperature increases, the luminescence signal somewhat decreases; however, it is more important that giant fluctuations disappear with increasing T. This is reflected in Fig. 3, where it is shown how the luminescence intensity measured at the line maximum (1.516 eV) varies. In addition, it is indicated in the same figure how the ratio $D/\langle I \rangle$ varies with temperature. In is evident that the ratio $D/\langle I \rangle$ takes an anomalously high value of about 30 at 1.5 K and sharply drops down to normal Poisson values (0.5–1) at $T > 1.9$ K. As to the correlation coefficient, it is evident

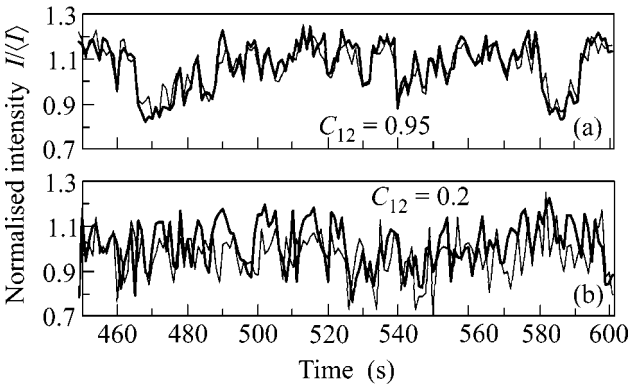

Fig. 4. Comparison of giant fluctuations of luminescence intensities measured under the same experimental conditions (a) without and (b) with a strip dividing the system of two-dimensional electrons into two subsystems. It is evident that dividing the sample into two subsystems completely suppresses the effect of correlations between luminescence intensity fluctuations and decreases the correlation coefficient from 0.95 down to 0.2. Measurements were performed under conditions of the quantum Hall effect at $\nu = 2$, $n_s = 3.85 \times 10^{11}$ cm^{-2}, $B = 7.95$ T, and $T = 1.5$ K.

in the figure that it remains close to unity down to the critical temperature $T_c = 1.9$ K, at which giant fluctuations disappear, and then sharply drops down to its background value (less than 0.1). Thus, it may be argued that the occurrence of spatial correlations of luminescence signals at macroscopic distances is a characteristic feature of the regime of giant fluctuations under conditions of the integer quantum Hall effect at $T < T_c$.

In order to check whether the existence of a common excitation spot is essential for the observed correlations, the following experiment was set up. A thin strip (0.5 mm) of black paper was placed on the sample so that it divided the excitation spot into two parts and the signal arrived at each of the light guides from its own part of the excitation spot. It should be noted that the signals from the same two parts of the sample measured in the absence of the black strip at $\nu = 2$ exhibited in-phase giant fluctuations with a correlation coefficient of 0.95. In the presence of the black strip correlations between the signals were not observed even at $\nu = 2$, though the signal from each light guide still exhibited giant fluctuations (ratio $D/\langle I\rangle > 10$). The results obtained under the same experimental conditions with the dividing strip and without it are compared in Figs. 4a and 4b, respectively. It is evident that dividing the sample into two subsystems completely suppresses the effect of correlations between luminescence intensity fluctuations. Small residual correlations that are seen in Fig. 4b can be explained by insufficient magnetic field stability, because these correlations were observed even in the absence of giant intensity fluctuations. It is known that the magnetic field strongly affects the shape of the luminescence spectrum of a 2D electron gas, especially under conditions of the quantum Hall effect [4, 5]. By virtue of this fact, the insufficient stability of the field can give rise to residual correlations of the signals. In the case when the luminescence spectrum only weakly depends on the field strength, as takes place for bulk luminescence, the magnitude of residual correlations is close to zero. The suppression of correlations in intensity fluctuations observed in this work on artificially dividing the 2D electron system into two subsystems allows us to exclude unambiguously the possible interpretation of giant fluctuation according to which the fluctuations are due to the anomalous enhancement of instabilities of the magnetic field or the photoexcitation source. Actually, it is possible to suggest that, because of the sharp stepwise character of the magnetic-field dependence of the spectral position of the luminescence line in the vicinity of integer filling factors [1], even weak magnetic field fluctuations can be manifested under these conditions as a strong instability of the luminescence intensity. If this were so, it would be reasonable to expect in-phase fluctuations in both parts of the sample upon dividing the 2D electron system into two subsystems (with the use of a thin black strip), because the source of fluctuations is similar in both cases and specifies a common phase. However, it is evident in Fig. 4 that correlations in intensity fluctuations disappear upon dividing the electron system into two subsystems, which most likely points to the occurrence of a common single phase in the macroscopic wave function of 2D electrons under conditions of the quantum Hall effect. Upon artificially dividing the electron system into two subsystems, the unity of the wave function disappears and a phase difference appears between the wave functions of two subsystems, which leads to disturbance of the phase coherence of fluctuations measured in different parts of the sample. The occurrence of a phase difference in the wave functions must lead to phenomena analogous to the Josephson effect. Therefore, it may be expected that oscillations associated with phase periodicity must arise in the correlation coefficient C_{12} if the parameters of the barrier (its width and the potential height) dividing the electron system into two subsystems are smoothly varied.

Thus, correlations between recombination radiation intensities of a 2D electron gas measured at different points of the sample with giant luminescence fluctuations in the regime of the quantum Hall effect have been investigated in this work. It has been found that extremely strong correlations are observed in intensity fluctuations under these conditions. These correlations most likely point to the macroscopic coherence of the electron system in the regime of the quantum Hall effect. It has been shown that these correlations disappear as the temperature increases or if the electron system is artificially divided into two subsystems unconnected with each other.

This work was supported by the Russian Foundation for Basic Research and by the program Physics of Solid-State Nanostructures.

REFERENCES

1. O. V. Volkov, I. V. Kukushkin, M. V. Lebedev, *et al.*, Pis'ma Zh. Éksp. Teor. Fiz. **71**, 558 (2000) [JETP Lett. **71**, 383 (2000)].
2. H. G. Schuster, *Deterministic Chaos* (Physik, Weinheim, 1984; Mir, Moscow, 1988).
3. L. Mandel and E. Wolf, *Optical Coherence and Quantum Optics* (Cambridge Univ. Press, Cambridge, 1995; Nauka, Moscow, 2000).
4. O. V. Volkov, V. E. Zhitomirskiĭ, I. V. Kukushkin, *et al.*, Pis'ma Zh. Éksp. Teor. Fiz. **65**, 38 (1997) [JETP Lett. **65**, 38 (1997)].
5. O. V. Volkov, V. E. Zhitomirskiĭ, I. V. Kukushkin, *et al.*, Pis'ma Zh. Éksp. Teor. Fiz. **66**, 539 (1997) [JETP Lett. **66**, 575 (1997)].

Translated by A. Bagatur'yants

JETP Letters, Vol. 77, No. 6, 2003, pp. 300–304. Translated from Pis'ma v Zhurnal Éksperimental'noĭ i Teoreticheskoĭ Fiziki, Vol. 77, No. 6, 2003, pp. 350–355.

Parametric Generation of Solitonlike Spin-Wave Pulses in Ring Resonators Based on Ferromagnetic Films

A. A. Serga*, [1], M. P. Kostylev, B. A. Kalinikos**, S. O. Demokritov*, B. Hillebrands*, and H. Benner*****

** Department of Physics, Kaiserslautern University of Technology, 67663 Kaiserslautem, Germany*
*** St. Petersburg State Electrotechnical University, St. Petersburg, 197376 Russia*
e-mail: borisk@borisk.usr.etu.spb.ru
**** Darmstadt University of Technology, D-64289 Darmstadt, Germany*
Received February 11, 2003

Parametric generation of intense solitonlike spin-wave pulses is experimentally observed in ring resonators based on ferromagnetic films under the effect of a periodic parallel pulsed magnetic pumping. Depending on the repetition rate of the pumping pulses and the position of their carrier frequency about the eigenfrequency spectrum of the ring resonator, different types of nonlinear pulse sequences are obtained. The theoretical explanation of this phenomenon is proposed. *© 2003 MAIK "Nauka/Interperiodica".*

PACS numbers: 75.30.Ds; 75.70.-i; 85.70.Ge

It is well known that, in nonlinear dispersion media, the excitation and propagation of nonlinear pulses in the form of envelope solitons is possible (see, e.g., [1, 2]). Recently, the use of "active rings" constructed on the basis of nonlinear dispersion waveguide media was proposed for the self-generation of envelope solitons. For example, active rings on the basis of ferromagnetic films were used for the self-generation of both bright and dark microwave magnetic envelope solitons [3–6]. In such rings, an external microwave amplifier connected in series with the ferromagnetic film served to compensate for the losses associated with the spin wave and other ring elements. The compensation of the losses could cause the ring, which actually was a travelling wave resonator, to operate in the multifrequency self-generation regime with a discrete spectrum of generated frequencies. With active resonant rings, two different mechanisms of the stationary spin-wave soliton self-generation were realized. These mechanisms were based on the time [3] and frequency [4–6] filtering of the circulating signal. Thus, previous studies showed that active resonant rings fabricated on the basis of ferromagnetic films can be used for an effective self-generation of periodic sequences of spin wave envelope solitons.

The purpose of this work is the experimental investigation of the possibility of obtaining a parametric generation of periodic sequences of nonlinear spin-wave pulses in a ring resonator by using a spatially localized parallel pulsed magnetic pumping. In contrast to the previous studies of the spin-wave soliton generation in rings, in our experiments the loss in the resonant ring was compensated by the "internal" mechanism of parametric amplification of spin waves.

The mechanism of parametric amplification of spin-wave pulses, including nonlinear solitonlike pulses, by a spatially localized parallel pumping was investigated in [7–16]. In particular, in the previous studies, it was shown that, for the realization of a parametric amplification of both linear and nonlinear spin-wave pulses (bright solitons), the most convenient objects are the so-called backward volume magnetostatic waves (BVMSWs) propagating along the direction of a bias magnetic field in a tangentially magnetized ferromagnetic film. The gain factors obtained experimentally for a short BVMSW pulse in the pulsed pumping regime exceed 30 dB [13].

In addition, it was shown that the parametric amplification of BVMSWs by means of a parallel pulsed pumping by a spatially localized microwave magnetic field has some distinctive features that distinguish it from the amplification of a spin-wave signal by a conventional microwave amplifier. Such features are the comparable gain values for a multitude of parametrically amplified thickness modes and the formation of counter- and copropagating idle pulses that occur simultaneously with the amplification of the signal pulse.

In the experiments, we used an active resonant ring whose basic elements were a tangentially magnetized yttrium iron garnet (YIG) film, a microwave amplifier, and an attenuator. A backward volume magnetostatic wave was used as the "carrier" wave. It should be noted that the microwave amplifier mainly served for the

[1] Permanent address: Radio Physics Faculty, Shevchenko National University, Kiev, 01033 Ukraine.

compensation of the matching losses in the antennas used for the excitation and reception of spin waves in the film. We stress that the amplifier parameters (the amplified frequency band and the dynamic range) were chosen so that the nonlinear properties of the resonant ring were determined solely by the YIG film. The attenuator served for a smooth attenuation control in the ring.

The experiments were performed on a narrow YIG film strip, 1.5 mm wide, which served as a "waveguide" for spin waves. The waveguide was cut out of a single-crystal film grown on a gadolinium gallium garnet substrate with the (111) orientation; the film thickness was $L = 4.9$ μm. To excite and receive the spin waves, a conventional delay line structure was used [17, 18], which had short-circuited input and output microstrip antennas 50 μm wide. The distance between the input and output microstrip antennas was equal to 8 mm. The pumping element was placed in the middle between the input and output antennas. It was made of a wire 50 μm in diameter, in the form of a half-wave resonator tuned to a frequency of 14.518 GHz.

Experiments on the parametric generation of solitonlike pulses formed by the lowest thickness mode of the BVMSW were performed in several steps. At the first step, with the interrupted feedback circuit, the amplitude–frequency characteristic (AFC) of the spin-wave delay line was measured in a definitely linear regime by supplying a continuous external signal to its input. The resulting AFC is shown in Fig. 1a. One can see that, at the operating frequency, the transmission loss of the microwave signal in the structure was about 45 dB. A simple calculation (based on the known half-power ferromagnetic resonance linewidth of the film $\Delta H = 0.4$ Oe) shows that the net value of the BVMSW transmission loss in the structure was about 11 dB. This means that the main contribution to the total loss was made by the signal conversion in the antennas (of about 34 dB).

In addition to the loss measurement, an external signal supplied to the disconnected ring was used to measure the gain in the spin-wave pulse due to the parallel pumping. The maximal internal (i.e., without regard for the signal conversion loss in the antennas) gain factor was 13 dB. This result showed that, in the parallel pumping regime, the given experimental structure allows a complete compensation of the BVMSW pulse transmission loss but provides no compensation of the loss in the antennas. In the experiment, the latter was achieved using a microwave amplifier.

At the second stage of the experiment, the ring was closed and the gain in the feedback circuit was chosen so as to compensate the conversion loss in the antennas without allowing the system to switch to the spontaneous self-generation mode. In these conditions, an external monochromatic signal was supplied to the delay line input, and the AFC of the structure was again measured in the transmission configuration. Figure 1b shows the AFC part lying in the region near the frequency chosen as the operating one for the following measurements. As one would expect in the case of a ring resonator, the measured AFC is characterized by a set of narrow resonance peaks. The distance between the peaks (3.2 MHz) corresponds to the propagation distance of spin waves in the YIG film. Simple calculations using the theoretical value of the spin wave group velocity and the distance between the antennas showed that the delay time of the microwave signal in the feedback circuit was only 5 ns out of the whole time of signal circulation in the ring $t_1 = 315$ ns.

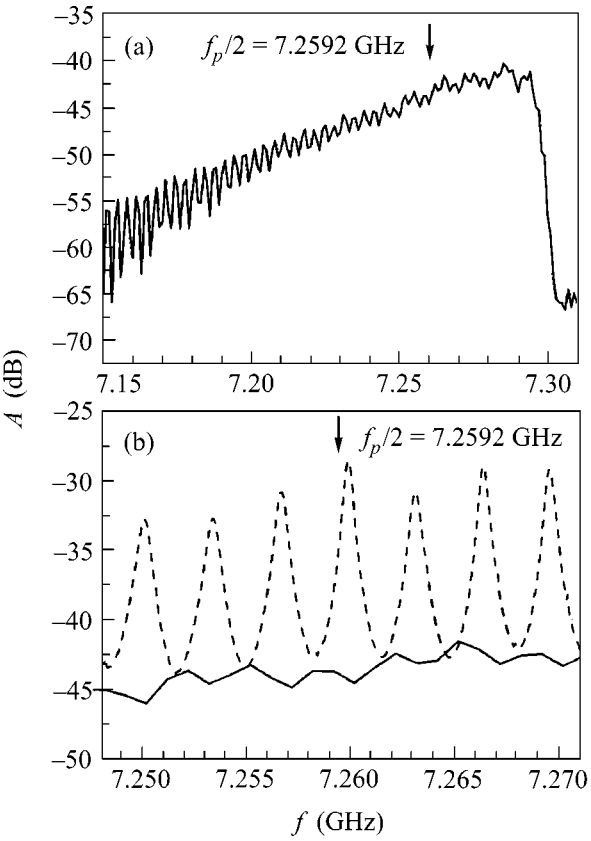

Fig. 1. (a) Amplitude–frequency characteristic (AFC) of a disconnected ring and (b) the working part of the AFC (the solid lines). The dashed line in the lower plot (b) shows the working part of the AFC measured for a closed ring with a microwave amplifier gain of 43 dB in the absence of pulsed pumping. The arrow indicates the position of half the carrier frequency of the pumping pulses.

Then, a periodic sequence of short rectangular microwave pulses was supplied to the input of the pumped element. The pulse duration was 24 ns, and the period T_p was chosen to be equal to the period of signal circulation in the ring: $T_p = t_r = 315$ ns. The pumping carrier frequency was $f_p = 14.518$ GHz. By varying the bias magnetic field, the half pumping frequency $f_p/2$ was placed within the long-wavelength part of the BVMSW spectrum. (In Fig. 1, the position of one-half the pumping frequency $f_p/2$ with respect to the AFC of

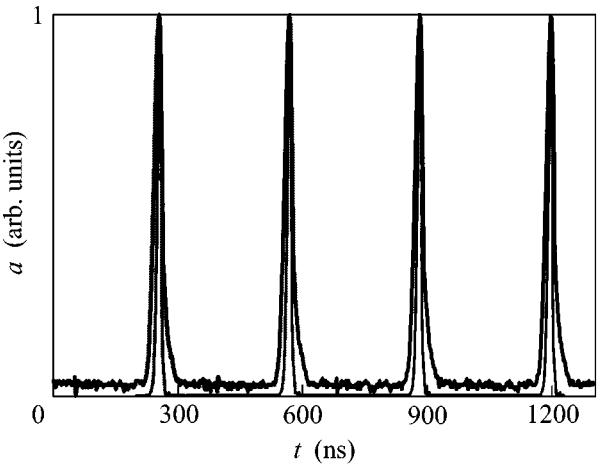

Fig. 2. Profile of a parametrically generated sequence of spin-wave pulses. The thick line represents the experiment, and the thin line, the numerical calculation. The YIG film thickness is 4.9 μm, the distance between the input and output antennas is 8 mm, the microstrip resonator width is 50 μm, the bias magnetic field is 1852 Oe, the duration of a pumping pulse is 24 ns, and the pumping pulse repetition period is 315 ns.

the structure is shown by a vertical arrow.) The power of the pumping pulses was chosen so as to exceed the threshold of the pulsed parametric generation of spin waves in the ring.

The measurements showed that a stable parametric generation of short spin wave pulses is observed in a very narrow interval of the pumping pulse repetition period values. At the same time, it was found that the pumping carrier frequency, at which the effective parametric generation of nonlinear solitonlike pulses is observed, can be easily varied. Such a tuning was of a discrete character, and the tuning step, i.e., the distance between the neighboring frequencies at which the effective parametric generation of nonlinear solitonlike pulses took place, was equal to 1.59 MHz. In other words, the carrier frequency of the generated pulses (which was determined by us as one-half the pumping carrier frequency $f_p/2$) could be easily varied at a step of 1.59 MHz. A typical profile of the pulse sequence generated in our experiment is shown in Fig. 2 by the thick line. The profile was obtained at the pumping frequency $f_p = 14.518$ GHz with a bias magnetic field of 1852 Oe.

The last stage of measurements was the study of different generation regimes that occurred with the variation of the pumping pulse repetition period. We obtained single-pulse and two-pulse generation regimes. As was mentioned above, a single-pulse generation was observed when the pumping pulse repetition period was equal to the time of the signal circulation in the ring (see Fig. 2). The two-pulse generation was observed when the pumping pulse repetition period was equal to half the time of pulse circulation in the ring. Typical periodic pulse sequences observed in these two generation regimes are shown in Fig. 3. Note that, in the case of a stationary generation, a small variation of the pumping pulse repetition period (of about 10 ns) suppressed the generation.

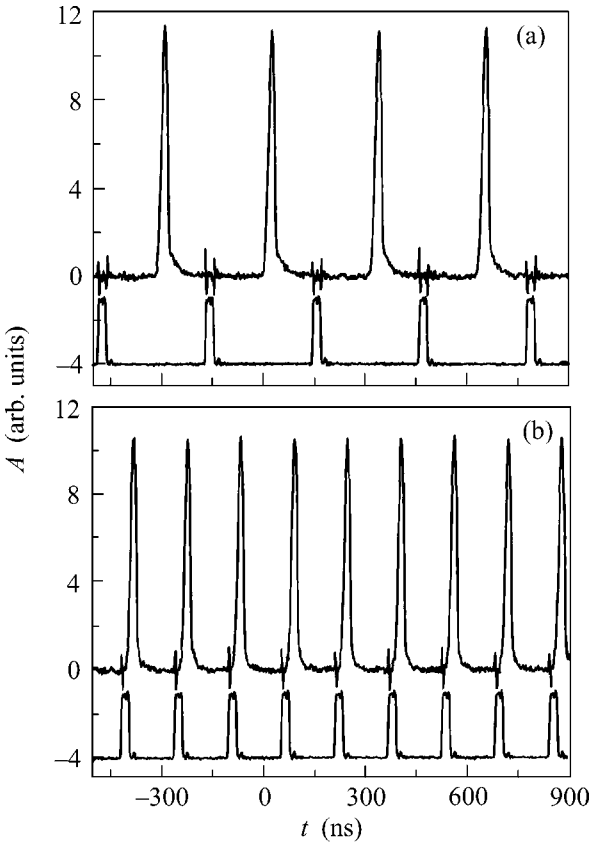

Fig. 3. Experimental profiles of the envelope of the generated periodic pulse sequence. (a) Repetition period of the pumping pulses is equal to the period of spin-wave pulse circulation, i.e., $T_p = t_r = 315$ ns; in this case, one spin-wave pulse circulates in the ring. (b) The repetition period of the pumping pulses is equal to half of the period of spin-wave pulse circulation, i.e., $T_p = t_r/2 = 155$ ns; in this case, two spin-wave pulses circulate in the ring.

To explain the experimental results, we performed analytical calculations and a numerical modeling of the experiment. The model was constructed using the following simplifying assumptions: the ring was assumed to be homogeneous with respect to the wave propagation, and the ring properties, including the transmission loss per unit distance, were described as if they were completely determined by the ferromagnetic film in which the BVMSW propagates. We stress that the model takes into account the spatially localized parametric amplification of only the lowest thickness mode of the BVMSW. To obtain a unidirectional circulation, for the idle pulse we set a much greater transmission loss (compared to the natural one for YIG) in the time intervals within which the pumping was turned off. As a result, the parametrically generated backward idle

pulse was completely suppressed until its next collision with the amplified pulse.

The modeling was performed on the basis of the system of nonlinear parametric equations proposed in our previous publication [14]. The equations were obtained for the spatial Fourier components of the alternating magnetization of the BVMSW and the pumping microwave field. In the present paper, these equations are modified for the case of a periodic ring structure by introducing a discrete wave number with the step $\Delta k = 2\pi/l$, where l is the length of the ring film resonator. The equations take into account the three-wave parametric interaction of the microwave magnetic field of the pulsed periodic parallel pumping with the BVMSW packet, the four-wave process of the wave self-action in the wave packet, and the dispersion of the BVMSW. Note that, in the equations for the spatial Fourier components of the dynamic magnetization, we use the real spectrum of traveling BVMSWs in the ferromagnetic film, $\omega(k)$, but with a discrete wave number k.

An example of the numerical calculation performed for a single-pulse generation regime is shown in Fig. 2 by the thin line. The calculation shows that, when the pumping pulse repetition frequency is equal to the signal circulation frequency in the ring, a spin wave pulse arises starting from the noise level and then rapidly grows in amplitude. Owing to the large value of the parametric gain, the shape of the generated pulse observed immediately after the pumping is turned off is mainly determined by the duration of the pumping pulse, the spatial length of the pumping region, and the phase relations in the ring. As the pulse travels through the ring, the pulse shape is slightly smoothed by dispersion. When the amplitude of the generated pulses approaches the threshold of the nonlinear four-wave self-action, i.e., the single-soliton threshold,[2] a broadening of the spectrum of spatial and, hence, temporal harmonics of the wave packet takes place. As a result, harmonics lying outside the pumping spectral band are generated. These harmonics do not participate in the amplification process and, hence, are strongly attenuated. The persistent energy transfer to these harmonics owing to the four-wave self-action process is enhanced with growing amplitude of the wave packet envelope; thus, it raises the resulting loss level in the system and, finally, limits further amplitude growth. The results of the numerical modeling suggest that, although the pulses generated in a stationary regime do not have the shape of a single envelope soliton, they are formed according to the soliton mechanism. This process is characteristic of our wave system, in which the dispersion and the nonlinear coefficients have different signs.

Now, let us consider the interpretation of the periodicity observed in the positions of the generation frequency bands (when the half pumping frequency varies

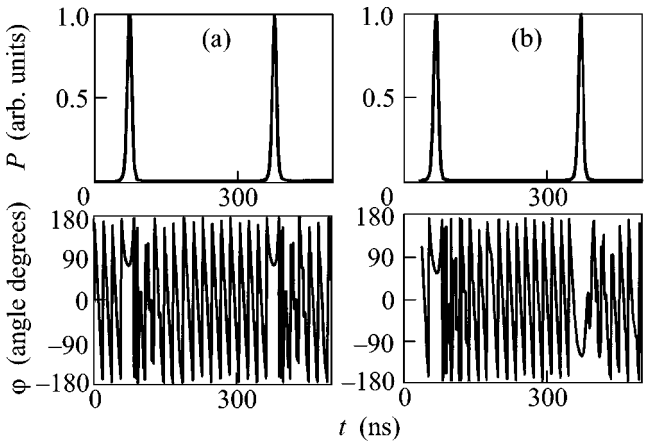

Fig. 4. Calculated profiles of the instantaneous power and the phase of the envelope of the parametrically generated pulse sequence: (a) half the pumping frequency is equal to 7261 MHz, which corresponds to the 15th resonance mode of the ring; (b) half the pumping frequency is equal to 7259.4 MHz, which corresponds to the middle point between the 14th and 15th resonance modes of the ring. Other parameters are the same as in Fig. 2.

at a step of 1.59 MHz). To explain this effect, we performed numerical modeling for two cases. The results of the calculations are shown in Fig. 4. Figure 4a corresponds to the case (same as in Fig. 2) when one-half the pumping frequency exactly coincides with the frequency of one of the resonance modes of the ring (the 15th mode in the given specific case), and Fig. 4b, to the case when half the pumping frequency lies exactly in the middle between the 14th and 15th modes (i.e., 1.59 MHz upwards from the 15th mode). The upper curves in Fig. 4 show the power profiles of the pulses, and the lower curves, their phase profiles.

The calculation shows that an effective generation of pulse sequences is possible in both cases. The amplitude profiles of the generated pulse sequences fully coincide. However, their phase profiles exhibit some difference. In case (a), all pulses of the sequence are in phase, whereas in case (b), the phase changes from pulse to pulse by 180°.

This effect has the following physical explanation. The periodic pulsed pumping with the pulse repetition frequency equal to the frequency of signal circulation in the ring, 3.18 MHz, possesses a discrete frequency spectrum, and the harmonics of this spectrum are spaced at 3.18 MHz. This means that the parametric pumping spectrum measured at half the frequency (the frequency of the parametric amplification of spin waves) consists of harmonics spaced at 1.59 MHz. Then, it is only every second pumping harmonic that may coincide with an eigenfrequency of the ring resonator and, hence, make an effective contribution to the parametric amplification of the circulating wave packet. The spectrum of the periodic sequence of rectangular rf pulses is known to have the maximal har-

[2] Modeling shows that, for a given duration of the pumping pulses, the single-soliton threshold is 1–2 degrees when measured in terms of the precession angle of the local magnetic moment.

monic at the pulse carrier frequency (in our case, f_p). As the pumping carrier frequency is sequentially shifted by 3.18 MHz, one-half the frequency f_p of this maximal harmonic sequentially coincides with either an eigenfrequency of the ring or a middle point between eigenfrequencies. In the first case, the maximal gain due to the parametric pumping corresponds to only one eigenfrequency of the resonant ring, and this frequency becomes the carrier frequency of the parametrically generated pulse sequence. In the second case, the maximal parametric gain corresponds to two eigenfrequencies of the resonant ring, and precisely these two frequencies prove to be the initial frequencies of the parametrically generated pulse sequence. Thus, in this case, we have a sequence of antiphase pulses with the suppressed central carrier frequency (Fig. 4b).[3] Similar conclusions follow from the numerical Fourier transformation, which yields the frequency spectra of pulse sequences shown in Fig. 4.

Of interest is to consider the analogy between the results obtained by us and the theoretical predictions [20] that follow from the analytic solutions of the boundary-value problems for a one-dimensional nonlinear Schrödinger equation. In particular, in the cited paper [20] it was shown that, for periodic boundary conditions modeling a nonlinear dispersion ring, two types of nonlinear solutions are possible. One of these types of nonlinear solutions ("bright soliton trains") exhibits an analogy with the ordinary linear solutions to the Schrödinger equation. The second type has no analogy with linear solutions and is unique in this sense. In [20], the latter type of solutions was called symmetry breaking solution. Using the terminology of [20] for describing the results of our study, we can say that Fig. 4b shows the nonlinear sequences maintaining the symmetry, and Fig. 4a, the symmetry breaking sequences. Thus, the nonlinear system under study, in which the stationary state is determined by not only four-wave but also three-wave parametric interactions, is another type of a system that allows the existence of nonlinear stationary states of two internally different types.

In closing, we note that we obtained and studied the parametric generation of intense solitonlike spin waves under the effect of a periodic pulsed parallel magnetic pumping in ring resonators made on the basis of ferromagnetic films. Depending on the pumping pulse repetition period and the position of the pumping pulse repetition frequency with respect to the resonator eigenfrequency spectrum, we observed the generation of different types of sequences. We proposed a theoretical explanation of the phenomenon under investigation on the basis of the numerical solution of a system of nonlinear equations with allowance for the three-wave and four-wave interactions and the spectral features of spin waves in a ferromagnetic film. It was found that the limitation of the amplitude growth for a parametrically amplified pulse circulating in the film resonator and the formation of the stationary profile of this pulse follow the soliton mechanism.

More detailed experimental data and their comparison with theory will be published elsewhere.

This work was supported by the Russian Foundation for Basic Research (project no. 02-02-16485), the German Scientific Society (Deutsche Forschungsgemeinschaft, project no. DFG 436 RUS 113/644/0-1), and INTAS (project no. 99-812).

REFERENCES

1. M. Remoissenet, *Waves Called Solitons: Concepts and Experiments* (Springer, Berlin, 1996).
2. G. P. Agrawal, *Nonlinear Fiber Optics* (Academic, San Diego, 1995; Mir, Moscow, 1996).
3. B. A. Kalinikos, N. G. Kovshikov, and C. E. Patton, Phys. Rev. Lett. **80**, 4301 (1998).
4. B. A. Kalinikos, M. M. Scott, and C. E. Patton, Phys. Rev. Lett. **84**, 4697 (2000).
5. M. M. Scott, B. A. Kalinikos, and C. E. Patton, Appl. Phys. Lett. **78**, 970 (2001).
6. B. A. Kalinikos, N. G. Kovshikov, M. P. Kostylev, and H. Benner, Pis'ma Zh. Éksp. Teor. Fiz. **76**, 310 (2002) [JETP Lett. **76**, 253 (2002)].
7. G. A. Melkov and S. V. Sholom, Zh. Tekh. Fiz. **60** (8), 118 (1990) [Sov. Phys. Tech. Phys. **35**, 943 (1990)].
8. B. A. Kalinikos and M. P. Kostylev, IEEE Trans. Magn. **33**, 3445 (1997).
9. B. A. Kalinikos, M. P. Kostylev, N. G. Kovshikov, *et al.*, Pis'ma Zh. Éksp. Teor. Fiz. **66**, 346 (1997) [JETP Lett. **66**, 371 (1997)].
10. A. V. Bagada, G. A. Melkov, A. A. Serga, and A. N. Slavin, Phys. Rev. Lett. **79**, 2137 (1997).
11. P. A. Kolodin, P. Kabos, C. E. Patton, *et al.*, Phys. Rev. Lett. **80**, 1976 (1998).
12. G. A. Melkov, A. A. Serga, V. S. Tiberkevich, *et al.*, IEEE Trans. Magn. **35**, 3137 (1999).
13. G. A. Melkov, A. A. Serga, A. N. Slavin, *et al.*, Zh. Éksp. Teor. Fiz. **116**, 2192 (1999) [JETP **89**, 1189 (1999)].
14. M. P. Kostylev and B. A. Kalinikos, Zh. Tekh. Fiz. **70**, 136 (2000) [Tech. Phys. **45**, 277 (2000)].
15. G. A. Melkov, Yu. V. Kobljanskyj, A. A. Serga, *et al.*, J. Appl. Phys. **89**, 6689 (2001).
16. G. A. Melkov, A. A. Serga, V. S. Tiberkevich, *et al.*, Phys. Rev. E **63**, 066607 (2001).
17. B. A. Kalinikos, N. G. Kovshikov, and A. N. Slavin, Zh. Éksp. Teor. Fiz. **94** (2), 1459 (1988) [Sov. Phys. JETP **67**, 303 (1988)].
18. M. Chen, M. A. Tsankov, J. M. Nash, and C. E. Patton, Phys. Rev. B **49**, 12773 (1994).
19. B. A. Kalinikos, M. P. Kostylev, N. G. Kovshikov, and H. Benner, IEEE Trans. Magn. **38**, 3120 (2002).
20. L. D. Carr, C. W. Clark, and W. P. Reinchardt, Phys. Rev. A **62**, 063611 (2000).

[3] Note that, here, one can easily see an analogy with the results of our previous work [19].

Translated by E. Golyamina

JETP Letters, Vol. 77, No. 6, 2003, pp. 305–310. Translated from Pis'ma v Zhurnal Éksperimental'noĭ i Teoreticheskoĭ Fiziki, Vol. 77, No. 6, 2003, pp. 356–361.

Stripe-like Topological Excitations in a Two-Dimensional Heisenberg Ferromagnet

E. V. Sinitsin, I. G. Bostrem, and A. S. Ovchinnikov

Ural State University, Yekaterinburg, 620083 Russia

e-mail: alexander.ovchinnikov@usu.ru

Received February 12, 2003

For a two-dimensional Heisenberg ferromagnet, a class of steady-state nonlinear excitations above the ground state is considered. The excitations have the form of stripes and exhibit quasiparticle properties. The effect of an external magnetic field on the basic characteristics of these nonlinear topological excitations is investigated. The magnetic field is found to destroy the instanton-type solutions (kinks) and to generate new particles with the properties of vortex–antivortex pairs: each particle has a zero topological charge and an energy close to the double skyrmion energy $8\pi JS^2$. The dispersion of the quasiparticles and the dependences of their energy and momentum on the number of magnons localized by one excitation are discussed. © *2003 MAIK "Nauka/Interperiodica".*

PACS numbers: 75.10.Hk; 75.30.Kz

Soliton solutions obtained for a two-dimensional ferromagnet remain the object of intensive research in physics of low-dimensional systems until this day. The study of nonlinear spin structures in the continuum approximation leads to a wide variety of configurations, whose ordering depends on the dimension and symmetry of the problem [1].

To obtain topological solitons, the usual way is to consider the mapping of a sphere, the physical space of the spin order parameter, onto a sphere homeomorphic to the *xy* plane. The resulting solutions, which include skyrmions [2], easy-axis solitons [3], out-of-plane vortices [4], etc., along with the recent helical [5] and nodal [6] solutions, naturally acquire a preferred axis and possess a preferred point in the plane. However, a two-dimensional plane also allows another compactification, in the form of a cylinder (Fig. 1), which brings up the question as to the mapping of a physical sphere S^2 on the manifold $R \times S^1$. In this case, one may obtain qualitatively new steady-state solutions with a preferred line. From symmetry considerations, it follows that these solutions must possess certain interesting properties, such as a nonzero momentum along the preferred line, a particular topological charge, and so on.

In this paper, we show that the aforementioned nonlinear excitations form a separate class of soliton solutions and can be obtained explicitly with allowance for the spatial symmetry. In addition, these nonlinear excitations have some properties that are characteristic of bound vortex–antivortex (skyrmion–antiskyrmion) pairs [7, 8]. However, unlike the latter, they represent indivisible stripelike spin structures with zero topological charge; i.e., they cannot be represented as a bound state of two topological particles with opposite charges. It is possible that, in the numerical studies of a number of magnetic systems [9, 10], the authors dealt with this kind of excitation rather than with the skyrmion–antiskyrmion pairs.

Consider a conventional Hamiltonian for a planar ferromagnet:

$$H = -\frac{1}{2}\sum_{i,\delta} J^{\perp}_{i,i+\delta}\mathbf{S}^{\perp}_i\mathbf{S}^{\perp}_{i+\delta} - \frac{1}{2}\sum_{i,\delta} J^{z}_{i,i+\delta}S^z_iS^z_{i+\delta} - h\sum_i S^z_i, \quad (1)$$

where $J^{\perp} > 0$ and $J^z > 0$ are the exchange integrals for the in-plane and *z* components, respectively, of the *i*th spin and its nearest neighbors lying at a distance δ from it; the last term describes the interaction with the external magnetic field *h* directed along the *z* axis.

To simplify the study in the long-wave length approximation, we use the continuum version of the spin equations of motion, which are expressed in terms of the variables θ and ϕ and correspond to Hamiltonian (1):

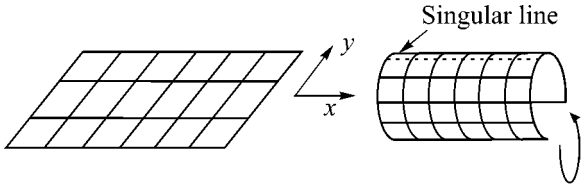

Fig. 1. Homeomorphic transformation of a two-dimensional plane into a cylinder.

0021-3640/03/7706-0305$24.00

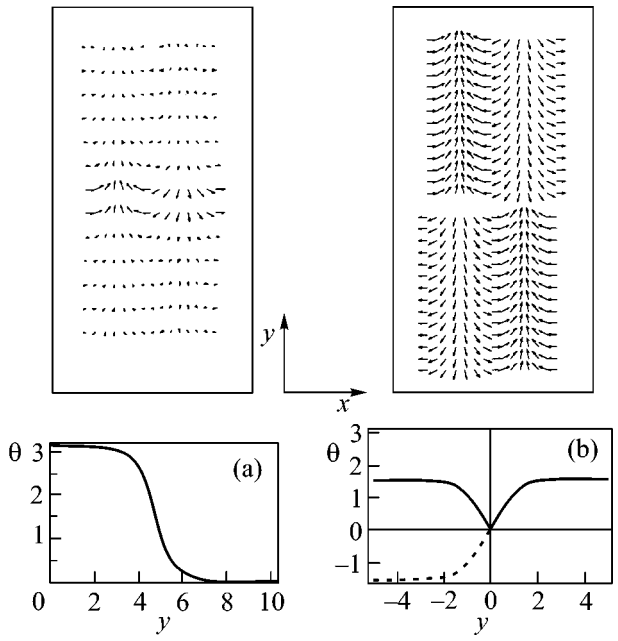

Fig. 2. Spin configurations of nonlinear topological excitations in the absence of magnetic field: (a) kinks and (b) out-of-plane solitons.

$$\hbar S\sin\theta\frac{\partial\phi}{\partial t} = J^{\perp}S^2(4\cos\theta\sin\theta + \cos^2\theta\Delta\theta) - J^{\perp}S^2\cos\theta\sin\theta((\nabla\theta)^2 + (\nabla\phi)^2) - 4J^zS^2\cos\theta\sin\theta + J^zS^2\cos\theta\sin\theta(\nabla\theta)^2 + J^zS^2\sin^2\theta\Delta\theta - hS\sin\theta, \quad (2)$$

$$-\hbar S\frac{\partial\theta}{t} = J^{\perp}S^2(\sin\theta\Delta\phi + 2\cos\theta(\nabla\theta\nabla\phi)). \quad (3)$$

To obtain a vertical stripe ordering, we use the parametrization $\theta = \theta(y)$, $\phi = \phi(x)$. Then, from Eq. (3), we derive $\phi = qx + \phi_0$, where q describes the period along the x axis that is matched with the stripe width L_x: $q = 2\pi/L_x$; outside the stripe, the value of ϕ coincides with ϕ_0, which is an arbitrary initial value. Note that the choice of a piecewise continuous function for the azimuth variable ϕ does not violate its harmonic behavior in the plane as a whole. For steady-state solutions tending to one of the possible ferromagnetic ordered states characterized by an angle $\theta = \theta_0$ when $y \longrightarrow +\infty$, Eq. (2) can be resolved as follows:

$$\left(\frac{d\theta}{dy}\right)^2 = \frac{\left(q^2 + 4\frac{K}{J}\right)(\sin^2\theta - \sin^2\theta_0) - 2\frac{h}{JS}(\cos\theta - \cos\theta_0)}{1 + \frac{K}{J}\sin^2\theta}, \quad (4)$$

where $K = J^z - J^{\perp}$ and $J = J^{\perp}$. The boundary value θ_0 is determined from Eq. (2): $\sin\theta_0(4K\cos\theta_0 + Jq^2\cos\theta_0 + h/S) = 0$, which yields the solutions (i) $\theta_0 = 0, \pi$ (below, we consider only $\theta_0 = 0$ for $h > 0$) and (ii) $\cos\theta_0 = -(h/JS)(q^2 + 4K/J)^{-1}$.

For the case $K = 0$ and $h = 0$, only the first type of the boundary conditions fits expression (4). Then, we arrive at a solution similatr to a topological kink in a one-dimensional system: $\theta = 2\tan^{-1}[\exp(-q(y - y_0))]$, where y_0 is an unessential constant representing the coordinate of the kink center. For an exchange anisotropy of the easy-axis type with $K > 0$, the solution $\theta = \theta(y)$ can be expressed in an implicit form:

$$\sqrt{q^2 + 4K/J}(y - y_0) = \frac{1}{2}\log\left[\frac{\sqrt{1 + K/J\sin^2\theta} + \cos\theta}{\sqrt{1 + K/J\sin^2\theta} - \cos\theta}\right] + \sqrt{K/J}\arcsin[\sqrt{K/(J + K)}\cos\theta]. \quad (5)$$

Similar expressions can be obtained for an easy-plane anisotropy with $K < 0$. However, in the latter case, two different solutions are possible (Fig. 2): (a) kinks corresponding to the boundary value $\theta_0 = 0$, which are realized when $|K/J| < q^2/4$, and (b) out-of-plane (OP) solitons with the boundary value $\theta_0 = \pi/2$, which appear when $|K/J| > q^2/4$. Solution (a) for the polar variable $\theta = \theta(y)$ has the following inexplicit form:

$$\sqrt{q^2 + 4K/J}(y - y_0) = \frac{1}{2}\log\left[\frac{\sqrt{1 + K/J\sin^2\theta} + \cos\theta}{\sqrt{1 + K/J\sin^2\theta} - \cos\theta}\right] - \sqrt{-K/J}\log[\sqrt{-K/J}\cos\theta + \sqrt{1 + K/J\sin^2\theta}]. \quad (6)$$

Solution (b), or the OP solution, is obtained in a similar way:

$$\pm\sqrt{4|K/J| - q^2}(y - y_0) = \sqrt{|K/J|}\arcsin(\sqrt{|K/J|}\sin\theta) + \sqrt{1 - |K/J|}\arctan\left(\frac{\sqrt{1 - |K/J|}\sin\theta}{\sqrt{1 - |K/J|\sin^2\theta}}\right). \quad (7)$$

The spin structure of the OP type exhibits an interesting effect, namely, the presence of an antiphase boundary extending along the x axis (Fig. 2b). A smooth monotonic variation of the angle θ in the form of a kink is possible only in the nonphysical range from $-\pi/2$ to $\pi/2$ if the plus sign is chosen in Eq. (7), or in the range from $3\pi/2$ to $\pi/2$ in the case of the minus sign. However, at the point y_0, where $\theta(y_0) = 0(\pi)$, the planar spin component $S^{\perp}$ changes sign, which makes this structure energetically unprofitable. To retain the same spin value above and below the kink center y_0 and to provide the energy gain, we use the global rotation in the upper half-plane $\varphi \longrightarrow \varphi + \pi$ while remaining within the

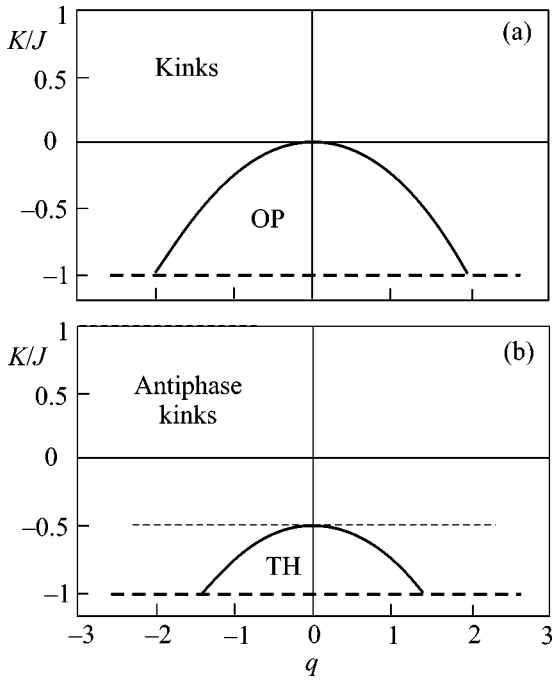

Fig. 3. Phase diagram of nonlinear excitations (a) with and (b) without a magnetic field.

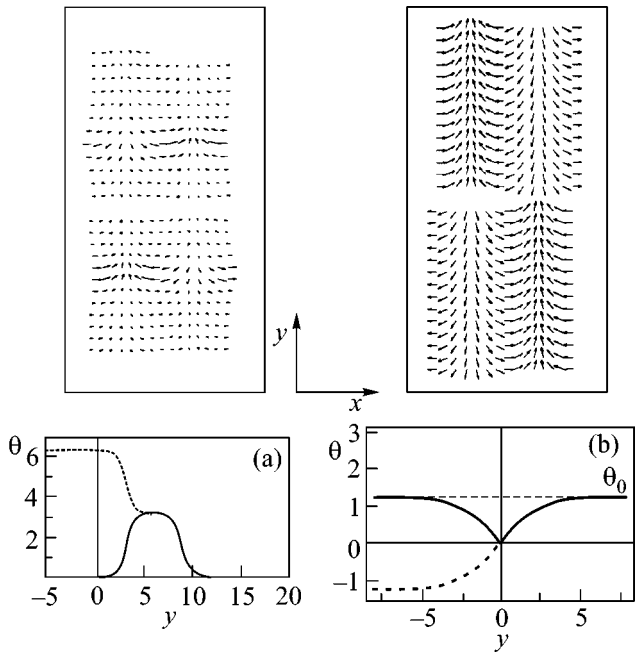

Fig. 4. Spin configurations of nonlinear excitations in the presence of a magnetic field: (a) antiphase kinks and (b) Takeno–Homma solitons.

physical range of variation of the angle $\theta \in [0, \pi]$. This explains the appearance of the antiphase boundary. The topological charge

$$Q = \frac{1}{4\pi}\int\int \sin\theta(y)d\theta(y)d\varphi(x)$$

determined for an individual stripe is equal to unity for kinks and to zero for OP solitons.

The phase diagram of the model is shown in Fig. 3a. Above the curve, one can see a vast region corresponding to kinks.

Let us consider the effect of an external magnetic field h. The solution for the isotropic case ($K = 0$) with the boundary value $\theta_0 = 0$ is

$$\exp\left(-2\sqrt{q^2 + \frac{h}{JS}}(y - y_0)\right) = \frac{(1 - \cos(\theta/2))}{(1 + \cos(\theta/2))}$$
$$\times \frac{\left(\frac{h}{JS} - q^2\cos\left(\frac{\theta}{2}\right) + \sqrt{\frac{h}{JS} + q^2}\sqrt{\frac{h}{JS} + q^2\cos^2\left(\frac{\theta}{2}\right)}\right)}{\left(\frac{h}{JS} + q^2\cos\left(\frac{\theta}{2}\right) + \sqrt{\frac{h}{JS} + q^2}\sqrt{\frac{h}{JS} + q^2\cos^2\left(\frac{\theta}{2}\right)}\right)}. \quad (8)$$

It has the form of a kink in the range from 0 to 2π and exhibits an antiphase boundary accompanied by the global rotation $\varphi \longrightarrow \varphi + \pi$ above the point y_0, at which $\theta(y_0) = \pi$. Correspondingly, the soliton profile is transformed to a "cap" shape (Fig. 4a). The topological charge is $Q = 0$. The analysis with allowance for both the exchange anisotropy and the external magnetic field shows that the region above the curve $q^2 + 4K/J + h/JS = 0$ corresponds to antiphase kinks with the characteristic length $L_y = (q^2 + 4K/J + h/JS)^{-1/2}$ along the y axis (Fig. 4a). The region below this curve belongs to solitons (we call them Takeno–Homma solitons (TH) [11]), which correspond to the boundary value $\cos\theta_0 = -(h/JS)(q^2 + 4K/J)^{-1}$ and describe the in-plane spin ordering with the antiphase boundary (Fig. 4b). They are analogues of the OP solitons, and their topological charge is also zero. As the field increases further, a soliton is reduced to the homogeneous state. This occurs when the field reaches the critical value $h_c = -4SK$.

When the magnetic field h is turned on, the phase diagram becomes somewhat modified (Fig. 3b). The curve separating the region of the topological excitations in the form of antiphase kinks from the region of TH solitons is shifted downwards by $h/4JS$, so that the TH soliton region is displaced to the point $K/J = -1$. For the fields above some critical value h_c, the formation of TH solitons is impossible.

The dynamics of a planar ferromagnet is restricted by the conservation laws that are also valid for topological solutions [12]. To proceed with our consideration, we use the following conserved quantities: the energy E, the momentum $\mathbf{P}$, and the number of localized magnons N.

We represent the energy functional in the form

$$E = -\iint dxdy(2J^{\perp}S^2\sin^2\theta + 2J^zS^2\cos^2\theta) + \frac{1}{2}\iint dxdy J^{\perp}S^2q^2\sin^2\theta - hS\iint dxdy\cos\theta + \frac{1}{2}\iint dxdy\left(J^{\perp}S^2\cos^2\theta\left(\frac{d\theta}{dy}\right)^2 + J^zS^2\sin^2\theta\left(\frac{d\theta}{dy}\right)^2\right), \quad (9)$$

where the first term corresponds to the exchange interactions; the second term is similar in form to a single-ion anisotropy of the easy-axis type; and the third and fourth terms describe the Zeeman component and the gradient contribution, respectively. The appearance of the preferred value $q = \sqrt{4|K/J| - h/JS}$ (the curve in the phase diagram) results from the competition of two tendencies: the dominant in-plane exchange ($K < 0$) and the "one-ion anisotropy."

The energy of one stripe $E = E_{bg} + \Delta E$ contains the term proportional to the stripe area σ_{str},

$$E_{bg} = \frac{JS^2}{2}[-4(1 + K/J) + (q^2 + 4K/J)\sin^2\theta_0 - 2(h/JS)\cos\theta_0]\sigma_{str} \quad (10)$$

(we call it the background energy, which, in the general case, differs from the energy of the nontopological ground state), and the additional energy

$$\Delta E = JS^2L_x\int dy[(q^2 + 4K/J)(\sin^2\theta - \sin^2\theta_0) - 2(h/JS)(\cos\theta - \cos\theta_0)], \quad (11)$$

which is determined by the deviation of the polar angle θ from its background value θ_0. Unlike E_{bg}, this correction remains finite for an individual stripe.

The direct calculation of these quantities for soliton solutions in the absence of the field,

$$E = -2J_zS^2\sigma_{str} + JS^2L_x\sqrt{q^2 + 4K/J} \times\left(1 + \frac{1 + K/J}{\sqrt{K/J}}\arcsin\sqrt{\frac{K/J}{1 + K/J}}\right) \text{(kink)} \quad (12)$$

and

$$E = -\frac{JS^2}{2}(4 - q^2)\sigma_{str} + JS^2L_x\sqrt{-q^2 + 4|K/J|} \times\left(\sqrt{1 - |K/J|} + \frac{\arcsin\sqrt{|K/J|}}{\sqrt{|K/J|}}\right) \text{(OP)}, \quad (13)$$

shows that the topological excitations can be separated into two types. Excitations of the first type (kinks in the case under consideration) lie immediately above the ground state when $K > 0$, and one can expect that, in certain conditions, these excitations will possess quasiparticle properties whose contribution to the thermodynamic properties may be considerable. By contrast, the solitons belonging to the second type are excited above the spin configuration, which is not a ground state (in our case, the OP solitons and the kinks in the case of $K < 0$). This principle holds when the magnetic field is taken into account. A simple analysis shows that the antiphase kinks lie above the state with the energy $E_{bg} = -(2J_zS^2 + hS)\sigma_{str}$, which is the ground state in the case of a small anisotropy $|K| < h/4S$; i.e., in the phase diagram, they lie above the dotted line (Fig. 3b). When $h < 4|K|S$, both antiphase kinks and TH solitons are excited above the background spin configurations, which do not correspond to minimal energy.

Let us discuss in more detail the quasiparticle properties of the solitons belonging to the first type. First, we note that common kinks in zero magnetic field represent instanton-type solutions that connect two equivalent vacuum states, spin-up and spin-down, at $y = \pm\infty$. Therefore, we consider only the antiphase kinks that have well defined integrals of motion, the momentum expressed as

$$\mathbf{P} = \hbar S\int_0^{L_x} dx\int_{-\infty}^{\infty} dy(1 - \cos\theta)\nabla\varphi,$$

and the total number of magnons localized by one excitation:

$$N = S\int_0^{L_x} dx\int_{-\infty}^{\infty} dy(1 - \cos\theta).$$

We consider most closely the case of an isotropic ferromagnet with $h \neq 0$. An antiphase kink has the energy $E = (-2J_zS^2 - hS)\sigma_{area} + \Delta E$ with

$$\Delta E = 4JS^2L_x \times\left(\sqrt{h/JS + q^2} + \frac{h}{qJS}\log\left[\frac{q + \sqrt{h/JS + q^2}}{\sqrt{h/JS}}\right]\right), \quad (14)$$

which is measured from the ground state energy at $h > 4|K|S$. For a soliton, the nonzero x component of the momentum

$$\mathbf{P} = \hbar S\int_0^{L_x} dx\int_{-\infty}^{\infty} dy(1 - \cos\theta)\nabla\varphi$$

has the form

$$P_x = 4\hbar SL_x\log\left[\frac{q + \sqrt{h/JS + q^2}}{\sqrt{h/JS}}\right], \quad (15)$$

which determines the dispersion $\Delta E = \Delta E(P_x)$, namely, $\Delta E = 4JS^2L_x\sqrt{h/JS + q^2} + h(P_x/\hbar q)$. In addition, the nonzero value of momentum provides an opportunity for a dynamical stabilization of a soliton [13]. Taking into account the relation $P_x = \hbar qN$, one can consider stripelike excitations as quasiparticles with an elementary momentum $\hbar q$. The dependence $E = E(N)$ also exhibits a linear behavior for large N; i.e., each quasiparticle makes an independent contribution to the energy. The angular momentum of such a stripe soliton,

$$M_z = \hbar qS\int_0^{L_x} dx \int_{-\infty}^{\infty} dyy(1-\cos\theta)$$

is zero. The dependences obtained by us (Fig. 5) can be qualitatively explained without difficulties. An increase in the stripe width $L_x = 2\pi/q$ along the x axis is accompanied by its compression along the y axis according to the formula $L_y = \sqrt{q^2 + h/JS}$, down to the minimal value determined by the magnetic field. A further growth of L_x leads to an increase in both the number of magnons localized by a soliton and the soliton energy. The soliton momentum P_x tends to a constant value, because the increase in L_x is compensated by a decrease in the elementary momentum $\hbar q$. The quasiparticle energy tends to $8\pi JS^2$ when $h \longrightarrow 0$ and $q \longrightarrow 0$. The appearance of an antiphase kink with the topological charge $Q = 0$ in the case of $h \neq 0$ can be interpreted as the generation of a quasiparticle by the external magnetic field. The properties of this quasiparticle are shown in Fig. 5 for a nonzero value of K and $h > 4|K|S$. It should be noted that the quasiparticle energy is close to the energy of the skyrmion–antiskyrmion pair production. Such particles were used in the semiclassical description of neutral excitations in a ferromagnet with the quantum Hall effect [8]. From the point of view of the theory developed by us, the appearance of a single antiphase kink with the topological charge $Q = 0$ may be misinterpreted as the generation of a vortex–antivortex pair, i.e., a pair of two coupled topological particles with opposite charges and a skyrmion energy of $4\pi JS^2$ per particle.

Thus, we have presented a theory of stripelike topological excitations in a two-dimensional Heisenberg ferromagnet. We considered the effect of an external magnetic field on the properties of topological excitations. We have found quasiparticle excitations immediately above the ground state for both easy-axis and easy-plane anisotropies. We have shown that the external magnetic field breaks the instanton-type solutions and generates new particles (antiphase kinks) with an energy close to the double skyrmion energy $8\pi JS^2$.

We are grateful to Professor M.V. Sadovskiĭ for discussing the results of this study. The work was supported in part by the Civilian Research and Development Foundation (project no. NREC-005), the INTAS (project no. 01-0654) (A.S.O.), and the program "Russian Universities" (project no. UR.01.01.005) (I.G.B. and A.S.O.).

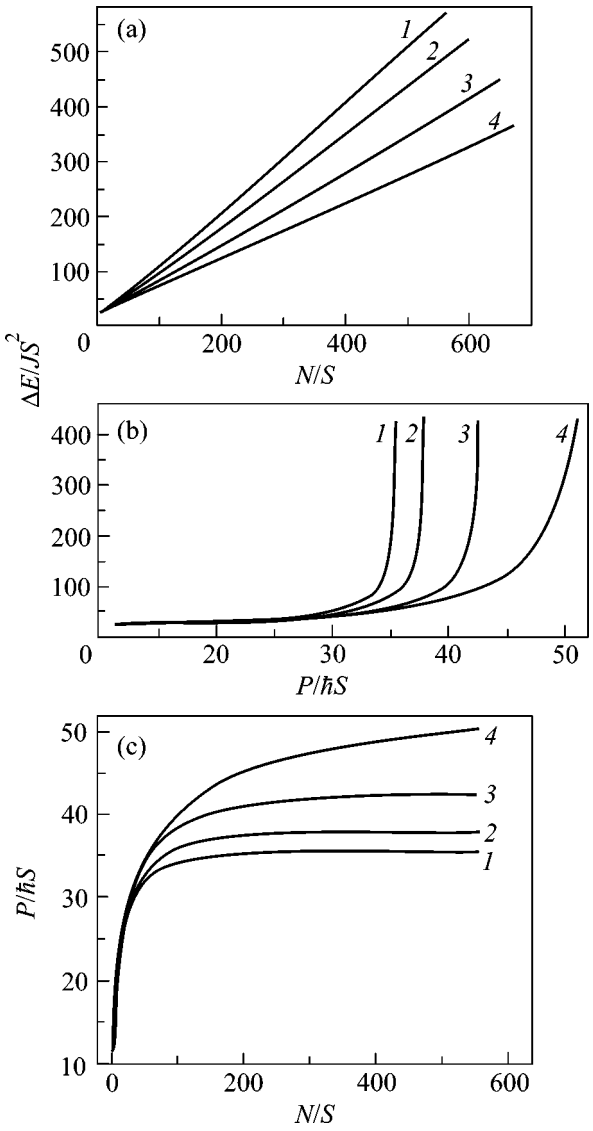

Fig. 5. Variations in the dependences (a) $E(N)$, (b) $E(P)$, and (c) $P(N)$ with varying ratio K/J: (*1*) 0.0, (*2*) –0.05, (*3*) –0.1, and (*4*) –0.125. The value of h/JS is taken to be equal to 0.5.

REFERENCES

1. A. M. Kosevich, B. A. Ivanov, and A. S. Kovalev, Phys. Rep. **194**, 119 (1990).
2. A. A. Belavin and A. M. Polyakov, Pis'ma Zh. Éksp. Teor. Fiz. **22**, 503 (1975) [JETP Lett. **22**, 245 (1975)].
3. A. S. Kovalev, A. M. Kosevich, and K. V. Maslov, Pis'ma Zh. Éksp. Teor. Fiz. **30**, 321 (1979) [JETP Lett. **30**, 296 (1979)].

4. M. E. Gouvea, G. M. Wysin, A. R. Bishop, and F. G. Mertens, Phys. Rev. B **39**, 11840 (1989).
5. A. B. Borisov, Pis'ma Zh. Éksp. Teor. Fiz. **73**, 279 (2001) [JETP Lett. **73**, 242 (2001)].
6. I. G. Bostrem and A. S. Ovchinnikov, Pis'ma Zh. Éksp. Teor. Fiz. **76**, 846 (2002) [JETP Lett. **76**, 716 (2002)].
7. A. S. Kovalev, S. Komineas, and F. G. Mertens, Eur. Phys. J. B **25**, 89 (2002).
8. S. L. Sondhi, A. Karlhede, S. A. Kivelson, and E. H. Rezayi, Phys. Rev. B **47**, 16419 (1993).
9. N. R. Cooper, Phys. Rev. Lett. **80**, 4554 (1998).
10. N. Papanicolaou and P. N. Spathis, Nonlinearity **12**, 285 (1999).
11. S. Takeno and S. Homma, Prog. Theor. Phys. **65**, 172 (1981).
12. R. F. Egorov, I. G. Bostrem, and A. S. Ovchinnikov, Phys. Lett. A **292**, 325 (2002).
13. B. A. Ivanov, C. E. Zaspel, and I. A. Yastremsky, Phys. Rev. B **63**, 134413 (2001).

Translated by E. Golyamina

JETP Letters, Vol. 77, No. 6, 2003, pp. 311–316. From Pis'ma v Zhurnal Éksperimental'noĭ i Teoreticheskoĭ Fiziki, Vol. 77, No. 6, 2003, pp. 362–367.

Anomalous Spin–Orbit Effects in a Strained InGaAs/InP Quantum Well Structure¶

S. A. Studenikin*, P. T. Coleridge, P. Poole, and A. Sachrajda

Institute for Microstructural Sciences, National Research Council of Canada, Ottawa, Ontario, K1A OR6, Canada

**e-mail: sergei.studenikin@nrc.ca*

Received February 3, 2003; in final form, February 13, 2003

There is currently a large effort to explore spin–orbit effects in semiconductor structures with the ultimate goal of manipulating electron spins with gates. A search for materials with large spin–orbit coupling is therefore important. We report results of a study of spin–orbit effects in a strained InGaAs/InP quantum well. The spin–orbit relaxation time, determined from the weak antilocalization effect, was found to depend nonmonotonically on gate voltage. The spin–orbit scattering rate had a maximum value of 5×10^{10} s^{-1} at an electron density of $n = 3 \times 10^{15}$ m^{-2}. The scattering rate decreased from this for both increasing and decreasing densities. The smallest measured value was approximately 10^9 s^{-1} at an electron concentration of $n = 6 \times 10^{15}$ m^{-2}. This behavior could not be explained by either the Rashba or the bulk Dresselhaus mechanisms but is attributed to asymmetry or strain effects at dissimilar quantum well interfaces. © *2003 MAIK "Nauka/Interperiodica".*

PACS numbers: 73.63.Hs; 73.21.Fg; 72.25.Rb

In A_3B_5 semiconductors containing heavy metal elements, such as indium, spin–orbit effects are large because of the increased coupling between valence and conduction bands associated with strong relativistic effects. In bulk materials, without magnetic impurities, the only important mechanism producing spin–orbit coupling is the bulk inversion asymmetry [1, 2]. In contrast, in semiconductor heterostructures, the electron spin–orbit interaction can also be controlled by modification of the subband structure using gate voltages [3], strain [4], or selective doping [5].

The role of spin–orbit effects in semiconductors is gaining significant attention because of recent interest in the emerging fields of spintronics and quantum computation [6, 7]. Key issues are the injection and detection of spin-polarized electrons, controlling and manipulating single spins, and the design and experimental realization of novel spintronic devices such as spin-transistors, logic elements, and memory. One obvious way to inject polarized electrons is to use ferromagnetic contacts [8, 9]. It is also possible to exploit the spin-polarized edge states in lateral quantum dot devices subject to a magnetic field [10]. Another, more challenging, approach is to create a spin-polarized current by employing spin–orbit coupling [11]. With the ultimate intention of learning how to manipulate and measure electron spins locally by using gates to modify the spin–orbit interaction, there is a vital interest in searching for semiconductor materials and structures where the electron spin–orbit interaction is large and highly sensitive to gate voltages.

One method that gives information about the spin–orbit coupling is the weak antilocalization (WAL) effect. This is a quantum interference correction to the conductivity, which appears as an abnormal positive magnetoresistance in very low magnetic fields, preceding the more usual negative magnetoresistance associated with weak localization [12]. In metals, WAL was thoroughly studied and understood in the 1980s [13]. In semiconductors the situation is more complex, because new mechanisms involving spin–orbit effects come into play, such as bulk nonsymmetry, asymmetry at heterointerfaces and in quantum wells, and two-dimensional quantum confinement [1].

In this work, the WAL effect is used to study spin relaxation due to the spin–orbit interaction in a strained InGaAs/InP quantum well (QW) structure. Compared with an isomorphous (lattice-matched) structure [14], the strained QW structure showed a larger sensitivity to the gate voltage. In addition an anomalous, nonmonotonic dependence of the spin–orbit time constant on electron concentration was observed. This cannot be explained by conventional bulk inversion and/or Rashba mechanisms and suggests that the existing theoretical understanding of spin–orbit effects in transport phenomena in semiconductor structures needs to be improved.

EXPERIMENTAL

The QW structure studied here was grown on a (100) InP semi-insulated substrate and consisted of the following layers (measured up from the substrate): 450 nm of undoped InP buffer layer, 10 nm $In_xGa_{1-x}As$

¶ This article was submitted by the authors in English.

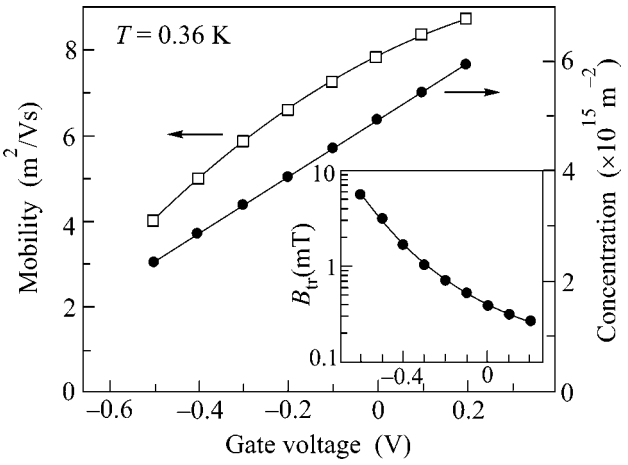

Fig. 1. Electron concentration (solid circles) determined from Shubnikov-de Haas oscillations and the Hall mobility (open squares) of the InGaAs/InP QW structure. Insert shows the characteristic magnetic field $B_{tr} = \hbar/4eD\tau$ as a function of the gate voltage.

($x = 0.76$) quantum well, a 13-nm undoped InP spacer layer, followed by a 13-nm InP doped layer ($N_d = 4 \times 10^{23}$ m^{-3}) and a 13-nm undoped cap layer. The indium content in the quantum well was higher than that of InGaAs lattice-matched to InP ($x = 0.53$) so the QW was compressively strained.

Standard optical photolithography and wet etching was used to form a 0.2-mm-wide Hall bar with 0.4-mm separation between adjacent potential contacts. A 40-nm SiO_2 dielectric layer and a gold gate were deposited on top of this. Measurements were performed in a He3 system; experimental details are given in [14].

Figure 1 shows the electron concentration determined from Shubnikov–de Haas oscillations and the Hall mobility (μ). These transport properties are very similar to those observed earlier in the isomorphous lattice-matched sample studied previously [14]. In particular, the concentration varies linearly with gate voltage, while the mobility has a somewhat slower dependence.

The WAL was used to investigate the spin–orbit scattering action to the conductivity appears as a nonmonotonic dependence of the magnetoresistance at very low magnetic fields, $\mu B \ll 1$. An initial positive magnetoresistance is followed by the more usual negative term. In the theoretical description of the interference corrections, characteristic values of the conductance and magnetic field appear, analogous to the Bohr radius and energy in the theory of excitons. It is therefore convenient to plot the conductance (inverse resistance) in units of the quantum conductivity $G_0 = e^2/\pi h$ and the magnetic field normalized by a characteristic field B_{tr} given by $\hbar/4eD\tau$, where $D = v_F^2\tau/2 = \hbar^2\pi n\mu/m^*e$ is the diffusion coefficient of the two-dimensional electrons and τ is the transport scattering time. B_{tr} depends on both electron concentration and mobility and therefore has a stronger gate voltage dependence than the density (see insert to Fig. 1), changing by more than an order of magnitude over the range of V_g used in the experiment. It should be further noted that, because it is desirable to eliminate the irrelevant classical Lorentz term in the magnetoconductivity $\sigma_{xx}(B) = \sigma_0/(1 + \mu^2B^2)$, it is also convenient to plot the inverse magnetoresistance $\Delta(1/\rho_{xx}) = 1/\rho_{xx} - 1/\rho_0$ rather than $\Delta\sigma = \sigma_{xx} - \sigma_0$, where σ_0 is the zero field value and $\rho_0 = 1/\sigma_0$. This procedure, which would produce zero in the absence of quantum interference corrections, removes the Lorentz term.

Figure 2 shows experimental traces plotted in this way for different gate voltages. The narrow peak around zero magnetic field is the WAL effect, which appears when the spin–orbit scattering rate is comparable to or large than the inverse phase breaking time $1/\tau_\varphi$. It is clear that in this sample the WAL effect shows a nonmonotonic dependence on gate voltage, reaching a maximum around $V_g = -0.3$ and decreasing for both large positive and large negative voltages. Such behavior is unusual and is discussed below.

To extract the phase-breaking and spin–orbit scattering times, we attempted to fit the experiment with the theoretical expression, derived for arbitrary magnetic fields [15]:

$$\Delta\sigma(B) = -(e^2/\pi h) \times \left[F(x, \beta_{s1}) + \frac{1}{2}F(x, \beta_{s2}) - \frac{1}{2}F(x, \beta_\varphi)\right], \quad (1)$$

where

$$B_{tr} = \frac{\hbar}{4eD\tau}, \quad B_{so} = \frac{\hbar}{4eD\tau_{so}} \text{ and } B_\varphi = \frac{\hbar}{4eD\tau_\varphi},$$
$$x = \frac{B}{B_{tr}} = \frac{4eBD\tau}{\hbar}, \quad \beta_\varphi = \frac{\tau}{\tau_\varphi}, \quad \beta_{so} = \frac{\tau}{\tau_{so}}, \quad (2)$$
$$\beta_{s1} = \beta_\varphi + \beta_{so}, \quad \beta_{s2} = \beta_\varphi + 2\beta_{so},$$

with D the diffusion coefficient and τ, τ_{so} and τ_φ the elastic scattering time, the spin–orbit relaxation time, and the phase-breaking time, respectively. The function $F(x, \beta_i)$, defined in [15, 14], describes the interference contributions from the three triplet and one singlet diffusion channels. This equation, derived for an arbitrary magnetic field, reduces to the well-known expression given by Hikami, Larkin, and Nagaoka (HLN) [16] in the limit of small magnetic fields $B \ll B_{tr}$. For the fitting procedure, B_{tr} is known, so there are two adjustable parameters β_φ and β_{so} or equivalently (τ_φ and τ_{so}). One more remark should be added here: to fully describe the WAL effect requires a spin-dependent vector potential with a three-dimensional character [17–19]. The two major spin–orbit relaxation mechanisms (Dresselhaus

and Rashba) are not additive, so in general more complicated expressions with additional fitting parameters should be used to describe the experiments. If, however, one mechanism dominates, a single scalar parameter τ_{so} suffices, which can then be treated on the same footing as τ_φ.

The thin solid lines in Fig. 2 are theoretical fits using this Eq. (1). Details of the fitting procedure are described in [14]. Although this theory should be valid for arbitrary magnetic fields, it was impossible to obtain a good fit over the whole magnetic field range for any of the data. Fitting the central part (small B) resulted in large deviations at higher fields and *vice versa*. This is a common problem in semiconductors encountered by many authors, e.g., [15]. A similar large discrepancy between theory and experiment observed in the isomorphous InGaAs QW sample [14] could only be reconciled by introducing an additional, empirical, scale parameter of order two. It was argued there that one reason for the discrepancy might be the fact that the spin–orbit scattering time was comparable to the transport relaxation time but this is not the case here: for all the curves shown in Fig. 2, $\beta_{so} = \tau/\tau_{so} \le 0.1$, satisfying the condition $\beta_{so} \ll 1$.

Given the large discrepancy between experiment and the theoretical description of the WAL effect (which appears to be a general property of high-mobility 2DEG semiconductors in high magnetic fields), it is not immediately obvious how to extract values of the spin–orbit relaxation time. Further theoretical effort is needed to fix this problem. However, the amplitude of the WAL is clearly affected by τ_{so}, and we have chosen to fit it using the low-field part of the data, where the turnover from a negative to a positive magnetoconductivity is sensitively dependent on τ_{so}. This approach has the advantage that it is also consistent with the procedure commonly used in the literature, whereby the low-field peak is fitted to the HLN expression [5, 16, 19–21] with the implicit understanding that deviations at higher fields are to be expected because of inadequacies in the theory.

The fitted theoretical curves shown in Fig. 2 are plotted well beyond the range of the fit to emphasize the unexpected discrepancy between theory and experiment and to stimulate the attention of theorists.

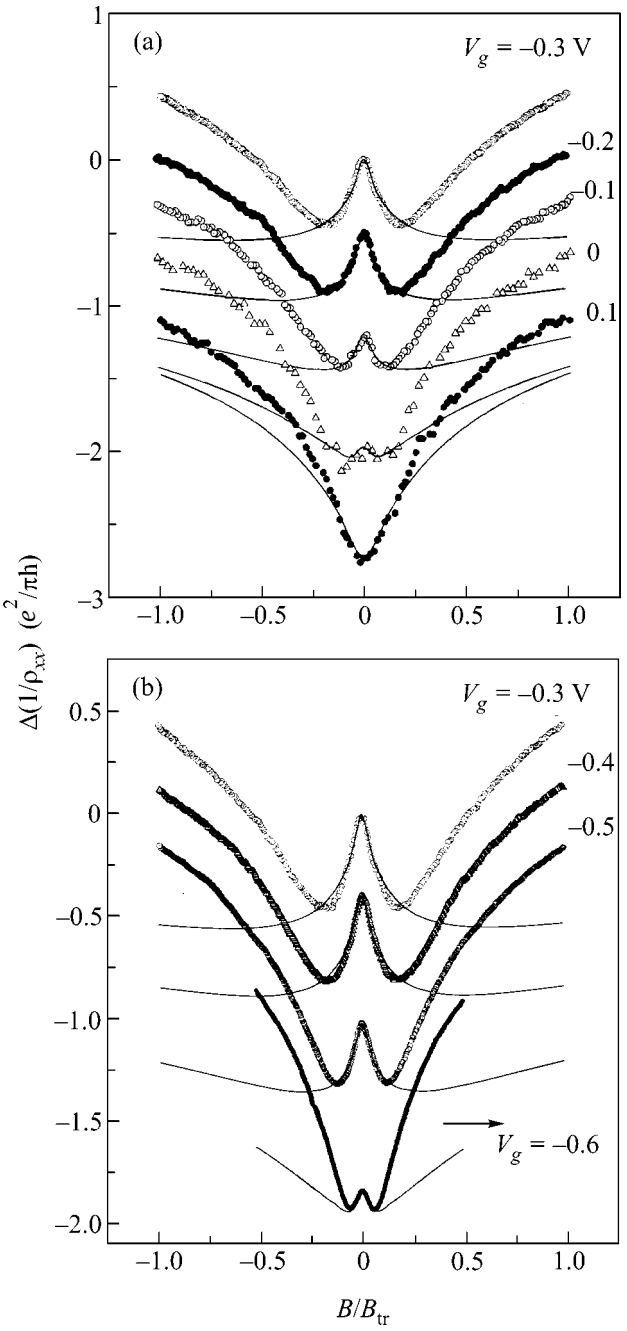

Fig. 2. Experimental traces of the magnetoresistance for different gate voltages at T = 0.36 K. (a) V_g = 0.1, 0, –0.1, –0.2, and –0.3 V; (b) V_g = –0.3, –0.4, –0.5, and –0.6 V. Thin solid lines are best theoretical fits to the experiment using Eq. (1).

DISCUSSION

Although the appearance of the WAL effect requires strong spin–orbit scattering, the curvature of the WAL peak at $B = 0$ and the characteristic width are in fact not determined by τ_{so} but rather by the phase breaking time τ_φ [14, 22]. It is the amplitude of the WAL, in particular the crossover from WAL to weak localizing behavior, that is determined by the ratio τ_φ/τ_{so}.

From Fig. 2 it can seen that the central part of the WAL peak at $B = 0$ changes little for different V_g, and indeed all the fits gave the same value for parameter $\beta_\varphi = 0.010 \pm 0.001$ (for curve at $V_g = +0.1$, where the WAL had vanished, β_φ was set to 0.010, and only β_{so} fit). The WAL peak is narrow, because its width is determined not by β_{so} but rather by β_φ, which can be very small in high-mobility samples. Without spin–orbit

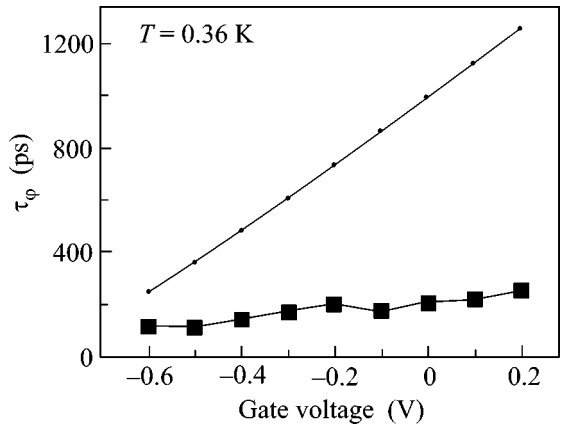

Fig. 3. Phase-breaking time obtained from the set of data in Fig. 2 as a function of the gate voltage. Straight line is the theoretical limit due to electron–electron scattering.

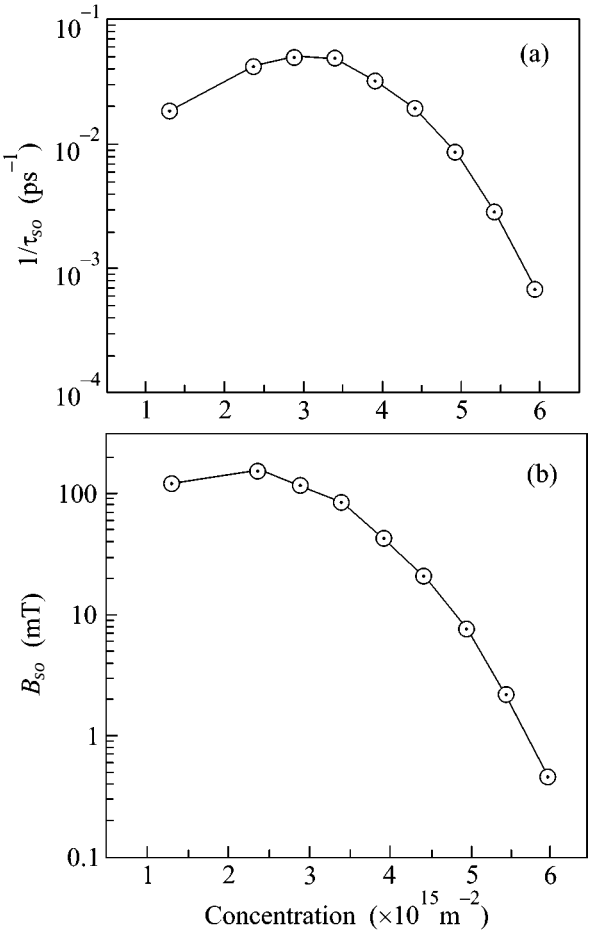

Fig. 4. (a) Spin–orbit scattering rate determined from data in Fig. 2 as a function of electron concentration, (b) spin–orbit magnetic field parameter $B_{so} = \hbar/4eD\tau_{so}$ as a function of electron concentration calculated on the basis of Figs. 1 and 4a.

scattering, a weak localization peak would appear with the same width but of opposite sign.

The phase-breaking time extracted from the fits to the data is plotted in Fig. 3 compared with the predictions of electron–electron scattering calculated from a Fermi liquid model [12, 23]:

$$\frac{1}{\tau_\varphi} = \frac{k_B T \pi G_0}{\hbar \sigma_0} \ln\left(\frac{\sigma_0}{2\pi G_0}\right), \qquad (3)$$

with $G_0 = e^2/\pi h$ and $k_B T\tau/\hbar \ll 1$. The experimental values of τ_φ shown in Fig. 3 are all smaller than predicted. In the literature, an empirical coefficient of order 2 is often introduced to bring the experimental data into better agreement with Eq. (3) [24, 25], but the discrepancy is larger than this. While this model generally works well in metals, where Fermi energy is large and the electron gas can be considered as being very uniform [12, 13], deviations appear at low temperatures, and *a fortiori* in semiconductors. The phase-breaking time is almost universally observed to saturate as the temperature is lowered. For all the data shown in Fig. 3, the temperature was sufficiently low that this saturation had occurred. That is, the absence of any significant gate voltage dependence in τ_φ reflects the temperature saturation rather than an intrinsic insensitivity to electron concentration. The saturation implies that there exist additional phase-breaking mechanisms, the analysis of which is not the topic of this paper.

Figure 4 shows the spin–orbit scattering rate determined from the fits to the data in Fig. 2. It is evident that τ_{so} is a nonmonotonic function of the electron concentration. In 2DEG systems, the two major spin–orbit scattering mechanisms identified in the literature are the Dresselhaus term, associated with the bulk zinc-blend crystal inversion asymmetry, and the Rashba term, associated with built-in electric fields [26]. To identify which mechanism dominates here, it is helpful to consider the dependence on electron concentration of $B_{so} = \hbar/4eD\tau_{so}$ [26, 20, 21]. This value, deduced from the data in Fig. 4a and the transport parameters shown in Fig. 1, is plotted in Fig. 4b.

When the Dresselhaus mechanism dominates, B_{so} should increase with increasing density [20], but in samples where the spin–orbit coupling is large, such as that considered here, the Rashba term usually dominates. The Rashba term results from structural asymmetry and is proportional to the internal electric field. Because the field is proportional to the surface charge density, it should therefore increase as the concentration in the quantum well increases (see, e.g., [27]). In general, the Rashba effect may therefore lead to a nonmonotonic dependence of spin–orbit splitting on gate voltage with a minimum corresponding to a symmetric quantum well [28]. In our case, however, we observe a maximum of the spin–orbit scattering rate (Fig. 4). To the best of our knowledge, this is the first report of such behavior. The nonmonotonic dependence of τ_{so} on elec-

tron concentration in Fig. 4 cannot be explained by either the Dresselhaus or the Rashba mechanisms, and some extra effect, such as strain or the role of the interfaces, must be involved. In the literature, the role of interfaces in the Rashba mechanism is somewhat controversial. In the effective mass approximation, the expectation value of a (smooth) potential gradient integrated over all space is always zero [18, 29]. More generally, the contribution from each separate interface is as large (or even larger) as that from the quantum well asymmetry [29, 30]. The two interfaces in a quantum well often have different properties, resulting, for example, from the growth process. As a result, changes in the amplitude of the electron wavefunction at each interface, produced by changes in gate voltage, will be reflected by changes in any asymmetry associated with having two different interfaces. The unexpected experimental observation that τ_{so} is a nonmonotonic function of gate voltage shows that such an effect plays an important role here.

An alternative method of investigating the strength of the spin–orbit coupling is to use information from the beat patterns of the low-field Shubnikov–de Haas (SdH) oscillations [30–33]. There has, to our knowledge, been no published comparison of results obtained in this way with those deduced, in the same sample, from the WAL effect. In [28], the authors observed beats in SdH oscillations and an anomalous positive magnetoresistance at low field, which could be due to the WAL effect. However, in a more detailed study, the authors of [34] suggested the situation is more complex, with the observed positive magnetoresistance being due to a combination of several factors, including the presence of two spin subbands, a corrugated quantum well, mobility anisotropy, and "possibly weak antilocalization." In the sample studied here, and also in the isomorphic sample studied previously [14], which had a much larger spin–orbit scattering rate, a careful examination of the SdH oscillations over a wide range of gate voltages revealed no sign of any beats. In other samples, under conditions when there was some parallel conduction, beats similar to those observed by other authors could sometimes be seen. However, when analyzed in detail by making gray-scale plots using many traces with small steps in gate voltage, the systematic behavior expected from spin–orbit splitting could not be confirmed. In our samples, we identify the beat pattern observed with interference between two sets of two SdH frequencies, originating from the gated and ungated parts of the sample, and coupled through the parasitic parallel conduction. A similar observation was made by Ensslin *et al.* [35] when they also failed to find any beats in a high-quality InAs/AlSb quantum well sample.

Spin–orbit relaxation in a strained InGaAs/InP QW structure was studied using the WAL effect. The spin–orbit relaxation time was found to depend strongly, and nonmonotonically, on the gate voltage, with the maximum scattering rate ($1/\tau_{so} = 5 \times 10^{10}$ s^{-1}) reached at a density of $n = 3 \times 10^{15}$ m^{-2}. This behavior cannot be explained by either the Rashba or bulk Dresselhaus mechanisms but is rather attributed to asymmetry or strain effects at dissimilar QW interfaces.

Compared with a similar but unstrained sample, the spin–orbit scattering rate here is smaller (by a factor of over 100 at the highest densities). In the strained sample, τ_{so} shows a strong gate voltage dependence (varying from 20 to 1000 ps), while in the unstrained sample τ_{so} was only weakly dependent on electron concentration. This demonstrates that strain can be used as a tool for producing desirable spin–orbit properties when engineering materials for spintronics applications. The exact mechanism responsible for the variation of the spin–orbit coupling in strained samples is not yet understood and is the subject of further investigations. Further theoretical work is also needed to correctly explain the experimentally observed magnetic field dependence, particularly in samples where the WAL effect is large.

S.A.S and A.S. acknowledge support of The Canadian Institute for Advanced Research (CIAR). We would like to thank S. Dickmann for helpful discussions and J. Lapointe for assistance in fabrication of the Hall bar.

REFERENCES

1. *Optical Orientation*, Ed. by F. Meier and B. P. Zakharchenya (North-Holland, Amsterdam, 1984).
2. M. I. D'yakonov and V. Yu. Kacharovskiĭ, Fiz. Tekh. Poluprovodn. (Leningrad) **20**, 178 (1986) [Sov. Phys. Semicond. **20**, 110 (1986)].
3. D. M. Zumbuhl, J. B. Miller, C. M. Marcus, *et al.*, Phys. Rev. Lett. **89**, 276803 (2002).
4. U. Ekenberg and O. Mauritz, Physica E (Amsterdam) **10**, 81 (2001).
5. T. Koga, J. Nitta, T. Akazaki, and H. Takayanagi, Phys. Rev. Lett. **89**, 046801 (2002).
6. D. P. DiVincenzo, J. Appl. Phys. **81**, 4602 (1997).
7. S. A. Wolf, D. D. Awschalom, R. A. Buhrman, *et al.*, Science **294**, 1488 (2001).
8. P. R. Hammar and M. Johnson, Phys. Rev. Lett. **88**, 066806 (2002).
9. A. T. Hanbicki, B. T. Jonker, G. Itskos, *et al.*, Appl. Phys. Lett. **80**, 1240 (2002).
10. A. S. Sachrajda, P. Hawrylak, M. Ciorga, *et al.*, Physica E (Amsterdam) **10**, 493 (2001).
11. T. Koga, J. Nitta, and H. Takayanagi, Phys. Rev. Lett. **88**, 126601 (2002).
12. B. L. Altshuler and A. G. Aronov, in *Electron–Electron Interactions in Disordered Systems*, Ed. by A. L. Efros and M. Pollak (North-Holland, Amsterdam, 1985), p. 1.
13. G. Bergman, Phys. Rep. **107**, 1 (1984).
14. S. A. Studenikin, P. T. Coleridge, N. Ahmed, *et al.*, cond-mat/0206323, Phys. Rev. B (in press).

15. A. Zduniak, M. I. Dyakonov, and W. Knap, Phys. Rev. B **56**, 1996 (1997).
16. S. Hikami, A. Larkin, and Y. Nagaoka, Prog. Theor. Phys. **63**, 707 (1980).
17. Yu. Lyanda-Geller, Phys. Rev. Lett. **80**, 4273 (1998).
18. F. G. Pikus and G. E. Pikus, Phys. Rev. B **51**, 16928 (1995).
19. S. V. Iordanskiĭ, Yu. B. Lyanda-Geller, and G. E. Pikus, Pis'ma Zh. Éksp. Teor. Fiz. **60**, 199 (1994) [JETP Lett. **60**, 206 (1994)].
20. P. D. Dresselhaus, C. M. A. Papavassiliou, R. G. Wheeler, and R. N. Sacks, Phys. Rev. Lett. **68**, 106 (1992).
21. G. L. Chen, J. Han, T. T. Huang, *et al.*, Phys. Rev. B **47**, 4084 (1993).
22. S. A. Studenikin, P. T. Coleridge, N. Ahmed, *et al.*, in *Proceedings of XIV Ural International Winter School on the Physics of Semiconductors* (Ekaterinburg, 2002).
23. B. L. Altshuler, A. G. Aronov, and D. E. Khmelnitskii, J. Phys. C **15**, 7367 (1982).
24. A. M. Kreschchuk, S. V. Novikov, T. A. Polyanskaya, and I. G. Savel'ev, Fiz. Tekh. Poluprovodn. (St. Petersburg) **31**, 459 (1997) [Semiconductors **31**, 391 (1997)]; T. A. Polyanskaya and Yu. V. Shmatsev, Fiz. Tekh. Poluprovodn. (Leningrad) **23**, 3 (1989) [Sov. Phys. Semicond. **23**, 1 (1989).
25. G. M. Minkov, O. E. Rut, A. V. Germanenko, *et al.*, Phys. Rev. B **64**, 235327 (2001).
26. W. Knap, C. Skierbiszewski, A. Zduniak, *et al.*, Phys. Rev. B **53**, 3912 (1996).
27. J. B. Miller, D. M. Zumbuhl, C. M. Marcus, *et al.*, cond-mat/0206375; Phys. Rev. Lett. (in press).
28. S. J. Papadakis, E. P. De Poortere, and H. C. Manoharan, Physica E (Amsterdam) **6**, 284 (2000).
29. L. G. Gerchikova and A. V. Subashiev, Fiz. Tekh. Poluprovodn. (St. Petersburg) **26**, 131 (1992) [Sov. Phys. Semicond. **26**, 73 (1992)].
30. D. Grundler, Phys. Rev. Lett. **84**, 6074 (2000).
31. Th. Schapers, G. Engels, J. Lange, *et al.*, J. Appl. Phys. **83**, 4324 (1998).
32. S. I. Dorozhkin, Phys. Rev. B **41**, 3235 (1990).
33. Y. Sato, Sh. Gozu, T. Kita, and S. Yamada, Physica E (Amsterdam) **10**, 77 (2001).
34. S. J. Papadakis, E. P. De Poortere, H. C. Manoharan, *et al.*, Phys. Rev. B **65**, 245312 (2002).
35. S. Brosig, K. Ensslin, R. J. Warburton, *et al.*, cond-mat/9909007 (1999).

JETP Letters, Vol. 77, No. 6, 2003, pp. 317–320. From Pis'ma v Zhurnal Éksperimental'noĭ i Teoreticheskoĭ Fiziki, Vol. 77, No. 6, 2003, pp. 368–371.

Screening and In-plane Magnetoresistance of an Anisotropic Two-Dimensional Gas¶

V. S. Khrapai

Institute of Solid State Physics, Chernogolovka, Moscow region, 142432 Russia

e-mail: dick@issp.ac.ru

Received December 23, 2002; in final form, February 17, 2003

In order to split the influence of the orbital and spin effects on the in-plane magnetoresistance of a quasi-two-dimensional (2D) gas, we derive its linear response function and dielectric function for the case of anisotropic effective mass. This result is used for the calculation of elastic transport relaxation time of a quasi-two-dimensional system in a parallel magnetic field. The relaxation time is proved to be isotropic in the low-density limit for the case of charged impurity scattering, allowing us to separate the two contributions. © *2003 MAIK "Nauka/Interperiodica".*

PACS numbers: 73.40.-c; 73.43.Qt

Among a variety of experimentally used two-dimensional semiconductor structures, some possess the anisotropy of a Fermi surface originating from that of a bulk material, including *n*-type Si-MOSFETs on other than (100) surfaces [1], AlAs heterostructures [2], *p*-type Si and GaAs structures [3]. The transport properties of such anisotropic semiconductors have been addressed widely [4–6], and it is well known that the Fermi surface anisotropy gives rise in general to the anisotropy of the relaxation time, even if the scattering potential is isotropic [5].

Another possibility is externally introduced anisotropy through the application of a magnetic field parallel to a quasi-2D layer, known to deform a Fermi surface [7] due to the so-called orbital effect [8]. In this case, however, there is additionally a coupling of parallel field to the particles' spins, leading to the partial spin polarization of the system [9, 10] and subsequent change of screening [11] (so-called spin effect). Although substantial interest [2, 9–15] has recently been attracted by longitudinal magnetoresistance (MR) studies of quasi-two-dimensional systems, it has remained unclear so far how the two effects work together [12].

In this letter, we address the screening properties of an anisotropic 2D gas, deriving the linear response function for the case of an elliptic Fermi surface. This result is then used to evaluate the transport relaxation time τ for elastic charged impurity scattering, which surprisingly turns out to be isotropic in the low-density limit. Furthermore, for a partially spin-polarized anisotropic 2D system, the relaxation time for each spin subband is also shown to be isotropic, allowing finally to reach the main result of the paper—to separate the influence of the orbital and spin effects on the longitudinal magnetoresistance of a diluted quasi-2D gas.

In the following, we utilize the simplest possible representation of anisotropy—the elliptic Fermi surface in the effective mass approximation. The interactions are treated in the random phase approximation (RPA), so that the screened linear response function is equal to the linear response of a free particles gas [16]:

$$\chi^{\mathrm{scr}}(\mathbf{q}, 0) = g_v g_s \sum_{\mathbf{k}} |(\rho_q)_{n0}|^2 \frac{f_0(E_{\mathbf{k}}) - f_0(E_{\mathbf{k}+\mathbf{q}})}{E_{\mathbf{k}} - E_{\mathbf{k}+\mathbf{q}} - i0}, \quad (1)$$

where $E_{\mathbf{k}}$ is the kinetic energy of a quasiparticle with momentum k, $f_0(E_{\mathbf{k}})$ is the zero temperature Fermi–Dirac distribution function, g_v, g_s are the valley and spin degeneracies. The excited state $|n\rangle$ contains a single pair of a quasiparticle with momentum $\mathbf{k} + \mathbf{q}$ and a quasihole with momentum $\mathbf{k}$, and the matrix element of the density fluctuation operator $(\rho_q)_{n0}$ is equal to unity. The last property originates entirely from the Bloch type of the Hamiltonian eigenfunctions in the effective mass approximation, similar to the isotropic case [16].

We perform the following change of coordinates to rewrite integral (1) in a spherically symmetric form:

$$\begin{aligned} k_x &\longrightarrow k_x^F \tilde{k}_x, \quad q_x \longrightarrow k_x^F \tilde{q}_x, \\ k_y &\longrightarrow k_y^F \tilde{k}_y, \quad q_y \longrightarrow k_y^F \tilde{q}_y. \end{aligned} \quad (2)$$

The kinetic energy depends solely on the length of the distorted wave vector $\tilde{\mathbf{k}}$,

$$E_{\mathbf{k}} = E_F((k_x/k_x^F)^2 + (k_y/k_y^F)^2) = E_F|\tilde{\mathbf{k}}|^2,$$

¶ This article was submitted by the author in English.

and for integral (1) we have

$$\chi^{\text{scr.}}(\mathbf{q}, 0) = g_v g_s \frac{k_x^F k_y^F}{4\pi^2 E_F} \int \frac{f_0(E_{\tilde{\mathbf{k}}}) - f_0(E_{\tilde{\mathbf{k}}+\tilde{\mathbf{q}}})}{-2\tilde{\mathbf{k}}\cdot\mathbf{q} - \tilde{\mathbf{q}}^2 - i0} d^2\tilde{\mathbf{k}}. \quad (3)$$

In view of the spherical symmetry, the integral value in (3) is invariant to rotation of vector $\tilde{\mathbf{q}}$; hence, the linear response function depends only on its length $\tilde{q}$. The integral in (3) would be the same for an isotropic Fermi surface as well; thus, the only difference from Stern's linear response function [17] is due to the normalizing prefactor proportional to the density of states of an anisotropic Fermi gas $D = g_v g_s \sqrt{m_x m_y}/2\pi\hbar^2$. Finally, we get for χ

$$\chi^{\text{scr.}}(\mathbf{q}, 0) = -D\phi(\tilde{q}),$$
$$\phi(\tilde{q}) = \begin{cases} 1, & (\tilde{q} < 2) \\ 1 - (1 - 4/\tilde{q}^2)^{1/2}, & \tilde{q} \geq 2. \end{cases} \quad (4)$$

The linear response function (4) of an anisotropic system depends on the direction of the perturbation wave vector $\mathbf{q}$ through the variable $\tilde{q} = ((q_x/k_x^F)^2 + (q_y/k_y^F)^2)^{1/2}$, so that the screening does become anisotropic, in contrast to the case of an isotropic Fermi surface [17]. Note, however, that this anisotropy is the same as that of kinetic energy as a function of momentum, since $\tilde{q}^2 = E_{\mathbf{q}}/E_F$.

At the same time, we are able to find the RPA static dielectric function [16]:

$$\varepsilon(\mathbf{q}, 0) = 1 - V(q)\cdot\chi^{\text{scr.}}(\mathbf{q}, 0) = 1 + \frac{q_{TF}}{q}\phi(\tilde{q}), \quad (5)$$

where $V(q) = 2\pi e^2/q$ is the 2D Fourier transform of the bare Coulomb interaction potential and $q_{TF} = 2\pi e^2 D$ is the Thomas–Fermi screening parameter [1].

We now turn to the application of our results to the transport properties of anisotropic 2D Fermi gases. Expression (5) for the dielectric function enables one to find the elastic transport relaxation time. In general, $\tau(\mathbf{k})$ is anisotropic, and calculation of this could be a rather complicated procedure [6, 18]. As we show below, for the case of screened charged impurity scattering, τ is still isotropic in the low-density regime and can be obtained analytically. One has for elastic scattering transport relaxation time

$$\frac{1}{\tau(\mathbf{k})} \propto \int \left(\frac{V(q)}{\varepsilon(\mathbf{q}, 0)}\right)^2 \times \left(1 - \frac{\mathbf{v}_\mathbf{k}\cdot\mathbf{v}_{\mathbf{k}'}}{\mathbf{v}_\mathbf{k}^2}\right)\delta(E_{\mathbf{k}'} - E_F) d^2\mathbf{k}', \quad (6)$$

where $\mathbf{v}_\mathbf{k} = \hbar^{-1} dE_\mathbf{k}/d\mathbf{k}$ is the particle's group velocity. Note that the relaxation time isotropy is already implicit in this expression and is verified in what follows. The first term in the integrand is the square of a scattering matrix element in the Born approximation [5], where we have neglected all the formfactors of the real Coulomb interaction between a quasi-2D electron (hole) and a charged impurity [1]. Applying the change of coordinates (2) to $\mathbf{k}'$ space, we find from (5): $V(q)/\varepsilon(\mathbf{q}, 0) = 2\pi e^2(q + q_{TF}\phi(\tilde{q}))^{-1}$, which, in the low-density limit ($k_x^F, k_y^F \ll q_{TF}$), reduces to[1]

$$V(q)/\varepsilon(\mathbf{q}, 0) = 2\pi e^2 q_{TF}^{-1}\phi^{-1}(\tilde{q}). \quad (7)$$

The second term in (6) accounts for the loss of initial velocity in a scattering event and is similar to the factor $1 - \cos(\widehat{\mathbf{k}, \mathbf{k}'})$ in the isotropic case [18]. Changing to polar coordinates $\tilde{k}_x, \tilde{k}_y \longrightarrow \tilde{k}, \theta$, we rewrite this in terms of the scattering angle θ: $1 - \mathbf{v}_\mathbf{k}\cdot\mathbf{v}_{\mathbf{k}'}/\mathbf{v}_\mathbf{k}^2 = 1 - \cos\theta + A(\mathbf{k})\sin\theta$, where the number $A(\mathbf{k})$ depends on the initial particle momentum $\mathbf{k}$. Hence, in the low density limit we find

$$\frac{1}{\tau(\mathbf{k})} \propto \frac{1}{g_v g_s D}\int_{-\pi}^{\pi} \phi^{-2}(\cos\theta)(1 - \cos\theta) d\theta, \quad (8)$$

since $\tilde{q} = (2 - 2\cos\theta)^{1/2}$, and the part of the integrand odd in θ gives no contribution to the integral. This final expression for the elastic scattering time in the low-density limit is essentially the same as in the isotropic case, the only difference represented by the reciprocal density of states D^{-1} in the prefactor. This finding has two important consequences: in the low-density limit, within the elliptic deformation of the Fermi surface, the transport relaxation time (i) remains isotropic and (ii) increases proportionally to the density of states D.[2]

Comparing to previous studies, we find that our result for the relaxation time isotropy recovers the one derived earlier for short-range scatterers [6], since, for the case of zero spin polarization considered so far, the relevant Fourier components of the screened impurity potential (7) do not depend on the wave vector at all, according to (4). The predicted increase of the relaxation time with the Fermi surface deformation implies of course an increase in conductivity, i.e., the negative magnetoresistance in the direction parallel to the field, caused by the orbital effect, as the effective mass in this direction remains unchanged [7]. This is in contrast to

[1] The low-density limit, determined by the inequality $k_x^F, k_y^F \ll q_{TF}$, is essentially the limit of strong interactions $r_S \gg 1$, where r_S is the Wigner–Seitz radius [1]. Strictly speaking, the utilized random phase approximation is expected to fail in this limit, and the local field corrections should be taken into account [16]. The simplified treatment we use is easily solved and seems to catch the major effect of Fermi surface anisotropy.

[2] One can easily see that these conclusions are also valid for the elastic scattering lifetime, which corresponds to omitting the second term in the integrand of (6).

the positive MR found for the orbital effect in [8], where the change of screening has been neglected. Our prediction could be easily verified in experiments on wide quantum wells, where the in-plane magnetoresistance is mostly due to the orbital effect.

As was mentioned earlier, apart from the Fermi surface deformation, the parallel magnetic field couples to the particles' spins, resulting in a partial spin polarization of the system. Similar to the isotropic case [11], there is no longer a single Fermi surface, but different ones for different spin projections onto the magnetic field axis. We would like to treat only the spin-conserving processes, which means that the linear response of such a partially polarized system is simply the sum of the responses from different spin subbands [11]. Similar to the case of an unpolarized system (expression (4)), the anisotropy of the linear response of a partially polarized system is again the same as that of the kinetic energy as a function of wave vector **q**, which leads to the isotropy of the relaxation time for each spin subband in the limit of low density, as we show below.

Calculating the transport relaxation times $\tau^{\uparrow,\downarrow}$, one should write the integrals of type (6) for major ($\uparrow$) and minor ($\downarrow$) spin subbands separately. In the low-density limit, when the Fermi wave vectors of both subbands satisfy $k_x^{F\uparrow,\downarrow}$, $k_y^{F\uparrow,\downarrow} \ll q_{FT}$, the Fourier image of the screened impurity potential $V(\mathbf{q})/\varepsilon(\mathbf{q})$ has the anisotropy of the linear response function and kinetic energy, according to (7). This means that the change of coordinates (2) applied to the integrands leads to the same expressions for $\tau^{\uparrow,\downarrow}$ as one gets in the isotropic case [11]. Thus, the relaxation times are isotropic, and the only effect of anisotropy is again to normalize the absolute value of $\tau^{\uparrow,\downarrow}$ through the density of states dependent prefactor (8). We are now able to write down the conductivity tensor of the partially polarized anisotropic system:

$$\hat{\sigma} = \hat{\sigma}^{\uparrow} + \hat{\sigma}^{\downarrow} = n_S e^2 \tau_0 \hat{m}^{-1} \frac{D}{D_0} F_{DG}(\xi), \qquad (9)$$

where $\hat{\sigma}^{\uparrow}$, $\hat{\sigma}^{\downarrow}$ are the major and minor spin-subband conductivity tensors and e, n_S, τ_0, D_0 are, respectively, the electron charge, density of 2D particles, the zero-field isotropic relaxation time, and the density of states. D and $\hat{m}$ are, respectively, the density of states and the effective mass tensor in magnetic field. The last term in (9) stands for the Dolgopolov–Gold calculated change of the conductivity of an isotropic system as a function of its degree of spin polarization $\xi = (n_\uparrow - n_\downarrow)/(n_\uparrow + n_\downarrow)$ [11]. Note that, for the case of a quasi-2D system with zero field anisotropic mass, this result is valid only for a parallel field applied along the main axes of symmetry; otherwise, the Fermi surface loses its ellipticity in magnetic field. Let us show finally how this simple expression allows us to separate immediately the contributions from spin and orbital effects on the longitudinal magnetoresistance of a diluted quasi-2D system.

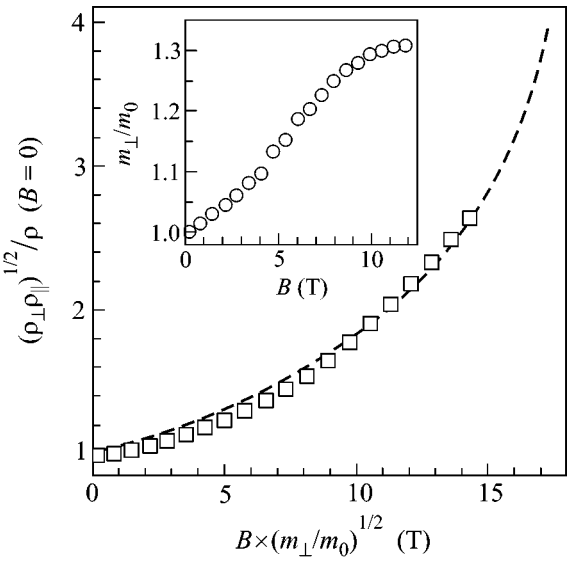

In the inset, the effective mass growth caused by the orbital effect [8] is shown, extracted from the longitudinal MR data of [12] ($n_S \approx 3 \times 10^{10}$ cm^{-2}) as described in the text. The spin effect contribution is shown in the figure body. The fit to theoretical dependence [11] (dashed line) gives full spin polarization field in the absence of orbital effect $B_P^0 \approx$ 17.3 T, corresponding to a Landé factor of $g^* \approx 2.1$.

We focus on the recent magnetoresistance studies of the 2D electron gas of AlGaAs/GaAs heterostructure [12]. This system is isotropic in zero magnetic field; hence, according to (9), the anisotropy of experimental MR [12] is due to the effective mass change in the direction perpendicular to magnetic field [8]:

$$m_\perp/m_0 = \rho_\perp(B)/\rho_\parallel(B),$$

where $\perp$ and $\parallel$ mark the resistances measured in directions perpendicular and parallel to in-plane magnetic field, respectively. The spin effect contribution in (9) is thus given by

$$F_{DG}^{-1}(\xi) = \sqrt{\frac{\rho_\perp(B)\rho_\parallel(B)}{\rho_\perp(B=0)\rho_\parallel(B=0)}}. \qquad (10)$$

The degree of spin polarization depends on both the Zeeman energy $g\mu_B B$ and the effective mass at a given field value: $\xi(B) = (E_{F\uparrow} - E_{F\downarrow})/(E_{F\uparrow} + E_{F\downarrow}) = g\mu_B BD/n_S$, where $E_{F\uparrow,\downarrow}$ are the kinetic parts of the Fermi energy for two spin subbands and g and μ_B are the Landé factor and Bohr magneton. Equivalently, the last equation reads $\xi(B) = B/B_P^0\sqrt{m_\perp(B)/m_0}$, where $B_P^0 = 2E_F^0/g\mu_B$ is the full spin polarization field in the absence of the orbital effect [11].

In the inset to the figure, we show the effective mass growth extracted in the above manner from the $\rho_\perp$, $\rho_\parallel$

data of [12]. The effective mass in the direction perpendicular to field grows by about 30% in moderate fields, as caused by the orbital effect [8]. For such a slight deformation, the utilized approximation of elliptic Fermi surface should work reasonably well, in contrast to the general case [7]. The partial spin polarization has a major effect on MR, as reflected by its small anisotropy [12], and leads to a roughly threefold resistance increase, as is shown in the body of the figure. Full spin polarization was not reached in [12], for which reason the saturation [11] of the geometrical mean of the resistivities parallel and perpendicular to in-plane field predicted by (10) is not seen in the figure. Fitting to calculation [11], we obtain the B_P^0 value 17.3 T, which corresponds to a Landé factor of $g^* \approx 2.1$ at $n_S \approx 3 \times 10^{10}$ cm^{-2}, in agreement with previous studies [10, 12].

We would like to add a note here concerning the applicability of the MR data analysis presented above to real interacting quasi-2D systems. Apart from the single-particle effect of Fermi surface deformation considered thus far, the squeezing of the 2D layer by the parallel magnetic field additionally changes the form factors of Coulomb interaction between particles [1] and increases the Wigner–Seitz ratio [15], which can in principle lead to the renormalization of the zero field effective mass and g factor [19]. In the presence of such many-body effects, the spin effect contribution [11] cannot be extracted with formula (10). Experimentally, this means that the geometrical mean of resistivities $\sqrt{\rho_\perp(B)\rho_\parallel(B)}$ does not saturate upon reaching full spin polarization. The in-plane magnetoresistance anisotropy, however, should still give the anisotropy of effective mass $\rho_\perp/\rho_\parallel = m_\perp/m_\parallel$, similar to the single-particle picture, although independent measurement is required to find the full spin polarization field B_P^0 [14, 15].

In conclusion, we have derived the linear response function and dielectric function of a 2D Fermi gas with anisotropic effective mass. In the low-density limit, the screened charged impurity potential is shown to possess the same symmetry as the kinetic energy as a function of wave vector. As a result, the elastic transport relaxation time τ is isotropic in this limit, even if the 2D system is partially spin polarized. This finding allows us to separate for the first time the influence of the orbital [8] and spin [11] effects on the in-plane magnetoresistance of a diluted quasi-two-dimensional system.

The author would like to thank V.T. Dolgopolov, S.V. Iordanski, A.A. Shashkin, and A.A. Zhukov for useful discussions and acknowledges the support of the Russian Foundation for Basic Research and of the Russian Ministry of Sciences under the “Nanostructures” and “Mesoscopics” programs.

REFERENCES

1. T. Ando, A. Fowler, and F. Stern, Rev. Mod. Phys. **54**, 437 (1982).
2. E. P. De Poortere, E. Tutuc, Y. P. Shkolnikov, *et al.*, Phys. Rev. B **66**, 161308R (2002).
3. C. Kittel, *Introduction to Solid States Physics*, 4th ed. (Wiley, New York, 1976; Nauka, Moscow, 1978).
4. C. Herring and E. Vogt, Phys. Rev. **101**, 944 (1956).
5. A. G. Samoĭlovich, I. Ya. Korenblit, and I. V. Dakhovskiĭ, Dokl. Akad. Nauk SSSR **139**, 355 (1961) [Sov. Phys. Dokl. **6**, 606 (1962)].
6. Yasuhiro Tokura, Phys. Rev. B **58**, 7151 (1998).
7. U. Merkt, *The Physics of the Two-Dimensional Electron Gas*, Ed. by J. T. Devreese and F. M. Peeters (Plenum, New York, 1987), p. 293.
8. S. Das Sarma and E. H. Hwang, Phys. Rev. Lett. **84**, 5596 (2000).
9. J. Yoon, C. C. Li, D. Shahar, *et al.*, Phys. Rev. Lett. **84**, 4421 (2000); E. Tutuc, E. P. De Poortere, S. J. Papadakis, and M. Shayegan, Phys. Rev. Lett. **86**, 2858 (2001).
10. E. Tutuc, S. Melinte, and M. Shayegan, Phys. Rev. Lett. **88**, 036805 (2002).
11. V. T. Dolgopolov and A. Gold, Pis’ma Zh. Éksp. Teor. Fiz. **71** (1), 42 (2000) [JETP Lett. **71**, 27 (2000)].
12. V. S. Khrapai, E. V. Deviatov, A. A. Shashkin, and V. T. Dolgopolov, Proc. NGS 10, IPAP Conf. Ser. **2**, 105 (2001); see also cond-mat/0005377.
13. C.-T. Liang, C. G. Smith, M. Y. Simmons, and D. A. Ritchie, Phys. Rev. B **64**, 233319 (2001).
14. J. Zhu, H. L. Stormer, L. N. Pfeiffer, *et al.*, Phys. Rev. Lett. **90**, 056805 (2003).
15. E. Tutuc, S. Melinte, E. P. De Poortere, *et al.*, cond-mat/0301027.
16. D. Pines and Ph. Nozières, *The Theory of Quantum Liquids* (Benjamin, New York, 1966), Vol. 1.
17. F. Stern, Phys. Rev. Lett. **18**, 546 (1967).
18. J. M. Ziman, *Principles of the Theory of Solids* (Cambridge Univ. Press, Cambridge, 1964; Mir, Moscow, 1966).
19. S. Yarlagadda and G. F. Giuliani, Phys. Rev. B **49**, 14188 (1994).

JETP Letters, Vol. 77, No. 6, 2003, pp. 321–323. Translated from Pis'ma v Zhurnal Éksperimental'noĭ i Teoreticheskoĭ Fiziki, Vol. 77, No. 6, 2003, pp. 372–375.

Kinematic Multiplication of Elementary Steps on a Crystal Surface

A. Ya. Parshin* and V. L. Tsymbalenko**

** Kapitza Institute for Physical Problems, Russian Academy of Sciences, Moscow, 119334 Russia*
e-mail: parshin@kapitza.ras.ru
*** Russian Research Centre Kurchatov Institute, Institute of Superconductivity and Solid-State Physics, Moscow, 123182 Russia*

Received February 20, 2003

The dynamics of elementary steps on an atomically smooth crystal–liquid interface and, in particular, the process of collisions of steps differing in sign are considered. It is shown that, along with the conventional annihilation of steps in such collisions, both the overthrow of steps to the neighboring row with the formation of a new atomic layer (passage) and the reflection of steps from each other can take place under certain conditions. The overthrow of steps gives a qualitatively new mechanism of the growth of facets in the absence of renewable sources such as grown-in dislocations. Under these conditions, the growth kinetics of a crystal with atomically smooth facets changes substantially. In particular, the processes considered above may form a basis for physical mechanisms of unconventional growth regimes observed for helium crystals at low temperatures. © *2003 MAIK "Nauka/Interperiodica".*

PACS numbers: 81.10.Aj; 67.80.-s; 68.08.-p

It is well known that the growth of a crystal with atomically smooth facets can proceed due to either continuously acting sources of elementary steps such as screw dislocations and Frank–Read sources or two-dimensional nucleation. The impossibility of crossings is an essential property of steps, which is commonly not questioned. For steps of the same sign, this means the impossibility of one atomic layer to hang over another, that is, the impossibility of a configuration with a high excessive energy. From the same energy considerations, it is clear that, upon coming in contact, two steps of different signs annihilate in the contact region with the formation of a bridge (Fig. 1a). The step noncrossing property was used as the basis in classical works on the theory of crystal growth [1].

The property of steps indicated above is undoubtedly retained as long as all the processes with the participation of steps are sufficiently slow, so that each step section at each instant of time is in a local equilibrium and the kinetic energy of a step can be neglected. In other words, the corresponding relaxation time must be small in comparison with the "collision time" w/V, where V is the relative velocity of steps and w is the characteristic width of a step, which equals the interatomic distance by the order of magnitude. This condition can easily be violated in the case of atomically smooth facets of a helium crystal at temperature tending to zero, when the relaxation time increases without limit and the step velocities can be very high up to the sound velocity [2]. It is natural to suggest that the colliding steps of different signs in this case will be able to pass inertially one over the other forming a new atomic layer (see Fig. 1b) or to reflect from each other. We will show in this brief communication that this actually takes place under certain conditions. Here it is necessary to note that this idea in itself is analogous to the idea of the "kinematic multiplication" of dislocations in

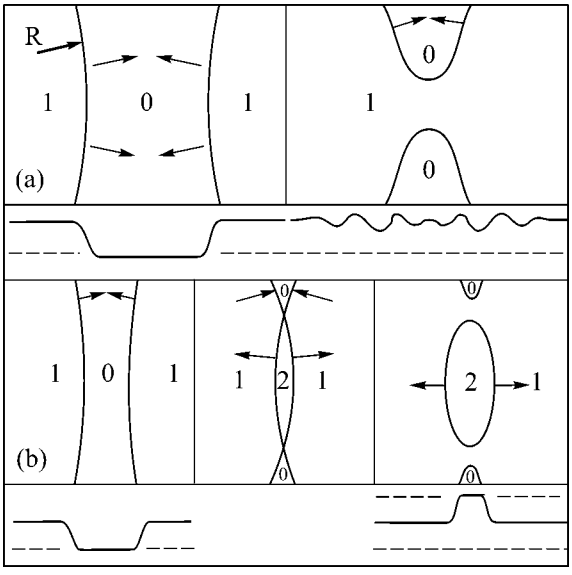

Fig. 1. (a) Collision of steps in a quasi-static case. (b) Passage of steps one over the other at high velocities and large relaxation times. A nucleus of a new layer is formed at this place as a result of the collision.

the crystal bulk, which was proposed by Frank [3] even before the discovery of Frank–Read sources.

We will describe the structure and dynamics of steps using the so-called weak-coupling approximation, which is widely used in the theory of phase transitions associated with the initiation of faceting in helium crystals (see, for example, [4]). In this approximation, the effective periodic potential retaining the surface in the vicinity of certain equilibrium positions is small in comparison with the surface energy because of strong fluctuations. Correspondingly, the energy of a step, that is, the transition region between two neighboring equilibrium positions of the surface, is also small, and the width of this region is conversely large in comparison with the interatomic distance. This allows one to introduce a continuous variable $\zeta(\mathbf{r})$ corresponding to a local displacement of the surface averaged over the fluctuations. Consider the case of extremely low temperatures. Then the dissipation, which accompanies the motion of steps, and the external supersaturation, which is necessary for its maintenance, are small, and the corresponding terms in the equations of motion can be neglected. In addition, we will consider both the liquid and the crystal incompressible. Then a displacement of the surface is associated only with crystallization or melting, and the total energy is a sum of the surface and kinetic energies. The surface energy minus an inessential constant can be written as

$$H_{\text{surf}} = \int\frac{\alpha}{2}(\nabla\zeta)^2 d^2\mathbf{r} + \int U_0\left(1-\cos\frac{2\pi\zeta}{a}\right)d^2\mathbf{r}, \quad (1)$$

where the first term takes into account a change in the surface area, the second term corresponds to the contribution of the effective potential, a is the interplanar distance, and α is the energy of unit surface area (here, we make no distinction between the surface energy and stiffness).

The kinetic energy in this case is the kinetic energy of the liquid, whose motion is due to the displacement of the surface;[1] with regard to the conservation of mass in crystallization, we obtain

$$H_{\text{kin}} = \frac{1}{4\pi}\frac{(\rho_s-\rho_l)^2}{\rho_l}\int\frac{\partial\zeta(t,\mathbf{r})}{\partial t}\frac{\partial\zeta(t,\mathbf{r}')}{\partial t}\frac{d^2\mathbf{r}d^2\mathbf{r}'}{|\mathbf{r}-\mathbf{r}'|}, \quad (2)$$

where ρ_s and ρ_l are the densities of solid and liquid helium. The corresponding equation of motion takes the form

$$\frac{1}{2\pi}\int\frac{\partial^2\varphi}{\partial t^2}\frac{d^2\mathbf{r}}{|\mathbf{r}-\mathbf{r}'|} - \Delta\varphi + \sin(\varphi) = 0, \quad (3)$$

[1] The additional contribution due to the rearrangement of atoms on passing from the liquid to the crystalline state [5] is relatively small and does not affect the qualitative conclusions.

where dimensionless coordinates x and y are measured in units ξ and time, in units τ

$$\xi = \sqrt{\frac{\alpha a^2}{4\pi^2 U_0}}, \quad \tau = \sqrt{\frac{\Delta\rho^2}{\rho_l}\frac{a^2}{4\pi^2 U_0}}\xi, \quad \varphi = \frac{2\pi\zeta}{a}, \quad \Delta\rho = \rho_s-\rho_l, \quad (4)$$

and U_0, in turn, can be expressed through the energy β of the unit length of immobile step

$$U_0 = \frac{\pi^2}{16}\frac{(\beta/a)^2}{\alpha}. \quad (5)$$

Let us also give here numerical values for the (0001) facet of a ^{4}He crystal: $\alpha = 0.25$ erg/cm^2 [6–8], $\beta/a = 0.014$ erg/cm^2 [8], and the other parameters

$$U_0 \approx 1.5\times10^{-3}\alpha, \quad \xi \sim 4a, \quad \tau \sim 5\times10^{-12}\ \text{s}, \quad V_0 = \xi/\tau \sim 2.8\times10^4\ \text{cm/s} < c \approx 3.6\times10^4\ \text{cm/s}, \quad (6)$$

where c is the speed of sound in the liquid.

The real steps on a crystal surface are always somewhat curved (see Fig. 1), and the radius of curvature R commonly exceeds or, at least, coincides by the order of magnitude with the radius of the critical nucleus R_c. Because $R_c \gg \xi$ (otherwise, the probability of conventional two-dimensional nucleation would be high; note also that the value of R_c is inversely proportional to the external supersaturation, which we assume to be small), the inequality $R \gg \xi$ is also fulfilled, so that steps in collisions first come in contact in a region $R^* \sim \sqrt{R\xi}$, which is small in comparison with R, where they can be considered rectilinear and parallel to each other. Therefore, first we must analyze the one-dimensional case, in which instead of Eq. (3) we have

$$\frac{1}{\pi}\int\ln\left(\frac{R^*}{|x'-x|}\right)\frac{\partial^2\varphi}{\partial t^2}dx' = \frac{\partial^2\varphi}{\partial x^2} - \sin\varphi. \quad (7)$$

This equation was solved numerically in the following sequence. First, the function $\varphi(x - Vt)$, which described the stationary shape of a single step moving with a prescribed velocity V measured in units V_0, was defined. Note that, at $V = 0$, this shape coincides with the shape of a single kink of the sine-Gordon equation and deviates more and more from this shape with increasing V. At $V > 1$, the stationary shape in the form of a simple kink loses its stability. The question of which configurations are stable in this case still remains unexplored.

At the second stage, the function corresponding to the stationary shape of two steps of different signs moving toward each other with velocities V_1 and V_2 was used as the initial condition for the solution of the problem of collision between such two steps. It was found that, depending on the values of initial velocities, three

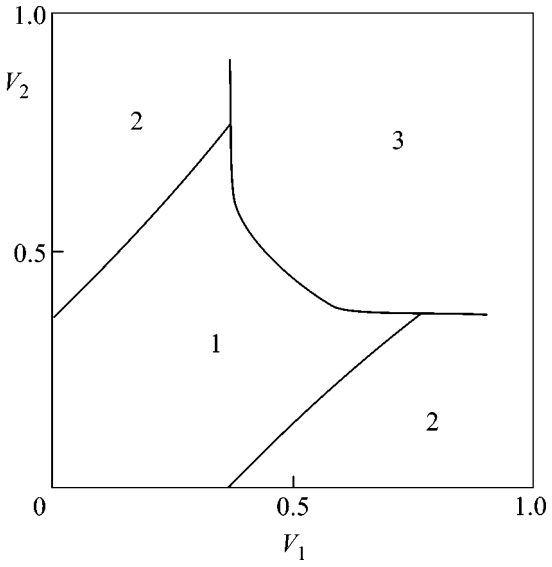

Fig. 2. Schematic diagram of collision processes of steps moving with different velocities of counter motion: regions correspond to (1) annihilation of steps, (2) reflection, and (3) passage with the creation of a new atomic layer.

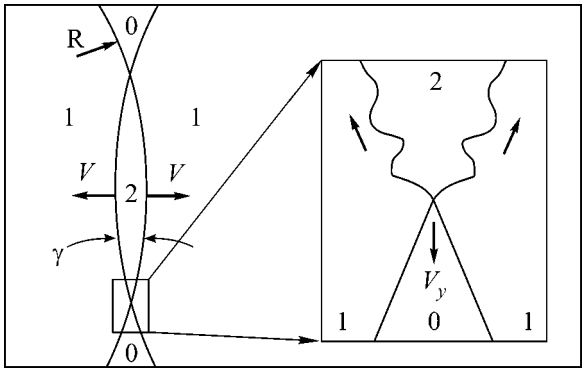

Fig. 3. Generation of excitations at the crossing point of steps and their propagation along the boundary of the newly formed layer.

qualitatively different results could be obtained: the passage of step over one another with "overthrow" to the neighboring row, annihilation, and reflection. All three processes are accompanied by the emergence of "ripplons" of higher or lower amplitudes. Regions corresponding to each of these processes are indicated in the schematic diagram in Fig. 2.

The further evolution of the system is substantially different in these three cases. Case (3), when a nucleus of a new atomic layer confined by two intersecting arcs of steps is formed (Fig. 1b), is of most interest. Generally speaking, it should be expected that an instability leading eventually to the formation of a bridge, as is shown in Fig. 1b, will develop in the crossing region. However, the terms in the total equation of motion (3) responsible for this instability are small at the initial instant of time by virtue of the smallness of the crossing angle γ; that is, the corresponding lifetime is large. At the same time, the result of the action of perturbations is not accumulated with time, because the crossing point itself moves along the Y axis with a velocity $V_y \cong 2V/\gamma$, which is faster than the velocity of the propagation of perturbations along the step ($V_{exc} \leq 1$, see Fig. 3). Therefore, the formation of a bridge becomes possible only at $\gamma \sim 1$; that is, when the size of the nucleus of the new layer l is on the order of R, and thus $l > R_c$. We can see that actually no additional restriction for the stable growth of the nucleus of the new layer arises in comparison with the schematic diagram in Fig. 2.

Note in conclusion that, with regard to the phenomenon considered above, the theory of the growth of atomically smooth crystal facets at low temperatures requires substantial corrections. In particular, it is possible that the proposed growth mechanism provides the basis for the so-called "burstlike" growth of dislocation-free helium crystals observed experimentally [2], which defies explanation within the known growth mechanisms.

We are grateful to V.I. Marchenko for useful discussions.

This work was supported by the Civilian Research & Development Foundation (project no. Rp-2411-MO-02), the State Program of Support for Scientific Schools, and the Russian Foundation for Basic Research (project no. 02-02-16772).

REFERENCES

1. W. K. Burton, N. Cabrera, and F. C. Frank, Philos. Trans. R. Soc. London **243**, 299 (1951).
2. J. P. Ruutu, P. J. Hakonen, A. V. Babkin, *et al.*, J. Low Temp. Phys. **112**, 117 (1998).
3. F. C. Frank, in *Report of the Conference on Strength of Solids* (Physical Society, London, 1948), p. 46.
4. P. Nozieres, in *Solids Far from Equilibrium*, Ed. by C. Godreche (Cambridge Univ. Press, Cambridge, 1991), p. 1.
5. L. Puech and B. Castaing, J. Phys. Lett. **43**, 601 (1982).
6. A. V. Babkin, D. B. Kopeliovich, and A. Ya. Parshin, Zh. Éksp. Teor. Fiz. **89**, 2288 (1985) [Sov. Phys. JETP **62**, 1322 (1985)].
7. O. A. Andreeva and K. O. Keshishev, Pis'ma Zh. Éksp. Teor. Fiz. **46**, 160 (1987) [JETP Lett. **46**, 200 (1987)].
8. E. Rolley, C. Guthmann, E. Chevalier, and S. Balibar, J. Low Temp. Phys. **99**, 851 (1995).

Translated by A. Bagatur'yants

JETP Letters, Vol. 77, No. 6, 2003, pp. 324–327. From Pis'ma v Zhurnal Éksperimental'noĭ i Teoreticheskoĭ Fiziki, Vol. 77, No. 6, 2003, pp. 376–379.

On the Integration of Some Classes of (n + 1)-dimensional Nonlinear Equations of Mathematical Physics¶

A. I. Zenchuk

Center of Nonlinear Studies of Landau Institute for Theoretical Physics, Moscow, 119334 Russia

e-mail: zenchuk@itp.ac.ru

Received February 6, 2003

This paper presents a method for construction of the families of particular solutions to some new classes of (n + 1)-dimensional nonlinear partial differential equations (PDE). The method is based on the specific link between algebraic matrix equations and PDEs. Admittable solutions depend on arbitrary functions of n variables. Examples of deformed Burgers-type equations are given. © *2003 MAIK "Nauka/Interperiodica".*

PACS numbers: 02.30.Jr

1. INTRODUCTION

Many different methods have been developed for the analytical investigation of nonlinear partial differential equations (PDEs) during the last decades. Especially attractive are methods for the study of so-called completely integrable systems. The particular interest in these equations is enhanced due to their wide range of application in physics. We emphasize different dressing methods, which are based on the fundamental properties of linear operators, either differential or integral: the Zakharov–Shabat dressing method [1, 2], $\bar{\partial}$ problem [3–6], and Sato theory [7].

We suggest a method for construction of the families of particular solutions to some new classes of (n + 1)-dimensional nonlinear PDEs, $n \geq 2$. It is based on the general properties of linear algebraic matrix equations [7–9]. In general, this method supplies a family of solutions depending on the set of arbitrary functions of n variables for an (n + 1)-dimensional PDE. The presented method can also be applied to the classical (2 + 1)-dimensional PDE integrable by the inverse scattering technique (IST). In this case, our algorithm is similar to the algorithm represented in [7, 10].

We discuss a general algorithm relating linear algebraic equations with nonlinear PDEs. Then we show that these PDEs are compatibility conditions for the appropriate overdetermined linear system of equations having different structure in comparison with the classical isospectral problem. Some examples of (2 + 1)-dimensional equations are presented.

¶ This article was submitted by the author in English.

2. GENERAL ALGORITHM

As mentioned above, our algorithm is based on the fundamental properties of the linear matrix algebraic equation

$$\Psi U = \Phi, \tag{1}$$

where $\Psi = \{\psi_{ij}\}$ is an $N \times N$ nondegenerate matrix and U and Φ are $N \times M$ matrices, $M < N$. The solution of this equation is unique, and hence the homogeneous equation with matrix Ψ has only the trivial solution. Thus, if we find a transformation that maps nonhomogeneous Eq. (1) onto the homogeneous equation $\Psi\tilde{U}(U) = 0$, then $\tilde{U}(U) = 0$.

It may be shown that such transformations can be performed using differential operators having a special structure. For this purpose, let us introduce two types of additional parameters $x = (x_1, \ldots, x_n)$ ($n = \dim(x)$) and $t = (t_1, t_2, \ldots)$ by the following systems:

$$\Psi_{x_i} = \Psi B_i + \Phi C_i, \quad i = 1, \ldots, n \tag{2}$$

(B_i and C_i are constant $N \times N$ and $M \times N$ matrices respectively) and

$$\mathcal{M}_i\Psi = 0, \quad \mathcal{M}_i\Phi = 0, \quad \mathcal{M}_i = \partial_{t_i} + L_i, \tag{3}$$

where L_i are arbitrary linear differential operators having derivatives with respect to variables x_j and constant scalar coefficients, so that system (2) is compatible with system (3). For the sake of simplicity, in this paper we use only one parameter t, omit subscripts in Eq. (3), and use the n-dimensional Laplacian for L: $\mathcal{M} = \partial_t + \sum_{k=1}^{n} \alpha_k \partial_{x_k}^2$. Hereafter, indices i, j, and k run values from 1 to n unless otherwise specified.

Let us study the compatibility conditions for the system (2) itself, which has the following form:

$$(\Psi B_j + \Phi C_j)B_i + \Phi_{x_j} C_i = (\Psi B_i + \Phi C_i)B_j + \Phi_{x_i} C_j. \quad (4)$$

We require that matrices B_i and C_i satisfy the two conditions

$$C_j B_i - C_i B_j = 0, \quad B_j B_i - B_i B_j = 0 \quad (5)$$

and that matrices C_j have the following structure: $C_j = [P_j \mid 0_{M, N-R}]$, $R \le M$, where P_j are $M \times R$ matrices with rang R and $0_{A,B}$ means $A \times B$ zero matrix. Then Eq. (4) is simplified to

$$\Phi_{x_i} P_j - \Phi_{x_j} P_i = 0, \quad (6)$$

which results in the first nonlinear equation for U owing to Eqs. (1) and (2):

$$(B_j + UC_j)UP_i + U_{x_j} P_i = (B_i + UC_i)UP_j + U_{x_i} P_j. \quad (7)$$

Let us show that another nonlinear matrix equation can be derived using operator $\mathcal{M}$. For this purpose, we apply operator $\mathcal{M}$ to both sides of Eq. (1) and use Eqs. (2) and (3):

$$0 = \mathcal{M}\Phi = (\mathcal{M}\Psi)U + \Psi\mathcal{M}U + 2\sum_{k=1}^{n} \alpha_k \Psi_{x_k} U_{x_k}$$

$$= \Psi\left(\mathcal{M}U + 2\sum_{k=1}^{n} \alpha_k (B_k + UC_k)U_{x_k}\right) = 0.$$

Since $\det(\Psi) \neq 0$, one has the second nonlinear equation for the matrix U:

$$U_t + \sum_{k=1}^{n} \alpha_k (U_{x_k x_k} + 2(B_k + UC_k)U_{x_k}) = 0. \quad (8)$$

Combining Eqs. (7), (8) and using condition (5), one can eliminate matrices B_i and receive a system of equations for matrix V composed of the first R rows of the matrix U. The first equation exists for any n. To derive it, let us eliminate operators B_i from Eq. (7) using Eqs. (5) and (8):

$$P_i\left(U_{j_t} + \sum_{k=1}^{n} \alpha_k (U_{j_{x_k x_k}} + 2U_k U_{j_{x_k}})\right)$$

$$- P_j\left(U_{i_t} + \sum_{k=1}^{n} \alpha_k (U_{i_{x_k x_k}} + 2U_k u_{i_{x_k}})\right) \quad (9)$$

$$+ 2\sum_{k=1}^{n} \alpha_k P_k (U_{i_{x_j}} - U_{j_{x_i}} + [U_j, U_i])_{x_k} = 0.$$

Another equation exists if only $n > 2$. In this case, we can derive the matrix equation without operators B_i using any three Eqs. (7) with pairs of indices (i, j), (j, k), (k, i) and relations (5):

$$\sum_{perm} P_i (U_{j_{x_k}} - U_{k_{x_j}} + [U_k, U_j]) = 0, \quad U_i = VP_i, \quad (10)$$

where the sum is over the cyclical permutation of indexes i, j, and k. In general, both Eqs. (9) and (10) should be considered simultaneously. Otherwise, the nonlinear system cannot be completed.

Thus, Eqs. (9) and (10) do not depend on the parameter N (which characterizes the dimensions of the matrices in the Eq.(1)) or on the matrices B_i; i.e., N is an arbitrary positive integer and B_i are $N \times N$ matrices fitting relations (5).

Arbitrary functions of variables x_j ($j = 1, \ldots, n$) appear in the solution V due to the matrix function Φ, defined by system (6). The number of arguments in the arbitrary functions, as well as the number of these functions, is defined by the particular choice of the matrices P_j and the dimension n of x space. For an n-dimensional x space and $R < M$, we are able to present examples with N arbitrary functions of n variables. But in particular cases, the situation may be different (see *Examples*). For instance, if $R = M$, then Φ may depend at most on $N \times M$ arbitrary scalar functions of a *single* variable, which is in accordance with [7]. Detailed discussion of this problem is beyond the scope of this paper.

2.1. On the Operator Representation of PDEs

Classical nonlinear (2 + 1)-dimensional systems integrable by the IST are in the family of equations introduced in the previous section. To clarify this statement, we derive the overdetermined linear system of PDEs with the compatibility condition in the form of Eqs. (9) and (10) and compare it with the classical isospectral problem. First, we introduce an arbitrary $R \times N$ matrix function $\mathbf{R}(\lambda)$ of the additional complex parameter λ. Multiplying Eqs. (7) and (8) by $\mathbf{R}(\lambda)\exp\eta$, $\eta = \sum_{k=1}^{n} B_k x_k - (\sum_{k=1}^{n} \alpha_k B_k^2)t$ from the left, we introduce the function $\hat{\Psi} = \mathbf{R}e^{\eta}U$. We get after transformations

$$\hat{\Psi}_{x_j} P_i - \hat{\Psi}_{x_i} P_j = \hat{\Psi} P_i U_j - \hat{\Psi} P_j U_i, \quad (11)$$

$$\hat{\Psi}_t + \sum_{k=1}^{n} \alpha_k (\hat{\Psi}_{x_k x_k} + 2\hat{\Psi} P_k V_{x_k}) = 0. \quad (12)$$

If $R = M$, i.e., if all P_j are square nondegenerate matrices, then system (11), (12) is equivalent to the classical $M \times M$ overdetermined linear system for the corresponding (2 + 1)-dimensional integrable system. In fact, in this case $\det P_j \neq 0$, one can express all derivatives of $\hat{\Psi}$ with respect to x_j, $j > 1$ through the derivatives of $\hat{\Psi}$ with respect to x_1 using Eq. (11). Both

Eqs. (11) and (12) are $M \times M$ matrix Eqs. for an $M \times M$ matrix function $\hat{\Psi}$. Thus, Eq. (11) can be taken for the spectral problem, while Eq. (12) represents the evolution part of the overdetermined linear system. For instance, if $M = R = n = 2$, $\alpha_1 = 1$, $\alpha_2 = 0$, and P_i have the form (14), then the compatibility condition of the linear system (11), (12) is given by Eqs. (15).

The situation is quite different if $R < M$. $\hat{\Psi}$ is an $R \times M$ matrix function, while (11) is an $R \times R$ matrix equation. Thus, it cannot be taken for the spectral problem. Moreover, Eq. (12) involves all derivatives appearing in the operator M. So, we have $(n + 1)$-dimensional equations. An important fact is that the solution of these equations depends on arbitrary functions of n variables, which has been shown in the end of the previous section. Below, we present an example of a $(2 + 1)$-dimensional system of this type.

2.2. Examples

Let $n = 2$, $\alpha_1 = 1$, $a_2 = 0$. Then Eq. (9) reduces to

$$P_1(U_{2_t} + 2U_{1_{x_1x_2}} - U_{2_{x_1x_1}} + 2(U_2U_1)_{x_1} - 2U_{1_{x_1}}U_2) - P_2(U_{1_t} + U_{1_{x_1x_1}} + 2U_1U_{1_{x_1}}) = 0, \quad (13)$$

while Eq. (10) does not exist. First, we show two trivial reductions of Eq. (13).

1. Let matrix A exist such that $AP_1 = 0$ and $AP_2 = I_R$ (I_R is the $R \times R$ identity matrix). Multiplying Eq. (13) by A from the left, one gets the matrix Burgers equation for U_1.

2. If $R = M = 2$ and

$$P_1 = I_2, \quad P_2 = \begin{bmatrix} 0 & 1 \\ 1 & 0 \end{bmatrix}, \quad V = \begin{bmatrix} v_{11} & v_{12} \\ v_{21} & v_{22} \end{bmatrix}, \quad (14)$$

then Eq. (13) is equivalent to the following system:

$$r_t - r_{x_1x_2} - 2rw_{x_1x_2} = 0,$$
$$q_t + q_{x_1x_2} + 2qw_{x_1x_2} = 0, \quad (15)$$
$$w_{x_1x_1} - w_{x_2x_2} = qr,$$

where functions r and q are related with elements of the matrix V by the formulas $v_{11} = \frac{1}{4}(r - q + 2w_{x_1})$, $v_{21} = \frac{1}{4}(r + q + 2w_{x_2})$, $v_{12} = \frac{1}{4}(-r - q + 2w_{x_2})$, $v_{22} = \frac{1}{4}(-r + q + 2w_{x_1})$. Equation (15) becomes the Devi–Stewartson equation after the reduction $r = \psi$, $q = \bar{\psi}$, $t_1 = it$, where $i^2 = -1$ and the bar means complex conjugated value.

A substantially different situation is described in the next example.

3. Let $M = 3$, $R = 2$, $P_1 = \begin{bmatrix} 1 & 0 \\ 0 & 1 \\ 0 & 0 \end{bmatrix}$, $P_2 = \begin{bmatrix} 0 & 0 \\ 1 & 0 \\ 0 & 1 \end{bmatrix}$. It is possible to construct solutions to the system (13) depending on N arbitrary functions of two variables. In fact, let $N = 3m + 2$, $m = 1, 2, \ldots$, matrices B_i be defined, for instance, by the following system:

$$B_j = \begin{bmatrix} 0_{2,2} & b_{j1} & 0_{2,N-5} \\ 0_{3(m-1),2} & 0_{3(m-1),3} & b_{j2} \\ 0_{3,2} & 0_{3,3} & 0_{3,N-5} \end{bmatrix},$$

$$b_{11} = \begin{bmatrix} 1 & 1 & 1 \\ 0 & 0 & 0 \end{bmatrix}, \quad b_{21} = \begin{bmatrix} 0 & 0 & 0 \\ 1 & 1 & 1 \end{bmatrix},$$

$$b_{j2} = \operatorname{diag} \underbrace{(A_j, A_j, \ldots)}_{m-1}, \quad j = 1, 2,$$

$$A_1 = \begin{bmatrix} 1 & 0 & -1 \\ -1 & 1 & 0 \\ 0 & -1 & 1 \end{bmatrix}, \quad A_2 = \begin{bmatrix} 1 & -1 & 0 \\ 0 & 1 & -1 \\ -1 & 0 & 1 \end{bmatrix}.$$

$\Phi = [\phi_1 \ \phi_2 \ \phi_3]$, where ϕ_k are N-dimensional columns. Then Eq. (6) can be written in the form $\phi_{1_{x_2}} = \phi_{2_{x_1}}$, $\phi_{2_{x_2}} = \phi_{3_{x_1}}$, i.e., $\phi_1 = S_{x_1x_1}$, $\phi_2 = S_{x_1x_2}$, $\phi_3 = S_{x_2x_2}$, where S is an arbitrary function of variables x_1 and x_2. In view of Eqs. (3), we can write for Φ: $\Phi = \int_{-\infty}^{\infty} c(k_1, k_2)\begin{bmatrix} k_1^2 & k_2k_1 & k_2^2 \end{bmatrix}\exp[k_1x_1 + k_2x_2 - k_1^2t]dk_1dk_2$, where $c(k_1, k_2)$ is an arbitrary column of N elements. Function Ψ (solution of systems (2) and (3)) can be represented in the form $\Psi = (\Psi_0 + \tilde{\Psi})e^{\eta}$, $\eta = B_1x_1 + B_2x_2 - B_1^2t$, where Ψ_0 is an arbitrary constant $N \times N$ matrix and $\tilde{\Psi}$ is taken in the form $\tilde{\Psi} = \partial_{x_1}^{-1}\Phi C_1 e^{-\eta}$. Then $U = \Psi^{-1}\Phi$ depends on an arbitrary $N \times 1$ matrix function $c(k_1, k_2)$ of two variables.

The appropriate nonlinear system (13) has a rather complicated form. To simplify it for application, we suggest two methods.

1. Multiscale expansion. We introduce parameter $\epsilon \ll 1$ and new scales for coordinates: $\partial_{x_j} \longrightarrow \epsilon\partial_{x_j}$ and $\partial_t \longrightarrow \epsilon^2\partial_t$. Let us consider matrix V in the form

$$V = \begin{bmatrix} 2 + \epsilon^2u_1 & \epsilon^2v_1 & \epsilon + \epsilon^2w_1 \\ \epsilon u & 1 + \epsilon v & \epsilon^2w_2 \end{bmatrix}.$$

Then we can write Eq. (13) in the form of the two-component Burgers equation with perturbation up to the order $O(\epsilon^2)$:

$$2u_{x_1} = -\epsilon(u_t + 2vu_{x_1} + u_{x_1x_1}) + \epsilon^2(4uvv_{x_1} - 2uu_{x_1x_2} + 2uv_{x_1x_1}),$$

$$2v_{x_1} = -\epsilon(v_t + 2vv_{x_1} + v_{x_1x_1}) + 2\epsilon^2 uu_{x_1}.$$

One can eliminate derivatives with respect to x_1 from the right-hand sides (terms with ϵ^3 appear): $2u_{x_1} = -\epsilon u_t + \epsilon^2 vu_t - \epsilon^3(v^2u_t + 2uvv_t + 1/4u_{tt} - uu_{x_2t})$, $2v_{x_1} = -\epsilon v_t + \epsilon^2 vv_t - \epsilon^3(uu_t + v^2v_t + 1/4v_{tt})$.

2. Reductions. There is a wide class of reductions in the form of additional differential equations for the functions ϕ_i, $i = 1, 2, 3$, compatible with the two equations written above. They reduce the number of independent functions in Eq. (13), although freedom in construction of solutions is reduced as well. For instance, let $\phi_2 = \phi_{1_{x_1}}$ and $S_{x_2x_1} = S_{x_1x_1x_1}$. One has an additional equation for the column of the matrix $V = [V_1\ V_2\ V_3]$: $V_2 = (B_1 + U_1)V_1 + V_{1_{x_1}}$. Using the first column of Eq. (8) (with $n = 2$, $\alpha_1 = 1$, $\alpha_2 = 0$), one can eliminate B_1 from the above equation to yield $V_{1_t} + V_{1_{x_1x_1x_1}} + 2U_1V_{1_{x_1}} = -2V_{2_{x_1}} + 2(U_1V_1)_{x_1} + 2V_{1_{x_1x_1}}$. With this equation, nonlinear system (13) is reduced to

$$q_t + q_{x_1x_1} + 2q\varphi_{x_1x_1} = 0, \quad \varphi_t + \varphi_{x_2} = 0,$$

$$\varphi_{x_2x_2} + 2\varphi_{x_1x_1}^2 + [\varphi_{x_1x_1x_1} - 2\varphi_{x_1x_2} - 2\varphi_{x_2}\varphi_{x_1} + 2\varphi_{x_1}\varphi_{x_1x_1} + \frac{2}{3}\varphi_{x_1}^3]_{x_1} = 0,$$

where φ and q are expressed through the first-column elements of V: $\varphi_{x_1} = v_{11}/(1 - v_{21})$, $q = v_{21}/(1 - v_{21})$. Note that the last equation has no Lagrangian. It may be given the form of the nonlinear Burgers equation with nonlocal correction after applying the operator $\partial_{x_1}^{-2}$.

The presented version of the dressing method works for a wide class of $(n + 1)$-dimensional PDEs. It supplies solutions depending on arbitrary functions of n variables provided $R < M$. In the case $R = M$, the solution depends on arbitrary functions of a single variable. By construction, equations have an infinite number of commuting flows introduced by Eqs. (3). They are also compatibility conditions for some specific linear overdetermined systems, which are equivalent to the classical isospectral problems only if $R = M$.

This work was supported by the Russian Foundation for Basic Research, project nos. 02-01-06059 and 00-15-96007. The author thanks Prof. S.V. Manakov and Dr. Marikhin for discussions and Dr. Bogdanov for useful comments.

REFERENCES

1. V. E. Zakharov and A. B. Shabat, Funct. Anal. Appl. **8**, 43 (1974).
2. V. E. Zakharov and A. B. Shabat, Funct. Anal. Appl. **13**, 13 (1979).
3. V. E. Zakharov and S. V. Manakov, Funct. Anal. Appl. **19**, 11 (1985).
4. L. V. Bogdanov and S. V. Manakov, J. Phys. A: Math. Gen. **21**, L537 (1988).
5. B. Konopelchenko, *Solitons in Multidimensions* (World Sci., Singapore, 1993).
6. A. I. Zenchuk, J. Math. Phys. **41**, 6248 (2000).
7. Y. Ohta, J. Satsuma, D. Takahashi, and T. Tokihiro, Prog. Theor. Phys. Suppl. **94**, 210 (1988).
8. A. I. Zenchuk, arXiv:nlin.SI/0202053 v1 (2002).
9. A. I. Zenchuk, arXiv:nlin.SI/0210031 v1 (2002).
10. F. Guil, M. Mañas, and G. Álvarez, Phys. Lett. A **190**, 49 (1994).

JETP Letters, Vol. 77, No. 6, 2003, pp. 328–330. From Pis'ma v Zhurnal Éksperimental'noĭ i Teoreticheskoĭ Fiziki, Vol. 77, No. 6, 2003, pp. 380–382.

A Quantum Computer with Fixed Interaction is Universal¶

Y. Ozhigov and L. Fedichkin

Institute of Physics and Technology, Russian Academy of Sciences, Moscow, 117218 Russia

e-mail: ozhigov@ftian.oivta.ru

e-mail: leonid@ftian.oivta.ru

Received February 10, 2003

It is proved that a quantum computer with fixed and permanent interaction of diagonal type between qubits proposed in the work quant-ph/0201132 is universal. Such a computer is controlled only by one-qubit quick transformations, and this makes it feasible. © *2003 MAIK "Nauka/Interperiodica".*

PACS numbers: 03.67.Lx

1. Introduction and background. A model of a quantum computer with fixed and permanent interaction between qubits was proposed in paper [1], where it was shown how to implement QFT and simulation of wave function dynamics by such a computer. In this paper, we prove that such a model is universal: that is, every quantum algorithm can be implemented in the framework of this model with only a linear slowdown for long-distance interaction and with a slowdown proportional to size of memory for short-distance interaction. Here, we have to suppress undesirable interactions, as in [2]. But now we shall use the method of random strings consisting of NOT operations proposed in [1], which uses a diagonal form of interactions. Surprisingly, our method of suppressing undesirable interactions does not depend on individual features of qubits.

A traditional way for implementation of quantum algorithms requires control on the two-qubit level, that is, the ability to "switch on" and to "switch off" interaction between qubits. It is widely known that two-qubit transformations are a stumbling block in quantum computing in view of technological difficulties. The most natural way is to use a fixed and permanent interaction between qubits and control the process of computation by only one-qubit transformations. This way gives a universal quantum computer if our fixed interaction has a diagonal type. Note that it is not important that a fixed interaction decreases depending on the distance between qubits; for example, it may be nonzero only for the neighboring qubits, etc.

A permanent interaction between the qubits in our computer depends only on their spatial disposition, which is fixed. The only condition we impose on the interaction is that it must be diagonal. Thus, if j and k denote the identification numbers of two qubits, then the Hamiltonian of their interaction will have the form

$$H_{j,k} = \begin{pmatrix} E_1^{j,k} & 0 & 0 & 0 \\ 0 & E_2^{j,k} & 0 & 0 \\ 0 & 0 & E_3^{j,k} & 0 \\ 0 & 0 & 0 & E_4^{j,k} \end{pmatrix}, \qquad (1A)$$

$$H_{j,k} = \begin{pmatrix} 0 & 0 & 0 & 0 \\ 0 & 0 & 0 & 0 \\ 0 & 0 & 0 & 0 \\ 0 & 0 & 0 & E_{j,k} \end{pmatrix}, \quad E_{j,k} > 0. \qquad (1B)$$

At first, note that any interaction of the general form (1A) may be reduced to the form (1B) by adding appropriate one-qubit Hamiltonians $H'_{j,k}$, whose matrices have the forms

$$\begin{pmatrix} a & 0 & 0 & 0 \\ 0 & a & 0 & 0 \\ 0 & 0 & b & 0 \\ 0 & 0 & 0 & b \end{pmatrix}, \quad \begin{pmatrix} \alpha & 0 & 0 & 0 \\ 0 & b & 0 & 0 \\ 0 & 0 & a & 0 \\ 0 & 0 & 0 & \beta \end{pmatrix}.$$

This addition reduces the Hamiltonian of the form (1A) to (1B) and can be alternatively fulfilled by one-qubit quick transformations, because all these diagonal matrices commute.

Note that different pairs of qubits may interact variously: they may be disposed with different intervals and not be placed along one line, etc.

2. Suppression of undesirable interactions by one-qubit operations. To prove the universality of the computational model, we must show how one can fulfil an arbitrary two-qubit operation. Given a unitary trans-

¶ This article was submitted by the authors in English.

form induced by Hamiltonian (1B) in time frame 1, $U_{j,k} = \exp(-iH_{j,k})$ (Plank's constant equals 1). In fact, it would suffice to fulfill this transform on two qubits, the jth and kth, leaving all the others untouched. Just this last condition is difficult to guarantee for permanent interaction. If we can do it when at first we can fulfill an arbitrary two-qubit operation with every separated pair of qubits, then, for a long-distance interaction, we have at most a linear slowdown; for a short-distance interaction we need to perform SWAP operations to bring the required pair of qubits together and thus we obtain a time factor equal to the size of the memory.

Now we show how to implement $U_{j,k}$. If we simply wait for a time 1, when we obtain a transformation $U_{j,k} \otimes U' \otimes \ldots \otimes U''$, where all U' have the form $U_{j',k'}$, where $\{j', k'\} \neq \{j, k\}$. We should get rid of these interactions. We declare jth and kth qubits separated.

We apply one qubit NOT gate several times to all qubits except separated ones to suppress all two-qubit interactions excluding interaction between separated qubits. For each not-separated qubit number p, consider the Poisson random process $\mathcal{A}_p$ generating times $0 < t_1^p < t_2^p < \ldots < t_{m_p}^p < 1$ with some fixed density $\lambda \gg 1$. Let all $\mathcal{A}_p$ be independent. Now perform NOT transformations on each pth qubit at instants t_m^p sequentially. At instant 1, perform NOT on the pth qubit if and only if m_p is odd. Then after this procedure each qth qubit restores its initial value a_q. Count the phase shift generated by this procedure. The interaction between separated qubits remains unchanged. We fix some not-separated qubit number p and count its deposit to phase. It consists of two summands: the first comes from interaction with separated qubits, and the second, from interaction with not-separated qubits. We count them sequentially.

1. In view of the high density λ of Poisson process $\mathcal{A}_p$ about half the time our pth qubit will be in state a_p, and the other half, in $1 - a_p$. Its interaction with a separated qubit, say the jth, brings the deposit $\frac{1}{2}E_{p,j}a'_p a'_j + \frac{1}{2}E_{p,j}(1 - a'_p)a'_j$, that is, $\frac{1}{2}E_{p,j}a'_j$.

2. Consider a different not-separated qubit number $q \neq p$. In view of the independence of times when NOTs are performed on pth and qth qubits and the high density λ, these qubits will be in each of states (a_p, a_q), $(a_p, 1 - a_q)$, $(1 - a_p, a_q)$, $(1 - a_p, 1 - a_q)$ approximately a quarter of the time. The resulting deposit will be $\frac{1}{4}E_{p,q}[a_p a_q + a_p(1 - a_q) + (1 - a_p)a_q + (1 - a_p)(1 - a_q)] = \frac{1}{4}E_{p,q}$.

The total phase shift issued from the presence of not-separated qubits in our procedure is now obtained by summing values from items 1 and 2 for all $p \notin \{j, k\}$. It is

$$\frac{1}{2}\left[\sum_{p \notin \{j,k\}} E_{p,j}a_j + \sum_{p \notin \{j,k\}} E_{p,k}a_k\right] + \frac{1}{4}\sum_{p \notin \{j,k\}} E_{p,q}.$$

This shift can be compensated by one-qubit operations, because the first two summands depend linearly on the qubit values, and the second does not depend on qubit values at all. Thus, we obtain a gate with a permanent two-qubit interaction and one-qubit operations performing phase shift to $d_{j,k}a_j a_k$ that is required. If we take the time frame Δt instead of unit time in this procedure, we obtain the phase shift to $\Delta t\, E_{j,k}a_j a_k$.

Thus, we can implement $U_{j,k}$ for every separated pair of qubits.

3. Implementation of controlled-NOT by fixed interaction. Now we show in detail how to implement a controlled-NOT (CNOT) gate with a given pair of qubits. Let j, k be fixed and omit these indexes. Denote $\Delta E = E_1 - E_2 - E_3 + E_4$. If $\frac{\Delta E}{\pi} \notin Q$ ($\frac{\Delta E}{\pi}$ is not a rational number), then (since some physical parameters of our system influencing phases, for example, cycle period, can be slightly varied to avoid rationality of this parameter, the opposite case (rationality) can be ignored without lack of generality) we can effectively implement a common two-qubit CNOT gate

$$\mathrm{CNOT} = \begin{pmatrix} 1 & 0 & 0 & 0 \\ 0 & 1 & 0 & 0 \\ 0 & 0 & 0 & 1 \\ 0 & 0 & 1 & 0 \end{pmatrix}$$

over our pair of neighboring qubits by using a sequence of gates only from a given set of arbitrary one-qubit rotations and fixed diagonal two-qubit gate E,

$$E = \begin{pmatrix} \exp(iE_1) & 0 & 0 & 0 \\ 0 & \exp(iE_2) & 0 & 0 \\ 0 & 0 & \exp(iE_3) & 0 \\ 0 & 0 & 0 & \exp(iE_4) \end{pmatrix},$$

in the following way.

I. Denote the gate implementing by sequential implementation of the first qubit phase rotation A,

$$A = \begin{pmatrix} 1 & 0 \\ 0 & \exp(i(E_1 - E_3)) \end{pmatrix},$$

second qubit phase rotation B,

$$B = \begin{pmatrix} \exp(-iE_1) & 0 \\ 0 & \exp(-iE_2) \end{pmatrix},$$

and gate E as U:

$$U = E(A \otimes B) = \begin{pmatrix} 1 & 0 & 0 & 0 \\ 0 & 1 & 0 & 0 \\ 0 & 0 & 1 & 0 \\ 0 & 0 & 0 & \exp(i\Delta E) \end{pmatrix}.$$

II. By using the irrationality of $\Delta E/\pi$, it can be shown that

$$\forall \varepsilon > 0 \exists m \in N \exists n \in N: |\Delta E n - \pi(2m+1)| < \varepsilon;$$

i.e., for any desired accuracy ε, there exists $n = n(\varepsilon)$ such that U^n will approach Π gate,

$$\Pi = \begin{pmatrix} 1 & 0 & 0 & 0 \\ 0 & 1 & 0 & 0 \\ 0 & 0 & 1 & 0 \\ 0 & 0 & 0 & -1 \end{pmatrix},$$

with a given accuracy.

III. By using the relation

$$(I \otimes H)\Pi(I \otimes H) = \text{CNOT},$$

where I is the identity matrix

$$I = \begin{pmatrix} 1 & 0 \\ 0 & 1 \end{pmatrix}$$

and H is the Hadamard gate

$$H = \frac{1}{\sqrt{2}} \begin{pmatrix} 1 & 1 \\ 1 & -1 \end{pmatrix},$$

or, in matrix form,

$$\frac{1}{\sqrt{2}} \begin{pmatrix} 1 & 1 & 0 & 0 \\ 1 & -1 & 0 & 0 \\ 0 & 0 & 1 & 1 \\ 0 & 0 & 1 & -1 \end{pmatrix} \begin{pmatrix} 1 & 0 & 0 & 0 \\ 0 & 1 & 0 & 0 \\ 0 & 0 & 1 & 0 \\ 0 & 0 & 0 & -1 \end{pmatrix}$$

$$\times \frac{1}{\sqrt{2}} \begin{pmatrix} 1 & 1 & 0 & 0 \\ 1 & -1 & 0 & 0 \\ 0 & 0 & 1 & 1 \\ 0 & 0 & 1 & -1 \end{pmatrix} = \begin{pmatrix} 1 & 0 & 0 & 0 \\ 0 & 1 & 0 & 0 \\ 0 & 0 & 0 & 1 \\ 0 & 0 & 1 & 0 \end{pmatrix},$$

we see that controlled-NOT is finally obtained by the sequence

$$(I \otimes H)(E(A \otimes B))^n (I \otimes H)$$

of one-qubit rotations and gate E.

It is established that a quantum computer controlled by quick one-qubit transformations and with fixed permanent interaction of diagonal form between qubits is universal. This means that this type of quantum computer can implement all possible quantum algorithms by switching on and off only one-qubit gates.

We are grateful to Kamil Valiev for a stimulating discussion.

REFERENCES

1. Y. Ozhigov, Pis'ma Zh. Éksp. Teor. Fiz. **76**, 746 (2002) [JETP Lett. **76**, 675 (2002)].
2. L. Fedichkin, Quantum Comput. Comput. **1**, 84 (2000); LANL e-print quant-ph/0011005.